

118022
NASA Technical Memorandum 4382

Experimental Study of a Generic
High-Speed Civil Transport

Pamela S. Bolton and Richard L. Campbell

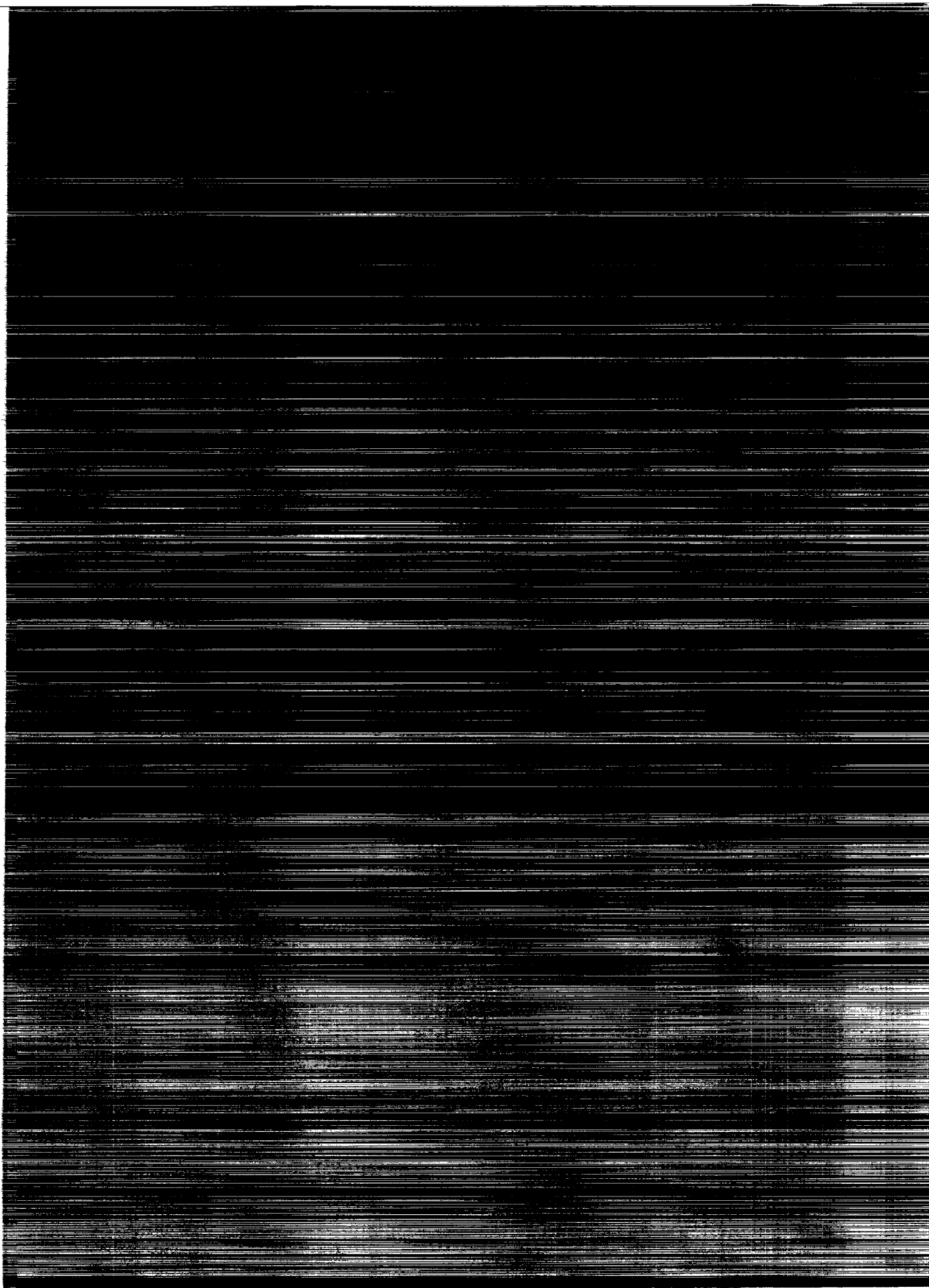
SEPTEMBER 1992

(NASA-TM-4382) EXPERIMENTAL STUDY
OF A GENERIC HIGH-SPEED CIVIL
TRANSPORT (NASA) 115 p

N92-33631

Unclass

H1/02 0118022



NASA Technical Memorandum 4382

Experimental Study of a Generic High-Speed Civil Transport

Pamela S. Belton and Richard L. Campbell
Langley Research Center
Hampton, Virginia



National Aeronautics and
Space Administration

Office of Management

Scientific and Technical
Information Program

1992

Summary

An experimental study of a generic high-speed civil transport has been conducted in the NASA Langley 8-Foot Transonic Pressure Tunnel. The data base was obtained for the purpose of assessing the accuracy of various levels of computational analysis. Two models differing only in wingtip geometry were tested with and without flow-through nacelles. The baseline model has a curved or crescent wingtip shape, while the second model has a more conventional straight wingtip shape. The study was conducted at Mach numbers from 0.30 to 1.19. Force data were obtained on both the straight wingtip model and the curved wingtip model. Only the curved wingtip model was instrumented for measuring pressures. Selected longitudinal and lateral-directional aerodynamic characteristics of both models are presented in graphical form. Selected pressure distributions for the curved wingtip model are also presented. Results indicate that the straight wingtip model produced slightly better longitudinal characteristics than the curved wingtip model. Adding the nacelles to both models also increased lift and improved pitching-moment characteristics. Lateral-directional data were essentially the same for both wingtip configurations. The nacelles also improved the lateral-directional characteristics of both models. Pressure data show vortical flow development and effects of adding nacelles to the curved wingtip model.

Introduction

Recent studies (refs. 1 and 2) have indicated that there is a large and growing potential market for a high-speed civil transport (HSCT). This fact, along with a number of promising technological advances, has prompted a number of the aircraft companies to renew their research efforts for this class of aircraft. Their interest is reflected in the report of the Aeronautical Policy Review Committee (ref. 3), in which the second of three proposed national goals is the development of the technologies required for an economically viable and environmentally acceptable HSCT. In response to this report, NASA has implemented the High-Speed Research Program. As part of this program, NASA Langley initiated several contractor (refs. 1 and 2) and in-house (refs. 4 and 5) studies to evaluate a variety of configurations relative to these issues and technologies.

One of these configurations, the NASA Langley baseline Mach 3.0 aircraft (ref. 5), has been selected as the focus of the initial phase of the High-Speed Airframe Integration Research (HiSAIR) program. This program was established at Langley to promote

the development of methodology for improving multidisciplinary analysis, design, and optimization of aircraft systems. Although an HSCT configuration was selected for developing this methodology, the resulting methods and processes would, in general, apply to all aircraft.

The first phase of the HiSAIR program involves performing a multidisciplinary analysis of the baseline configuration. As part of this effort, a hierarchy of aerodynamic codes ranging from linear to Navier-Stokes methods (refs. 6-8) has been used to analyze this configuration with the goal of comparing the relative accuracy and efficiency of the different methods. In order to provide a data base for assessing the accuracy of the codes, force, moment, and pressure data have been obtained in two NASA Langley wind tunnels on a 0.01-scale model of the baseline Mach 3.0 configuration. Data at supersonic speeds were taken in both the high-speed section and the low-speed test section of the Langley Unitary Plan Wind Tunnel and have been reported in reference 6. These data include the primary design point at the cruise Mach number of 3.0. It is recognized, however, that an HSCT would probably be restricted to subsonic flight over land (refs. 1 and 4) and that this could represent a significant fraction of the total flight time. Therefore, the baseline Mach 3.0 model was also tested at subsonic and transonic speeds in the Langley 8-Foot Transonic Pressure Tunnel (TPT).

The force, moment, and pressure data obtained during the 8-Foot TPT tests are presented in this report. The test Mach numbers range from 0.30 to 1.19 at a constant Reynolds number of 2.0 million per foot. The angle-of-attack range varied with Mach number because of balance load limits, with the maximum range of -4° to 18° occurring at $M = 0.30$. In addition, lateral-directional data were taken at selected Mach numbers for sideslip angles ranging from -7.5° to 5° . Force and moment data were also obtained for an alternate version of the baseline configuration having straight wingtips.

Symbols

The results presented in this report are referred to the stability-axis system for the longitudinal aerodynamic characteristics and to the body-axis system for the lateral-directional characteristics. Force and moment data have been reduced to conventional coefficient form based on the geometry of the wing planform. Moments are referenced to the quarter-chord point of the mean aerodynamic chord of the wing. All measurements and calculations were made in U.S. Customary Units.

Coefficients and symbols used herein are defined as follows:

b	wingspan, 18.19 in.
C_A	axial-force coefficient, $\frac{\text{Axial force}}{q_\infty S}$
C_D	drag coefficient, $\frac{\text{Drag}}{q_\infty S}$
C_L	lift coefficient, $\frac{\text{Lift}}{q_\infty S}$
C_l	rolling-moment coefficient, $\frac{\text{Rolling moment}}{q_\infty S b}$
C_{l_β}	derivative of C_l with respect to β
C_m	pitching-moment coefficient, $\frac{\text{Pitching moment}}{q_\infty S \bar{c}}$
C_{m_α}	derivative of C_m with respect to α
C_N	normal-force coefficient, $\frac{\text{Normal force}}{q_\infty S}$
C_{N_α}	derivative of C_N with respect to α
C_n	yawing-moment coefficient, $\frac{\text{Yawing moment}}{q_\infty S b}$
C_{n_β}	derivative of C_n with respect to β
C_p	pressure coefficient, $\frac{p - p_\infty}{q_\infty}$
C_Y	side-force coefficient, $\frac{\text{Side force}}{q_\infty S}$
C_{Y_β}	derivative of C_Y with respect to β
c	local wing chord, in.
\bar{c}	mean aerodynamic chord, 15.66 in.
M_∞	free-stream Mach number
p	local pressure, psi
p_∞	free-stream static pressure, psi
q_∞	free-stream dynamic pressure, psi
r	local leading-edge radius, in.
S	reference wing area, 175.84 in ²
x	longitudinal distance, positive aft, in.
y	distance left/right of model centerline, positive to left, in.
z	vertical distance, positive up, in.
α	model angle of attack, deg
α_n	angle of attack normal to the leading edge

β	model angle of sideslip, deg
η	fractional semispan location of orifice rows, $\frac{2y}{b}$
Λ	leading-edge sweep
ψ	model angle of yaw, deg

Abbreviations:

B.L.	butt line, in.
L.E.	leading edge
M.S.	model station, in.

Model Description

The baseline, or curved wingtip, model (fig. 1) is a 0.01-scale version of the NASA Langley Mach 3.0 HSCT configuration described in reference 5 and is shown installed in the Langley 8-Foot Transonic Pressure Tunnel in figures 2 and 3. It consists of a highly blended wing-fuselage with flow-through engine nacelles mounted on the lower surface near and extending beyond the trailing edge of each wing. The constant duct area nacelles are removable to allow wing-body testing and thus simplify grid generation requirements for computational comparisons. The inboard and outboard wing panels have leading-edge sweeps of 79° and 53°, respectively. The inboard panels are highly cambered and have rounded leading edges for increased leading-edge suction at cruise conditions. The outer panels have sharp leading edges, since their reduced sweep places them ahead of the Mach cone at cruise conditions. Airfoil sections for this configuration were derived by using an NACA 65-series thickness form with the camber determined from supersonic linear theory design. The configuration has a "platypus" nose shape for additional lift, and the wingtip has a curved planform based on the concept for reducing pitch-up described in reference 5. The aft section of the fuselage and the vertical tail are not included in the model to allow for the sting mounting system. The model wing reference area is 175.84 in², the wingspan is 18.19 in., and the mean aerodynamic chord measures 15.66 in. Coordinates for the wing airfoil sections are given in table I.

A second model with a more conventional straight wingtip was built to study the effect of tip shape on the pitch-up and induced drag characteristics for this type of aircraft. According to reference 5, having a straight wingtip geometry in conjunction with a highly swept wing should produce more pitch-up and less induced drag than a similar wing with a curved wingtip geometry. Figure 4 shows this straight wingtip model installed in the 8-Foot TPT. Figure 5 is a close-up comparison of the two wingtips.

The wingspan and area are the same for the two configurations.

The curved wingtip model was instrumented with 60 flush pressure orifices of 0.020-in. inside diameter, arranged in 2 chordwise and 4 spanwise rows, as shown in figure 6 and listed in table II. The pressure tubes exited at the model base and then were routed aft along the sting. The straight wingtip model was not pressure instrumented. Both models were fabricated from 7075 aluminum.

Apparatus and Procedures

Facility

These investigations were performed in the 8-Foot Transonic Pressure Tunnel at the NASA Langley Research Center. This facility is a variable-pressure slotted-throat wind tunnel that permits independent variations of Mach number, stagnation pressure, and temperature. The test section is a 7.125-ft square with filleted corners, giving a cross-sectional area approximately equivalent to an 8-ft-diameter circle. The floor and the ceiling are axially slotted, which results in approximately 6.9-percent open area in the calibrated test region. The sidewalls are solid and fitted with windows for schlieren flow visualization. Off-body flow visualization is obtained with a laser vapor screen system designed for vortex-dominated flow fields. A description of the tunnel and data system is given in reference 9.

Tests

The present investigation was performed at Mach numbers from 0.30 to 1.19. All data were taken at a Reynolds number of 2.0 million per foot. The angle-of-attack range was dependent on Mach number, with a maximum variation of -4° to 18° occurring at a Mach number of 0.30. Lateral-directional data were obtained for sideslip angles from -7.5° to 5° .

Pressure data were obtained for the curved-tip model only. A dummy balance was used for these tests, since the model was too small for both a balance and the number of pressure tubes installed. This would have resulted in extensive fouling and possible damage to a live balance. The pressure tubes were later removed to allow force and moment testing. Force and moment data were obtained for both models over the entire test envelope. Both models were tested with and without flow-through nacelles mounted on the wing lower surface.

Although not presented in this report, off-body flow visualization data were obtained at selected conditions for the curved-tip model by using a laser light

sheet system. This was used primarily to study the vortex patterns generated by the wing. Schlieren photography was used at the supersonic Mach numbers to verify that the shock waves reflecting from the tunnel walls were not impinging on the model.

Boundary-Layer Transition

Boundary-layer transition was fixed on the models by using transition strips composed of Carborundum grains set in a plastic adhesive. The roughness particle sizes and locations were selected according to the method of reference 10. The strips were approximately 0.06-in-wide bands of No. 120 Carborundum grains located 0.75 in. from the nose. No. 90 Carborundum grains were located 0.75 in. aft and perpendicular to the leading edge of the wing and 0.75 in. aft and perpendicular to the leading edge of the nacelles. The grit was applied to both upper and lower wing surfaces and both inner and outer nacelle surfaces.

Measurements and Corrections

Aerodynamic forces and moments for the models were measured with an internally mounted six-component strain-gauge balance. Model attitude was set with an accelerometer mounted on the sting support system. Output from the accelerometer was used in conjunction with the balance output to determine model attitude. For the case where a dummy balance was used, the following equation was solved iteratively to determine model attitude:

$$\alpha = \theta_s + \bar{k}_n f_1(\alpha) + \bar{k}_\theta f_2(\alpha)$$

where $f_1(\alpha)$ and $f_2(\alpha)$ are regression polynomials for C_{N_α} and C_{m_α} , respectively, which were determined when a balance was present, θ_s is the known accelerometer angle, and \bar{k}_n and \bar{k}_θ are nondimensional bending coefficients from the dummy balance.

Flow angularity was determined by testing the model in both upright and inverted positions. A correction of 0.28° upwash was applied to the data at $M_\infty = 1.19$. Corrections at other Mach numbers were negligible. Balance forces were adjusted to a condition of free-stream static pressure acting over the sting cavity area. No corrections were applied for internal drag of the flow-through nacelles. The accuracy of the data, based on instrument accuracy (0.5 percent of full-scale load on the balance), is

estimated to be as follows:

$$\begin{aligned}C_N &= \pm 0.006 \\C_A &= \pm 0.0009 \\C_m &= \pm 0.0008 \\C_l &= \pm 0.0002 \\C_n &= \pm 0.0004 \\C_Y &= \pm 0.003 \\\alpha &= \pm 0.01^\circ \\\psi &= \pm 0.20^\circ \\M_\infty &= \pm 0.001\end{aligned}$$

Coefficient values are based on a conservative, nominal dynamic pressure of 0.97 psi corresponding to data for $M_\infty = 0.30$.

Presentation of Results

The remainder of this paper will present results and analysis from the wind tunnel test. In order to reduce the volume of this paper, only representative results from the wind tunnel test are presented. Complete data are presented in reference 11.

Figures 7-10 show the longitudinal characteristics of the straight and curved wingtip models with nacelles on and off for all Mach numbers tested. Figures 11 and 12 show induced drag characteristics of the models tested, again with and without nacelles. Lateral-directional data are presented in figures 13-16. Finally, figures 17-19 show chordwise and spanwise pressure distribution results for the curved wingtip model with nacelles on and off.

Discussion of Results

Longitudinal Results

The effects of the wingtip geometry on lift can easily be seen at all Mach numbers in figures 7 and 8. The straight wingtip model consistently generated slightly more lift than the curved wingtip model at the higher angles of attack tested. Lift-versus-drag curves for the two configurations were similar at the lower Mach numbers, but indicated a slight drag benefit for the straight wingtip model with nacelles on at some of the higher Mach numbers (see figs. 8(e)-(g)). Pitching-moment characteristics were similar only at the extreme lower angles of attack tested. At all other angles of attack, pitch-up occurred at higher lift coefficients and pitching moment was reduced for the straight wingtip model in comparison with the curved wingtip model.

The data indicate that the tip area of the curved wingtip model has unloaded, resulting in lower lift coefficients and more pitch-up than seen for the straight wingtip model. This may be due to differences in the static aeroelastic deflections of the two wing shapes. The curved-tip shape places more area aft of the wing structural axis, increasing the nose-down torsional load for this wing. This increased torsional moment causes this wing to have more twist (washout) than the straight tip wing, thus reducing the lift in this region. To recover the lost lift, the configuration angle of attack must be increased. As a result, the lift distribution is shifted inboard and, because of the sweep angle, forward on the curved-tip wing. This forward movement of the resultant lift vector gives the curved-tip model a more positive pitching moment than the model with the straight wingtip. This effect is consistent with results shown in reference 12 for the static aeroelastic bending of swept wings on combat aircraft.

Another possible cause of the wingtip unloading can be gleaned from the aerodynamics of a vortex dominated flow field. The vortex of the curved wingtip is expected to be weaker because of the increase in sweep (ref. 13) than the tip vortex of the straight wingtip. The weaker vortex would result in lower lift and therefore increased pitch-up at lower lift coefficients, as seen in the data.

Figures 9 and 10 demonstrate the effects of the flow-through nacelles on the longitudinal characteristics of both models. When the nacelles were added, lift increased, pitch-up occurred at higher lift coefficients, and pitching moment decreased. Drag also increased at the lower angles of attack for $M_\infty < 0.95$. At $M_\infty \geq 0.95$, drag increased over the entire angle-of-attack range. The increase in lift can be explained by looking at the pressure distributions in figures 17-19. Near the leading edge of the nacelles, the velocity on the lower surface of the wing was reduced, thus generating more positive pressures and, as a result, increased lift. As expected when a component such as a nacelle is added to the configuration, there is an increment in the drag coefficient at zero-lift conditions due to the larger wetted area. However, this increment disappears at higher angles of attack for $M_\infty < 0.95$. This implies that the nacelles increase the span efficiency at the conditions where the drag increment disappears. Pitching-moment characteristics also improve with the addition of nacelles. In figure 3, it is clear that the nacelles extend well beyond the trailing edge of the wing. This aft location of the nacelles effectively extends a portion of the trailing edge of the wing and acts like a lifting surface. Since this surface is aft of the balance moment

center, it would tend to decrease the pitching moment. A decrease in the pitching moment would also result from the drag of the nacelles acting through a point below the moment reference center.

Effects of wingtip geometry on induced drag characteristics can be seen in figures 11 and 12. Since the Oswald efficiency factor e is proportional to the inverse of the slope of the curves in figures 11 and 12, a smaller slope is desirable and indicates less induced drag. For the conditions tested, the straight wingtip model produced a smaller slope and therefore a greater span efficiency factor than the curved wingtip model. The most significant difference in the curves occurs at $M_\infty = 0.95$ with the nacelles off and between $M_\infty = 0.80$ and 0.95 with the nacelles on. From tabulated data published in reference 11 at $M_\infty = 0.95$, the span efficiency factor of the straight wingtip model with nacelles off was 0.026 higher than that of the curved wingtip model between angles of attack of 3.0° and 6.4° . An increase of 0.031 in the span efficiency factor for the straight wingtip model as compared with the curved wingtip model was also computed at $M_\infty = 0.90$ between angles of attack of 3.1° and 8.4° with the nacelles on. This was not anticipated in reference 5, where the curved wingtip geometry was expected to exhibit better induced drag and pitch-up characteristics.

Lateral-Directional Results

Lateral-directional data are presented in figures 13 and 14 for four of the Mach numbers tested. All configurations were stable in yaw and roll at the conditions tested. Wingtip geometry effects are very small, as seen in figure 13. The most significant difference occurs in the side-force coefficient between angles of attack of 4° and 8° at the lower Mach numbers tested. This angle-of-attack region is where leading-edge separation and the resultant vortex formation on the highly swept portion of the wings is expected to develop. At all Mach numbers in this angle-of-attack region, the straight wingtip model has a slightly greater side-force coefficient. Asymmetry in the data, especially seen at $M_\infty = 0.30$, is probably due to errors in setting the model correctly at zero sideslip and asymmetry in the model itself.

Effects of the nacelles on lateral-directional characteristics of the curved wingtip model can be seen in figure 14. At all Mach numbers the nacelles simply increased the magnitude of the lateral-directional coefficients by a nearly constant amount over the range of angles of attack tested.

Lateral-directional data are presented in derivative form in figures 15 and 16 for four of the

Mach numbers tested. Derivatives were computed at sideslip angles of 0° and 5° . These figures have been drawn on the largest scale possible where differences in the curves could still be seen. As a result, the error in the data is greater than the symbol size; however, the trends seen are consistent and worth noting.

From figure 15 it is clear that notable differences in the results obtained with the two wingtip geometries occur at higher angles of attack. The differences show the curved wingtip model with slightly increased stability at higher angles of attack. The higher sweep of this wingtip at sideslip conditions may weaken the vortical forces and delay vortex burst, thus improving stability.

The changes seen in the slopes of the side-force and yawing-moment derivatives for both wings correspond to two test conditions where the physical characteristics of the flow are changing with angle of attack. The equation for angle of attack normal to the leading edge is given by

$$\alpha_n = \tan^{-1} \frac{\tan \alpha}{\cos \Lambda}$$

Therefore, at a given model angle of attack and sideslip angle, the sweep of the windward wing is reduced and the angle of attack normal to the leading edge is also reduced. Similarly, the sweep of the leeward wing increases, thereby increasing the angle of attack normal to the leading edge. As a result, leading-edge separation should occur first on the leeward wing at a given model angle of attack. With this information, the first slope change most likely corresponds to the condition where leading-edge separation on the highly swept portion of the leeward wing occurs. The second slope change would be consistent with leading-edge separation on the highly swept portion of the windward wing. These physical changes occur for all configurations at all subsonic Mach numbers.

From figure 16 the effects of the nacelles on the flow for the curved wingtip model can readily be seen. An incremental change is produced by the nacelles, resulting in more positive yaw derivatives and more negative roll and side-force derivatives.

Pressure Data Results

Figures 17 through 19 show chordwise and spanwise pressure distribution results for three selected Mach numbers at several angles of attack for the curved wingtip model with nacelles on and off. In some cases data were not taken precisely at the same

angle of attack with nacelles on and off. This is a result of not having a balance present and having to rely on the method described previously in the "Measurements and Corrections" section to determine angle of attack. Such differences, if any, are noted in the figures. Subsonically, pressure coefficient levels at each of the chordwise and spanwise locations tended to increase with Mach number for a fixed angle of attack. Also, vortex development at a constant Mach number can be seen at the spanwise stations as angle of attack increases. This is indicated by the pressure peaks on the upper surface near $\eta = 0.6$ (see figs. 17(c)–(e), for example). This development occurs at all Mach numbers.

The only significant change in the pressure distributions due to the presence of nacelles occurred at B.L. 6.040 and M.S. 20.670 at all Mach numbers (figs. 17–19). At B.L. 6.040, which is outboard of the nacelles, pressure coefficients on the upper surface of the wing are more negative when nacelles are present. The increase in lift caused by the nacelles apparently produced an increase in upwash on the outer portion of the wing. At M.S. 20.670 (figs. 17–19) the effects of the nacelles on the lower surface of the wing can be clearly seen. As described previously, the nacelles have slowed the flow on the lower surface, resulting in more positive pressures and an increase in lift. Again, this effect can be seen at all Mach numbers and angles of attack.

Concluding Remarks

An aerodynamic data base was created for assessing the applicability of various levels of computational methods to analyze high-speed civil transport (HSCT) configurations. This was accomplished by testing two generic HSCT models in the Langley 8-Foot Transonic Pressure Tunnel. The two models differed geometrically only in the wingtip region, where one model had curved wingtips and the second had straight wingtips. Force and pressure data were obtained on the curved wingtip model, and force data only were obtained on the straight wingtip model from Mach 0.30 to 1.19. Both models were tested with flow-through engine nacelles on and off. Data obtained can be used to assess the accuracy of various levels of computational analysis on an HSCT configuration.

Test results indicate that for a given angle of attack the straight wingtip model produced slightly higher lift coefficients at the higher angles of attack tested and for a given lift coefficient, less pitching moment. The straight wingtip model also generated less induced drag. Pitch-up also occurred at

higher lift coefficients for the straight wingtip configuration. Data also indicate that adding nacelles to the lower surface of the wings increased lift, increased span efficiency, and improved lateral-directional stability. Pressure data obtained on the curved wingtip model indicated more negative pressure coefficient levels with increased subsonic Mach number and indicated vortical flow development as angle of attack increased. Pressure coefficients also indicated increased loading on the outer wing panel due to the presence of the nacelles.

NASA Langley Research Center
Hampton, VA 23681-0001
July 27, 1992

References

1. Boeing Commercial Airplanes, New Airplane Development: *High-Speed Civil Transport Study Summary*. NASA CR-4234, 1989.
2. Douglas Aircraft Co., New Commercial Programs: *Study of High-Speed Civil Transports—Summary*. NASA CR-4236, 1990.
3. *National Aeronautical R & D Goals—Agenda for Achievement*. Executive Off. of the President, Off. of Science and Technology Policy, Feb. 1987.
4. Dollyhigh, Samuel M.: Technology Issues for High-Speed Civil Transports. SAE Tech. Paper Ser. 892201, Sept. 1989.
5. Robins, A. Warner; Dollyhigh, Samuel M.; Beissner, Fred L., Jr.; Geiselhart, Karl; Martin, Glenn L.; Shields, E. W.; Swanson, E. E.; Coen, Peter G.; and Morris, Shelby J., Jr.: *Concept Development of a Mach 3.0 High-Speed Civil Transport*. NASA TM-4058, 1988.
6. Covell, Peter F.; Hernandez, Gloria; Flamm, Jeffrey D.; and Rose, Ollie J.: Supersonic Aerodynamic Characteristics of a Mach 3 High-Speed Civil Transport Configuration. AIAA-90-3210, Sept. 1990.
7. Pittman, James L.; Bonhaus, Daryl L.; Siclari, Michael J.; and Dollyhigh, Samuel M.: Euler Analysis of a High-Speed Civil Transport Concept at Mach 3. *J. Aircr.*, vol. 28, no. 4, Apr. 1991, pp. 239–245.
8. Vatsa, Veer N.; Turkel, Eli; and Abolhassani, J. S.: *Extension of Multigrid Methodology to Supersonic/Hypersonic 3-D Viscous Flows*. NASA CR-187612, ICASE Rep. No. 91-66, 1991.
9. Peñaranda, Frank E.; and Freda, M. Shannon: *Aeronautical Facilities Catalogue. Volume 1—Wind Tunnels*. NASA RP-1132, 1985.
10. Braslow, Albert L.; and Knox, Eugene C.: *Simplified Method for Determination of Critical Height of Distributed Roughness Particles for Boundary-Layer Transition at Mach Numbers From 0 to 5*. NACA TN 4363, 1958.

11. Belton, Pamela S.; and Campbell, Richard L.: *Experimental Study of a Generic High Speed Civil Transport—Tabulated Data*. NASA TM-104216, 1992.
12. Treadgold, D.; and Wilson, K. H.: Some Aerodynamic Interference Effects That Influence the Transonic Performance of Combat Aircraft. *Subsonic/Transonic Configuration Aerodynamics*, AGARD-CP-285, Sept. 1980, pp. 24-1-24-17.
13. Hensch, Michael J.; and Luckring, James M.: Connection Between Leading-Edge Sweep, Vortex Lift, and Vortex Strength for Delta Wings. *J. Aircr.*, vol. 27, no. 5, May 1990, pp. 473-475.

Table I. Wing Definition

(a) $y = 0.900$ in.; $c = 23.134$ in.; M.S. at L.E. = 1.963 in.; $r = 0.00567$ in.

x , in.	Upper surface z , in.	Lower surface z , in.
0.000000	-0.311864	-0.311863
1.535218	-.346691	-.346691
1.621048	-.352843	-.352842
1.923880	-.375728	-.375727
2.902939	-.452498	-.452497
4.359268	-.575437	-.575437
5.676326	-.682707	-.682706
6.643123	-.757530	-.757530
7.863940	-.849977	-.849977
8.281753	-.879993	-.879992
9.016973	-.929336	-.929335
10.107080	-.993679	-.993679
11.162483	-1.046540	-1.046539
12.180408	-1.094475	-1.094474
13.160857	-1.135928	-1.135927
14.086013	-1.174906	-1.174906
14.883234	-1.202767	-1.202767
15.804919	-1.231405	-1.231404
16.946152	-1.266037	-1.266037
18.293055	-1.296420	-1.296420
19.009071	-1.310433	-1.310432
19.728561	-1.322496	-1.322496
20.890383	-1.337642	-1.337641
21.981417	-1.350464	-1.350463
22.553770	-1.356110	-1.356110
23.134680	-1.362099	-1.362098

Table I. Continued

(b) $y = 1.120$ in.; $c = 22.037$ in.; M.S. at L.E. = 3.061 in.; $r = 0.00547$ in.

x , in.	Upper surface z , in.	Lower surface z , in.
0.000000	-0.430451	-0.430451
1.462362	-.414520	-.414520
1.544118	-.418280	-.418280
1.832580	-.433923	-.433923
2.765178	-.488388	-.488388
4.152395	-.588532	-.588532
5.406950	-.686525	-.686525
6.327868	-.758203	-.758203
7.490749	-.839014	-.839014
7.888734	-.865172	-.865172
8.589064	-.910249	-.910249
9.627437	-.973696	-.973696
10.632756	-1.028544	-1.028544
11.602375	-1.075686	-1.075686
12.536294	-1.116707	-1.116707
13.417546	-1.152331	-1.152331
14.176935	-1.179915	-1.179915
15.054880	1.209469	1.209469
16.141956	1.241468	1.241468
17.424938	1.273830	1.273830
18.106977	1.288760	1.288760
18.792322	1.302483	1.302483
19.899010	1.322617	1.322617
20.938267	1.339781	1.339781
21.483454	1.348441	1.348441
22.036798	1.357116	1.357116

Table I. Continued

(c) $y = 1.800$ in.; $c = 17.941$ in.; M.S. at L.E. = 7.157 in.; $r = 0.00558$ in.

x , in.	Upper surface z , in.	Lower surface z , in.
0.000000	-0.546906	-0.546906
1.190546	-.512697	-.512697
1.257107	-.513467	-.513467
1.491950	-.517694	-.517694
2.251201	-.538320	-.538320
3.380570	-.589818	-.589818
4.401935	-.647328	-.647328
5.151678	-.694195	-.694195
6.098410	-.756497	-.756497
6.422420	-.778284	-.778284
6.992576	-.816832	-.816832
7.837941	-.874076	-.874076
8.656398	-.928197	-.928197
9.445789	-.979066	-.979066
10.206117	-1.026524	-1.026524
10.923566	-1.069717	-1.069717
11.541801	-1.104819	-1.104819
12.256561	-1.143514	-1.143514
13.141579	-1.187968	-1.187968
14.186085	1.235363	1.235363
14.741351	1.257991	1.257991
15.299308	1.278357	1.278357
16.200291	1.306551	1.306551
17.046375	1.329233	1.329233
17.490229	1.340301	1.340301
17.940720	1.351618	1.351618

Table I. Continued

(d) $y = 2.400$ in.; $c = 14.912$ in.; M.S. at L.E. = 10.202 in.; $r = 0.00397$ in.

x , in.	Upper surface z , in.	Lower surface z , in.
0.000000	-0.786224	-0.786224
.989539	-.724401	-.724401
1.044862	-.723093	-.723093
1.240055	-.719749	-.719749
1.871118	-.718416	-.718416
2.809808	-.735016	-.735016
3.658731	-.763328	-.763328
4.281889	-.789027	-.789027
5.068778	-.827170	-.827170
5.338083	-.841295	-.841295
5.811977	-.866823	-.866823
6.514616	-.906092	-.906092
7.194885	-.945457	-.945457
7.851000	-.984014	-.974014
8.482956	-1.021177	-1.021177
9.079275	-1.055918	-1.055918
9.593131	-1.085624	-1.085624
10.187213	-1.119242	-1.119242
10.922805	-1.159812	-1.159812
11.790964	1.205435	1.205435
12.252480	1.228595	1.228595
12.716233	1.250157	1.250157
13.465097	1.282096	1.282096
14.168332	1.309932	1.309932
14.537248	1.324489	1.324489
14.911679	1.338683	1.338683

Table I. Continued

(e) $y = 3.240$ in.; $c = 10.760$ in.; M.S. at L.E. = 14.721 in.; $r = 0.00332$ in.

x , in.	Upper surface z , in.	Lower surface z , in.
0.000000	-0.975824	-0.975824
.714052	-.916581	-.916581
.753973	-.914493	-.914493
.894824	-.908005	-.908005
1.350200	-.894812	-.894812
2.027560	-.887991	-.887991
2.640143	-.888338	-.888338
3.089814	-.894011	-.894011
3.657635	-.906314	-.906314
3.851965	-.911425	-.911425
4.193927	-.920980	-.920980
4.700951	-.937589	-.937589
5.191835	-.955338	-.955338
5.665288	-.974284	-.974284
6.121308	-.993921	-.993921
6.551611	-1.012989	-1.012989
6.922411	-1.029730	-1.029730
7.351100	-1.049372	-1.049372
7.881905	-1.073995	-1.073995
8.508368	-1.102027	-1.102027
8.841399	-1.117642	-1.117642
9.176044	-1.132790	-1.132790
9.716425	-1.154786	-1.154786
10.223880	-1.174958	-1.174958
10.490089	-1.185916	-1.185916
10.760280	-1.196411	-1.196411

Table I. Continued

(f) $y = 4.104$ in.; $c = 6.642$ in.; M.S. at L.E. = 19.240 in.; $r = 0.00346$ in.

x , in.	Upper surface z , in.	Lower surface z , in.
0.000000	-1.079943	-1.079943
.440755	-1.042277	-1.042277
.406540	-1.040644	-1.040644
.552338	-1.033818	-1.033818
.833423	-1.017775	-1.017775
1.251529	-1.004517	-1.004517
1.629652	-.997975	-.997975
1.907216	-.994311	-.994311
2.257708	-.991025	-.991025
2.377661	-.990354	-.990354
2.588740	-.988796	-.988796
2.901704	-.986524	-.986524
3.204707	-.984991	-.984991
3.496950	-.985023	-.985023
3.778433	-.984204	-.984202
4.044043	-.984628	-.984628
4.272921	-.984003	-.984003
4.537534	-.984176	-.984176
4.865177	-.984563	-.984563
5.251867	-.985937	-.985937
5.457434	-.987515	-.987515
5.663997	-.988237	-.988237
5.997551	-.986773	-.986773
6.310782	-.988488	-.988488
6.475102	-.989948	-.989948
6.641880	-.990961	-.990961

Table I. Continued

(g) $y = 4.800$ in.; $c = 5.678$ in.; M.S. at L.E. = 20.560 in.; $r = 0.00553$ in.

x , in.	Upper surface z , in.	Lower surface z , in.
0.000000	-0.960001	-0.960001
.376787	-.956774	-.956774
.397852	-.956601	-.956601
.472176	-.955991	-.955991
.712465	.954169	-.954169
1.069890	-.952149	-.952149
1.393134	-.950571	-.950571
1.630415	-.949428	-.949428
1.930038	-.947958	-.947958
2.032582	-.947398	-.947398
2.213026	-.946437	-.946437
2.480569	-.945185	-.945185
2.739596	-.944218	-.944218
2.989424	-.943491	-.943491
3.230056	-.942941	-.942941
3.457115	-.942579	-.942579
3.652776	-.942317	-.942317
3.878984	-.942239	-.942239
4.159077	-.942296	-.942296
4.489645	-.942122	-.942122
4.665377	-.942043	-.942043
4.841960	-.942076	-.942076
5.127104	-.942370	-.942370
5.394876	-.942948	-.942948
5.535348	-.943348	-.943348
5.677920	-.943987	-.943987

Table I. Continued

(h) $y = 6.360$ in.; $c = 4.278$ in.; M.S. at L.E. = 22.773 in.; $r = 0.00000$ in.

x , in.	Upper surface z , in.	Lower surface z , in.
0.000000	-0.780487	-0.780487
.283904	-.789043	-.789043
.299777	-.789504	-.789504
.355778	-.791107	-.791101
.536833	-.796067	-.796067
.806149	-.802859	-.802859
1.049708	-.808570	-.808570
1.228496	-.812596	-.812596
1.454260	-.817391	-.817391
1.531524	-.818926	-.818926
1.667486	-.821613	-.821613
1.869078	-.825291	-.825291
2.064251	-.828544	-.828544
2.252494	-.831316	-.831316
2.433805	-.833680	-.833680
2.604892	-.835729	-.835729
2.752320	-.837137	-.837137
2.922765	-.838348	-.838348
3.133811	-.839608	-.839608
3.382890	-.840662	-.840662
3.515301	-.840864	-.840864
3.648355	-.841044	-.841044
3.863208	-.841375	-.841375
4.064970	-.841719	-.841719
4.170814	-.841962	-.841962
4.278240	-.841948	-.841948

Table I. Continued

(i) $y = 8.160$ in.; $c = 3.032$ in.; M.S. at L.E. = 25.259 in.; $r = 0.00000$ in.

x , in.	Upper surface z , in.	Lower surface z , in.
0.000000	-0.672000	-0.672000
.201191	-.674608	-.674608
.212438	-.674765	-.674765
.252125	-.675314	-.675314
.380430	-.677045	-.677045
.571282	-.679462	-.679462
.743882	-.681484	-.681484
.870581	-.682988	-.682988
1.030570	-.684823	-.684823
1.085323	-.685471	-.685471
1.181675	-.686476	-.686476
1.324533	-.688090	-.688090
1.462843	-.689624	-.689624
1.596242	-.690966	-.690966
1.724730	-.691800	-.691800
1.845972	-.692652	-.692652
1.950448	-.693475	-.693475
2.071235	-.694147	-.694147
2.220793	-.694395	-.694395
2.397305	-.694966	-.694966
2.491139	-.695303	-.695303
2.585428	-.695358	-.695358
2.737685	-.695064	-.695064
2.880665	-.694782	-.694782
2.955672	-.695013	-.695013
3.031800	-.695586	-.695586

Table I. Continued

(j) $y = 8.640$ in.; $c = 2.572$ in.; M.S. at L.E. = 26.357 in.; $r = 0.00000$ in.

x , in.	Upper surface z , in.	Lower surface z , in.
0.000000	-0.707999	-0.707999
.170683	-.708033	-.708033
.180226	-.708040	-.708040
.213894	-.708064	-.708064
.322745	-.708144	-.708144
.484657	-.708233	-.708233
.631086	-.708423	-.708423
.738572	-.708651	-.708651
.874302	-.708896	-.708896
.920753	-.709031	-.709031
1.002494	-.709292	-.709292
1.123691	-.709704	-.709704
1.241029	-.710116	-.710116
1.354200	-.710559	-.710559
1.463204	-.710989	-.710989
1.566062	-.711366	-.711366
1.654697	-.711658	-.711658
1.757168	-.712090	-.712090
1.884049	-.712637	-.712637
2.033795	-.713017	-.713017
2.113400	-.713093	-.713093
2.193393	-.713105	-.713105
2.322563	-.713052	-.713052
2.443862	-.712963	-.712963
2.507495	-.712874	-.712874
2.572080	-.712748	-.712748

Table I. Concluded

(k) $y = 9.036$ in.; $c = 1.008$ in.; M.S. at L.E. = 28.608 in.; $r = 0.00000$ in.

x , in.	Upper surface z , in.	Lower surface z , in.
0.000000	0.723127	0.723127
.066890	.722951	.722951
.070631	.722941	.722941
.083825	.722906	.722906
.126484	.722794	.722794
.189937	.722627	.722627
.247322	.722475	.722475
.289447	.722365	.722365
.342640	.722225	.722225
.360844	.722177	.722177
.392878	.722092	.722092
.440375	.721967	.721967
.486360	.721846	.721846
.530712	.721730	.721730
.573431	.721617	.721617
.613741	.721511	.721511
.648476	.721419	.721419
.688636	.721313	.721313
.738360	.721182	.721182
.797046	.721028	.721028
.828244	.720946	.720946
.859592	.720863	.720863
.910214	.720730	.720730
.957751	.720605	.720605
.982690	.720539	.720539
1.008000	.720473	.720473

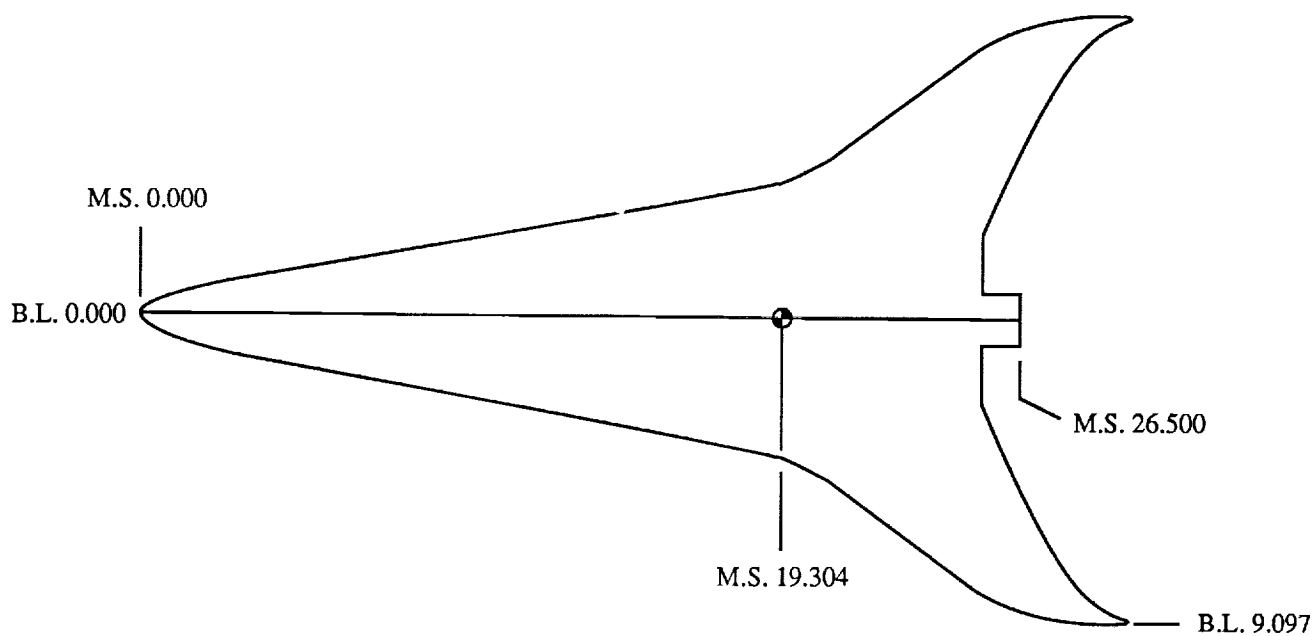
Table II. Pressure Orifice Locations

Orifice	x , in.	y , in.	Orifice	x , in.	y , in.
CP1	8.875	0.000	CP34	20.670	3.522
CP2	8.875	.352	CP35	20.670	3.874
CP3	8.875	.705	CP36	20.670	4.226
CP4	8.875	1.057	CP37	20.670	4.578
CP5	8.887	1.409	CP39	23.000	6.040
CP6	8.875	1.762	CP40	23.473	6.040
CP7	8.875	2.114	CP41	23.945	6.040
CP8	10.560	2.114	CP42	24.419	6.040
CP9	12.245	2.114	CP43	24.892	6.040
CP10	13.930	2.114	CP44	25.366	6.040
CP11	15.615	.000	*CP45	20.670	-1.410
CP12	15.615	.352	*CP46	20.670	-1.762
CP13	15.615	.705	*CP47	20.670	-2.114
CP14	15.616	1.057	*CP48	20.670	-2.466
CP15	15.615	1.409	*CP49	20.670	-2.818
CP16	15.615	1.762	*CP50	20.670	-4.000
CP17	15.615	2.114	*CP51	23.000	-3.800
CP18	15.615	2.466	*CP52	23.000	-3.600
CP19	15.615	2.818	*CP53	23.000	-3.400
CP20	15.615	3.170	*CP54	23.000	-3.200
CP21	15.615	3.303	*CP55	23.000	-3.000
CP22	17.300	2.114	*CP56	23.000	-1.200
CP23	18.985	2.114	*CP57	23.000	-1.000
CP24	20.670	.000	*CP58	23.000	-.800
CP25	20.670	.352	*CP59	23.000	-.600
CP26	20.670	.705	*CP60	23.000	-.400
CP27	20.670	1.057	*CP61	24.000	-2.060
CP28	20.670	1.409	CP62	26.000	.000
CP29	20.670	1.762	CP63	26.000	† _{min}
CP30	20.670	2.114	CP64	26.000	‡ _{max}
CP32	20.670	2.818	CP65	26.000	.000
CP33	20.670	3.170			

*Lower surface orifices.

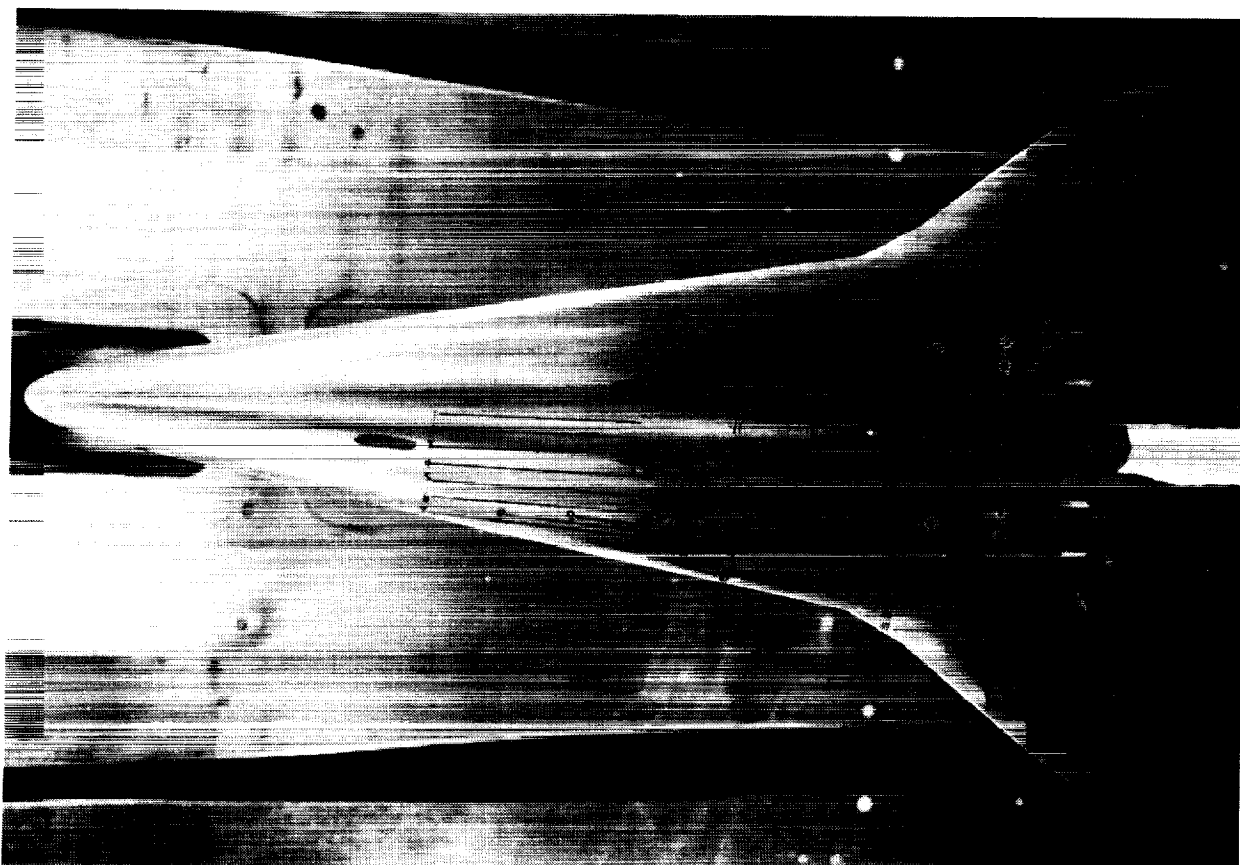
†Minimum vertical distance.

‡Maximum vertical distance.



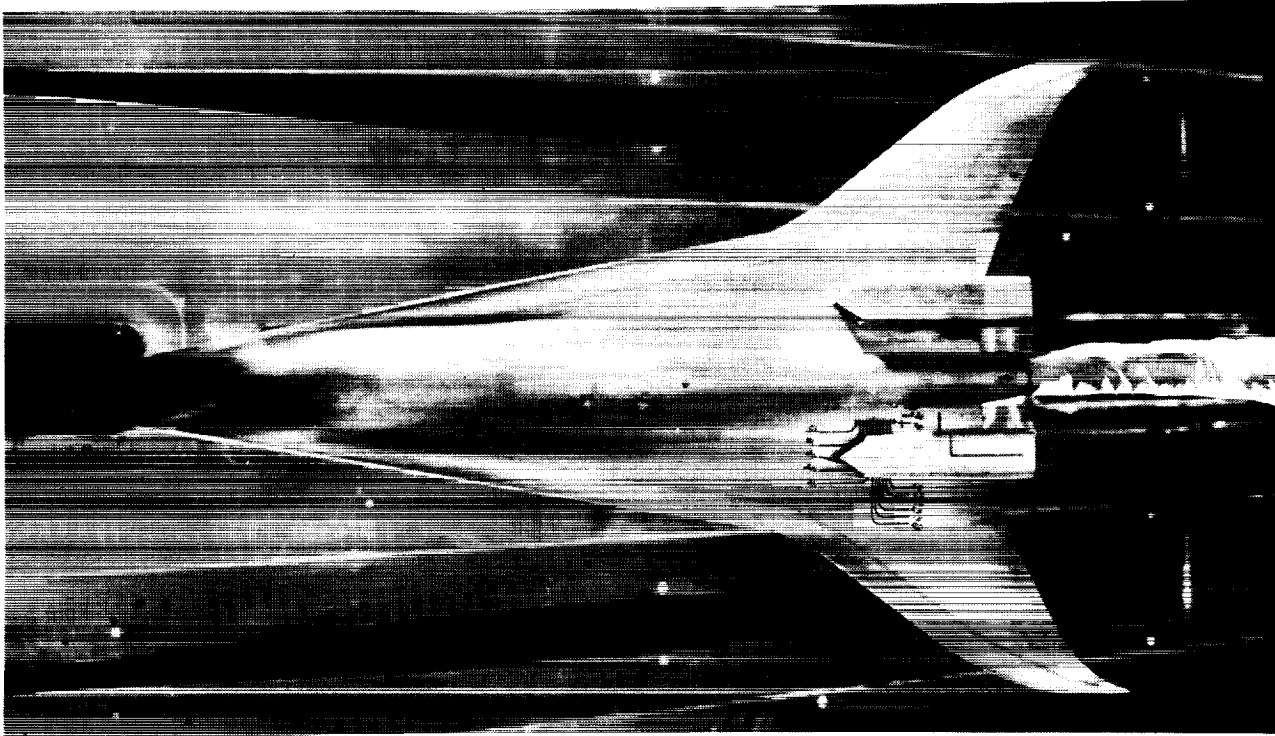
ORIGINAL PAGE
BLACK AND WHITE PHOTOGRAPH

Figure 1. Curved wingtip model.



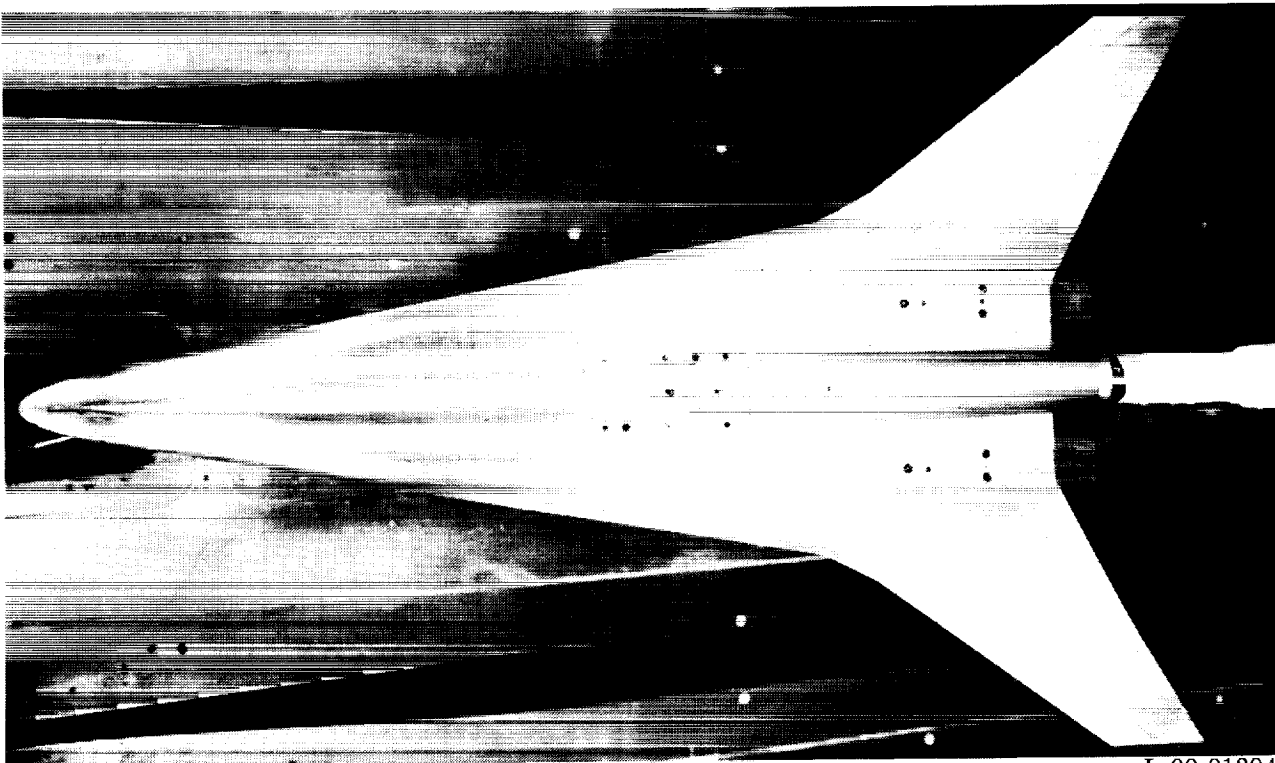
L-90-2745

Figure 2. Curved wingtip model installed in Langley 8-Foot Transonic Pressure Tunnel.



L-90-02749

Figure 3. Curved wingtip model, inverted, in Langley 8-Foot Transonic Pressure Tunnel.



L-90-01304

Figure 4. Straight wingtip model in Langley 8-Foot Transonic Pressure Tunnel.

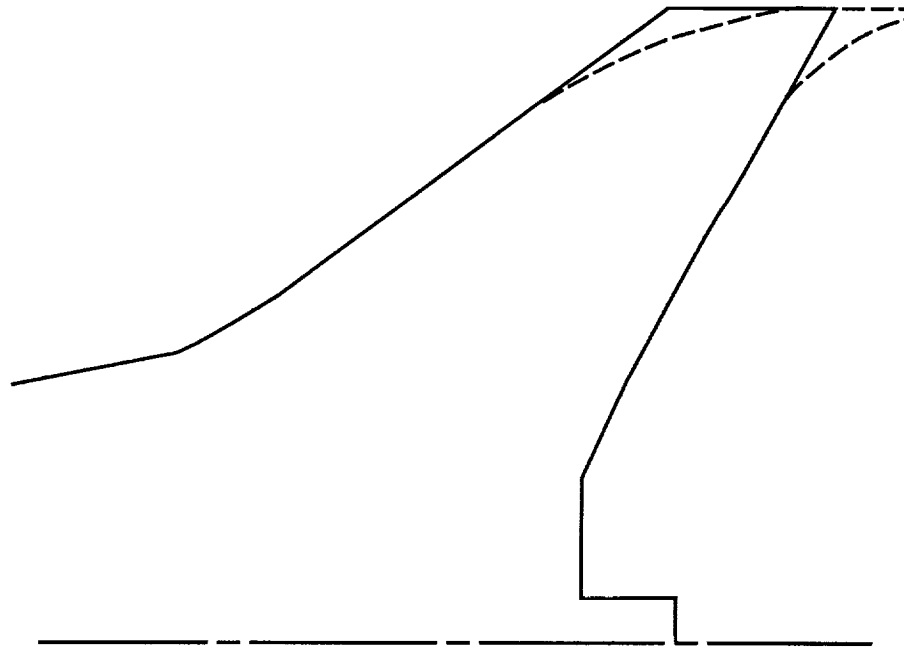


Figure 5. Comparison of curved and straight wingtips.

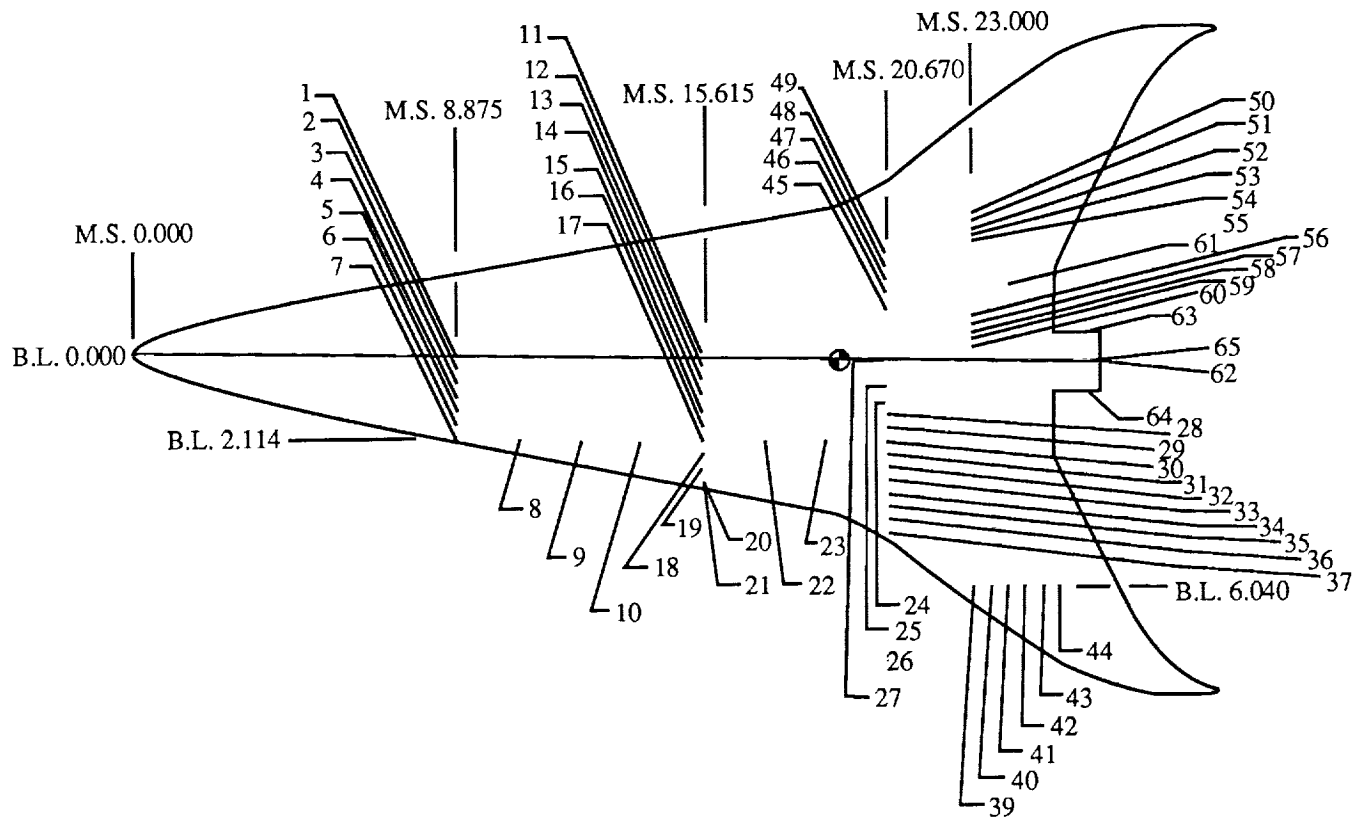
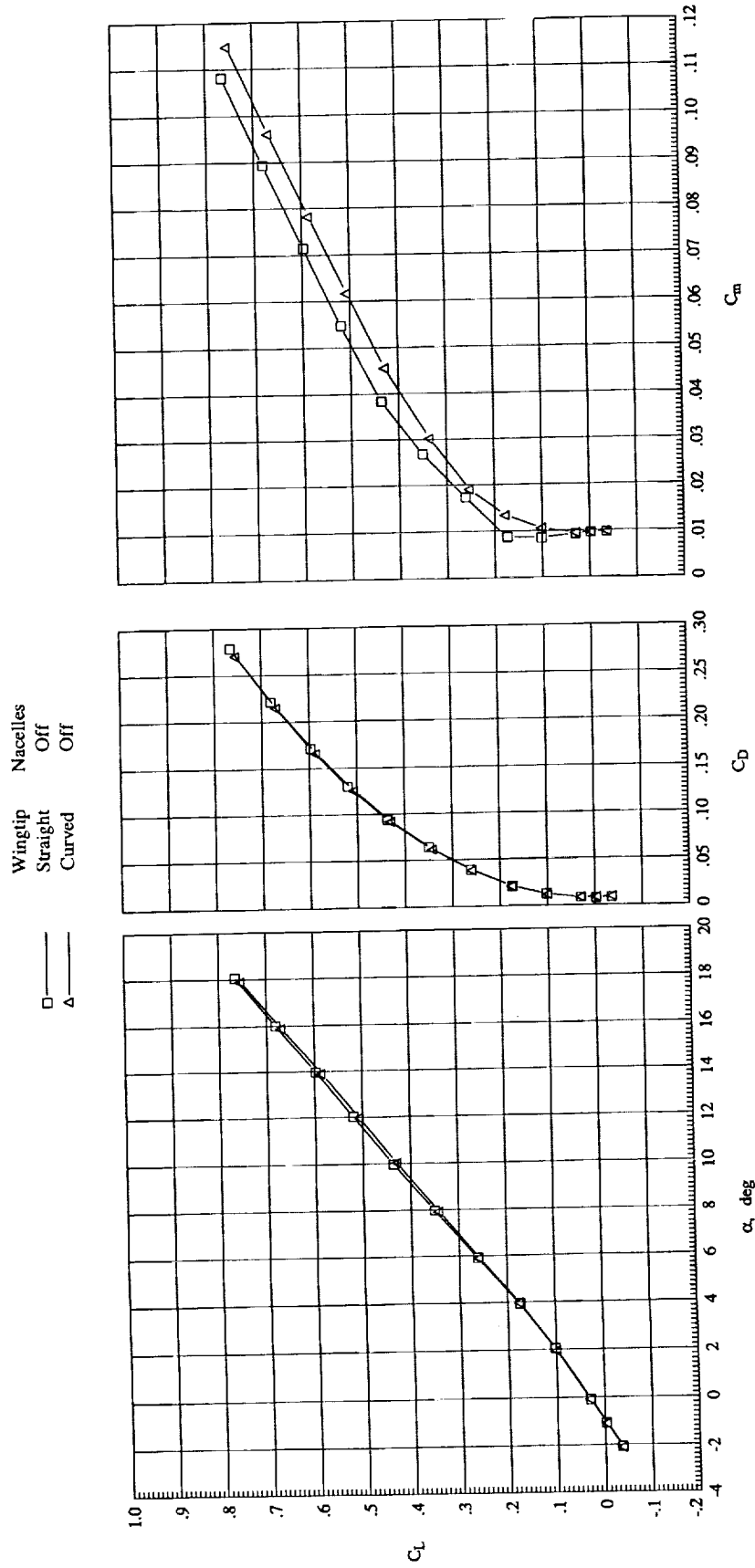
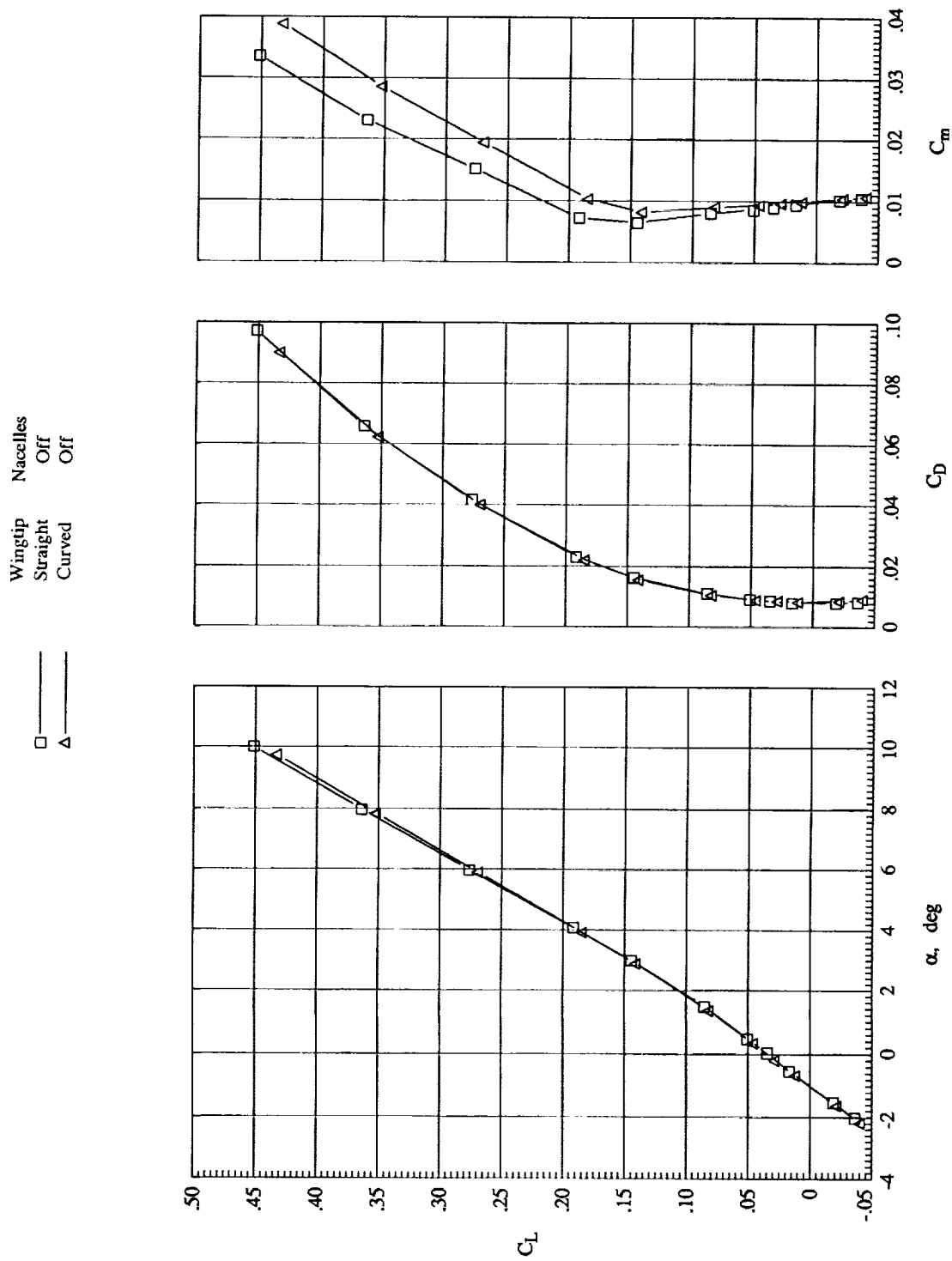


Figure 6. Pressure orifice arrangement for the curved wingtip model.



(a) $M_\infty = 0.30$.

Figure 7. Longitudinal characteristics of the straight and curved wingtip models with $\beta = 0^\circ$ and nacelles off.

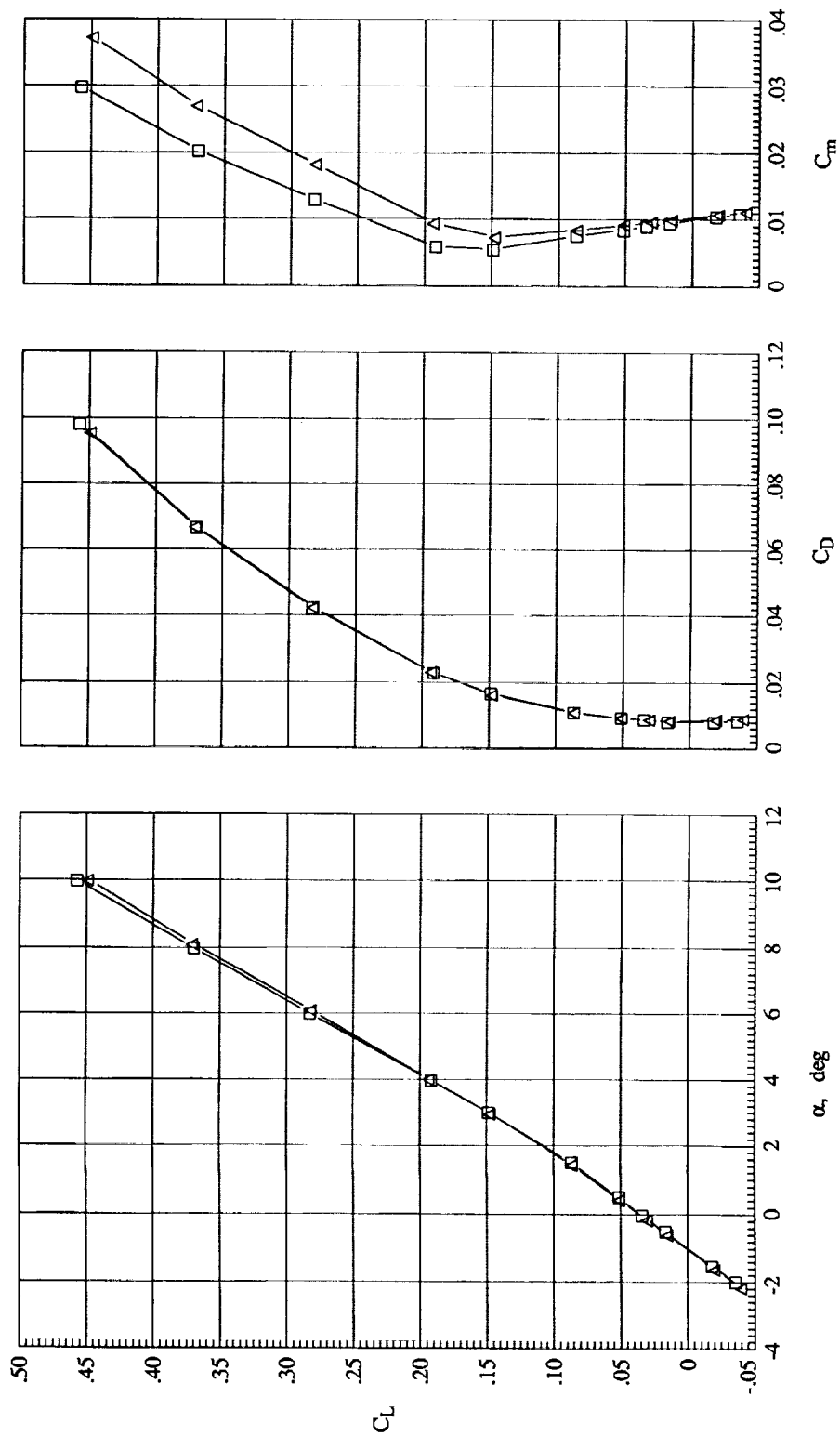


(b) $M_\infty = 0.60$.

Figure 7. Continued.

Wingtip Nacelles
 Straight Off
 Curved Off

□ —
 Δ —



(c) $M_\infty = 0.70$.

Figure 7. Continued.

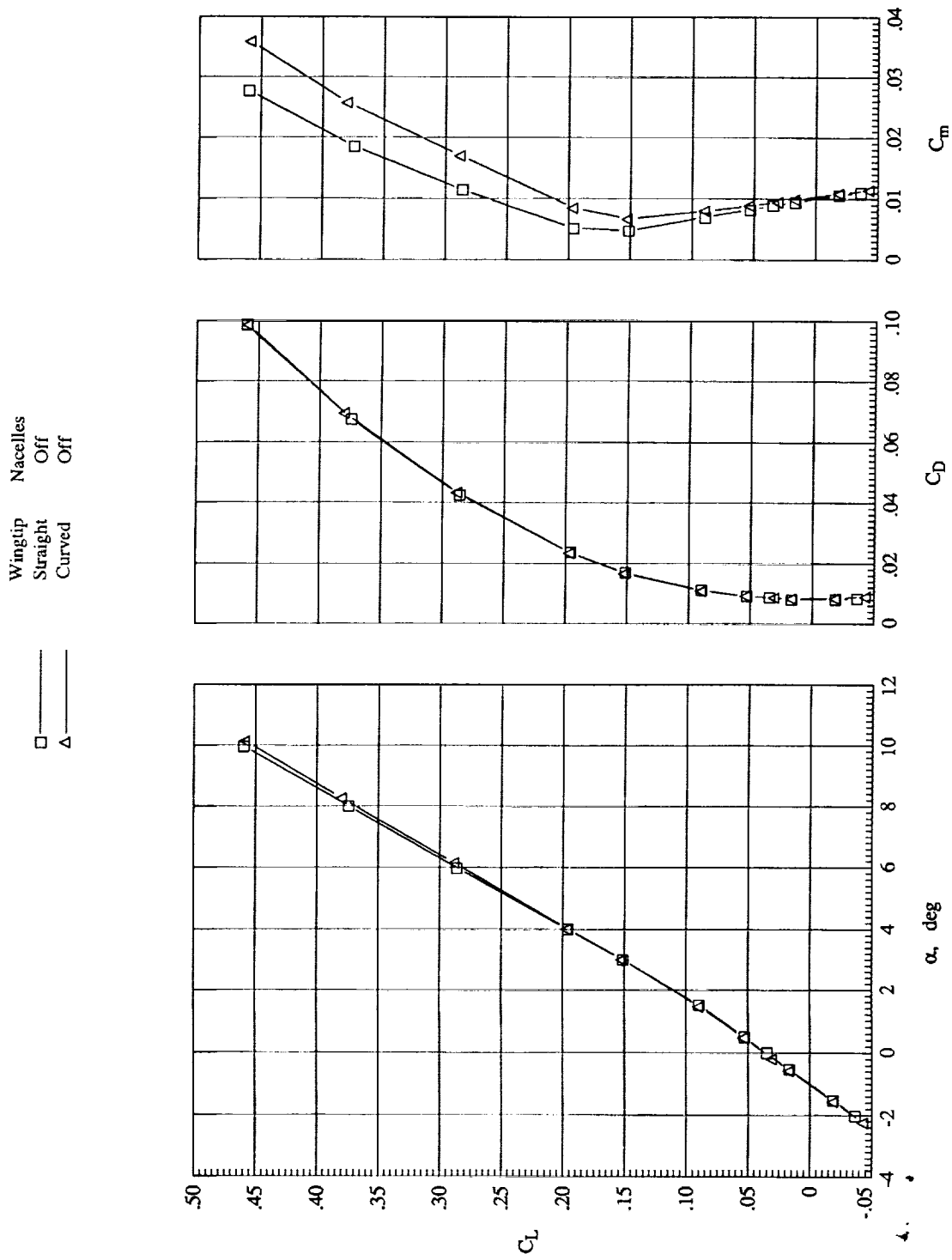
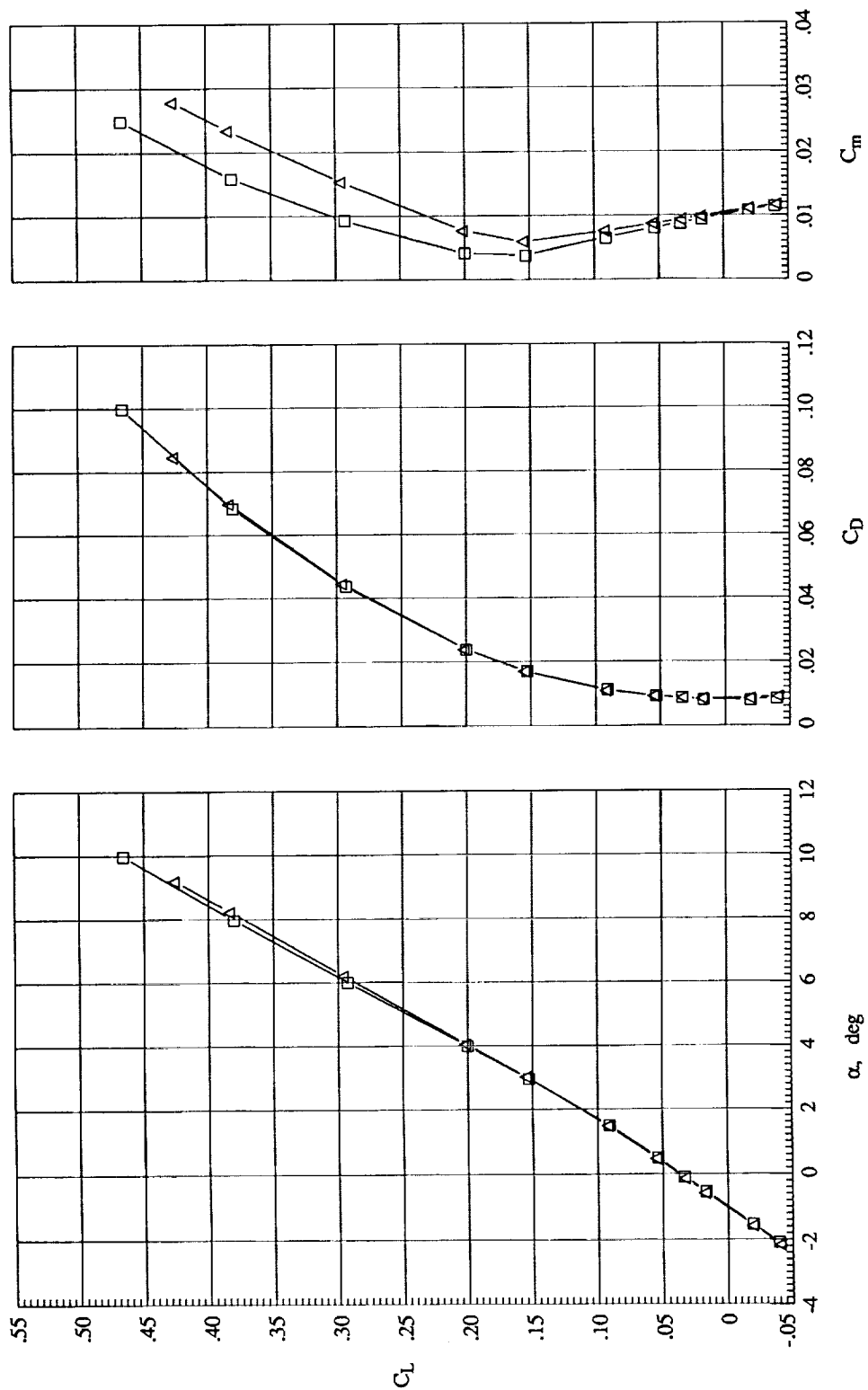
(d) $M_\infty = 0.75$.

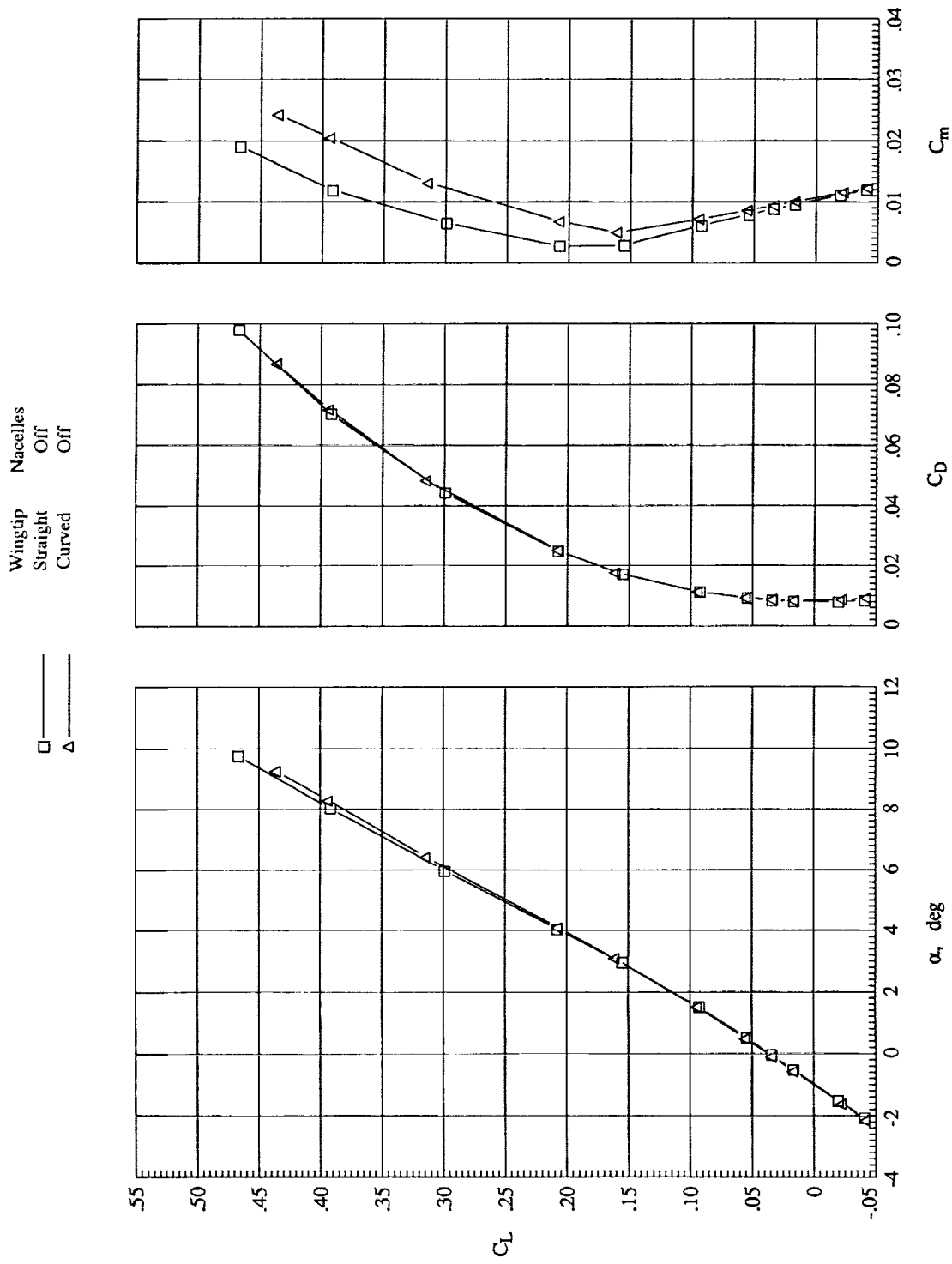
Figure 7. Continued.

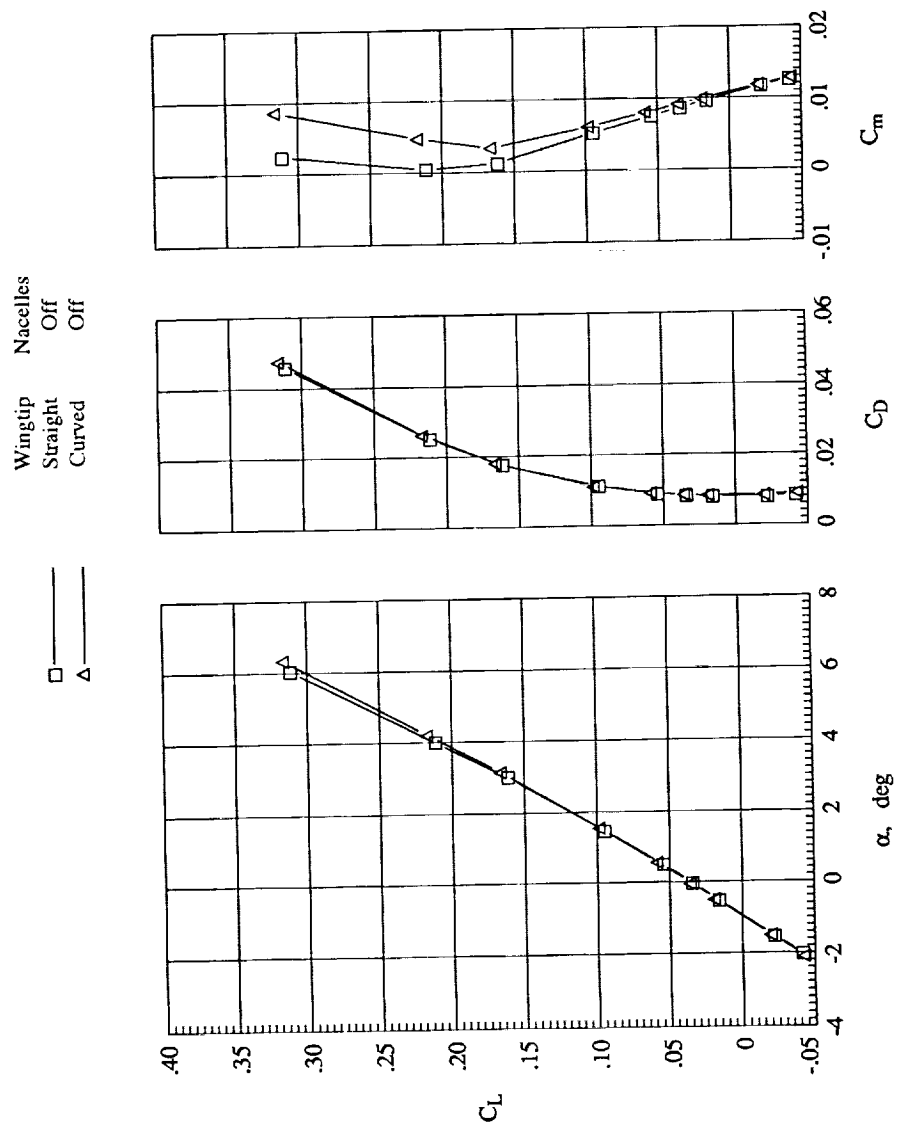
Wingtip Nacelles
 Straight Off
 Curved Off

□ —
 Δ —



(e) $M_\infty = 0.80$.
 Figure 7. Continued.





(g) $M_\infty = 0.90$.

Figure 7. Continued.

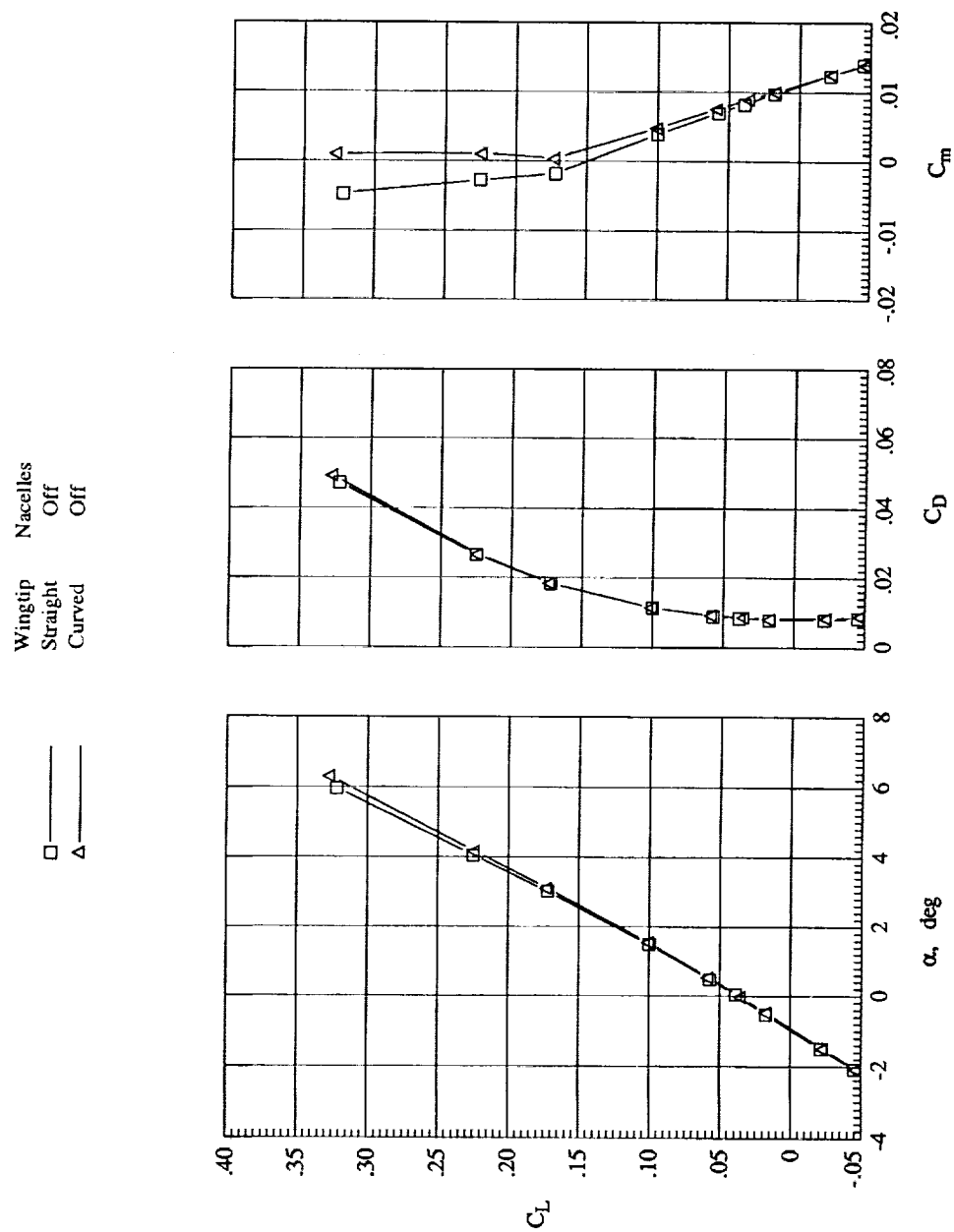
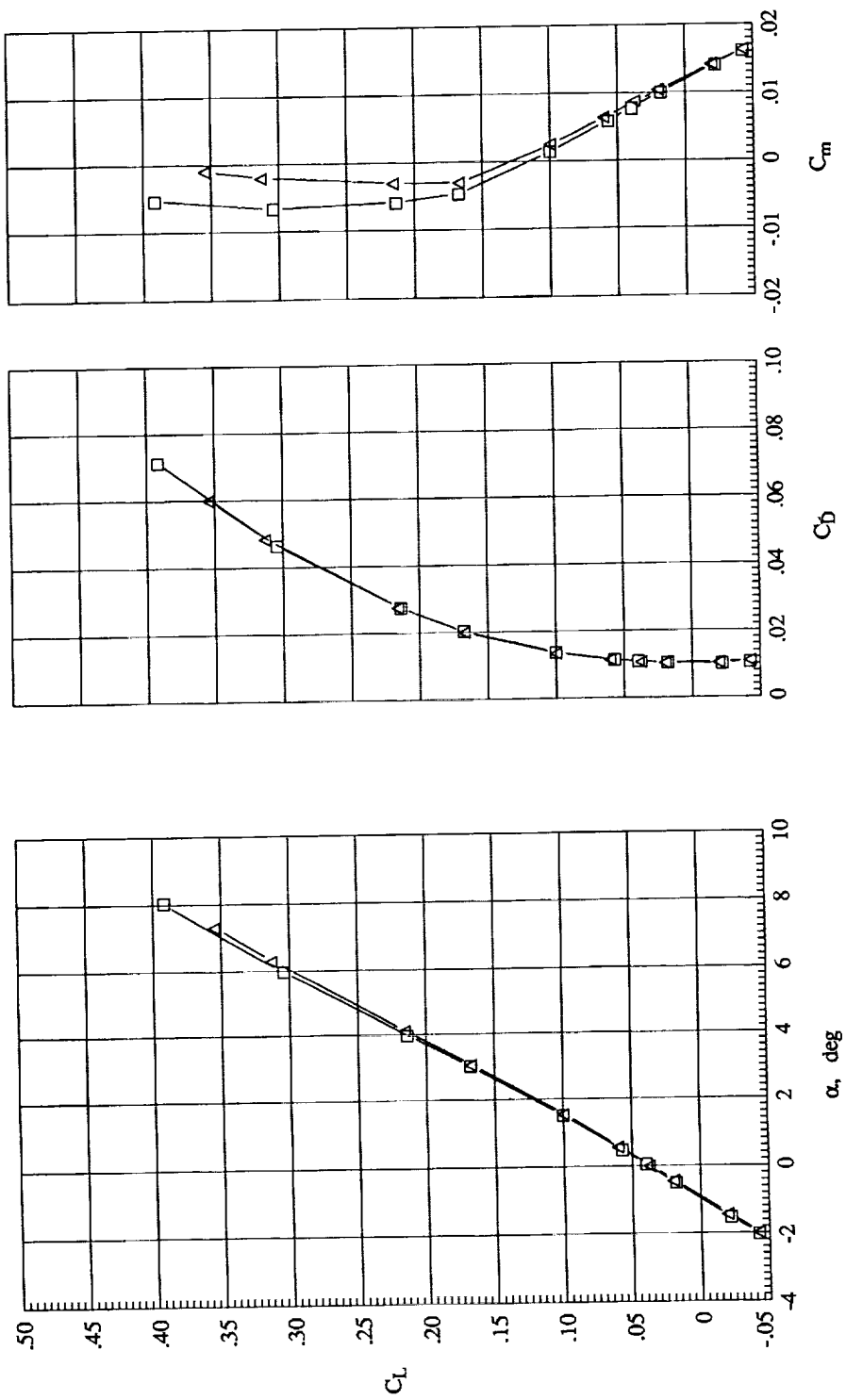
(h) $M_\infty = 0.95$.

Figure 7. Continued.

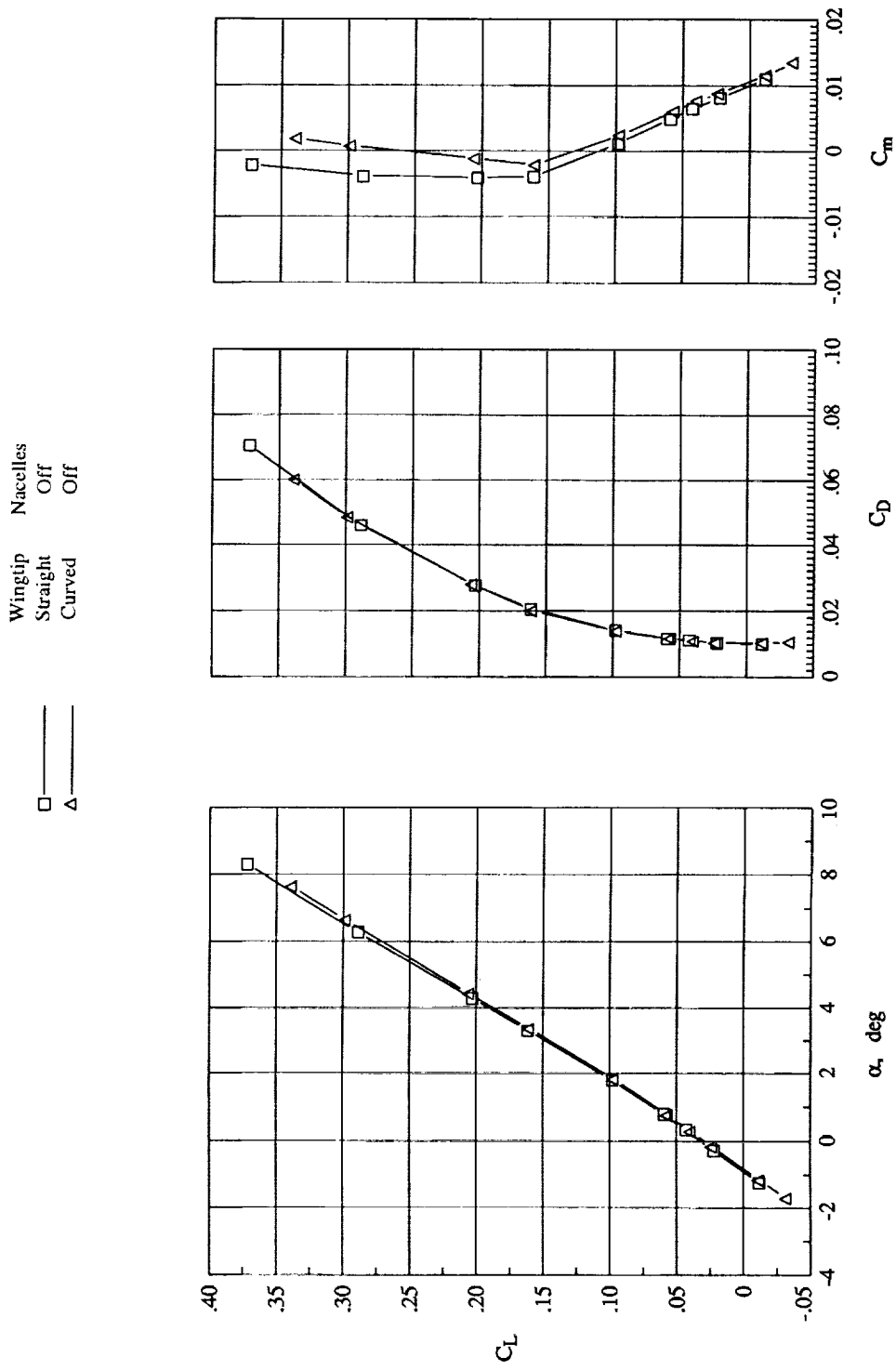
Wingtip Nacelles
 Straight Off
 Curved Off

□
 △



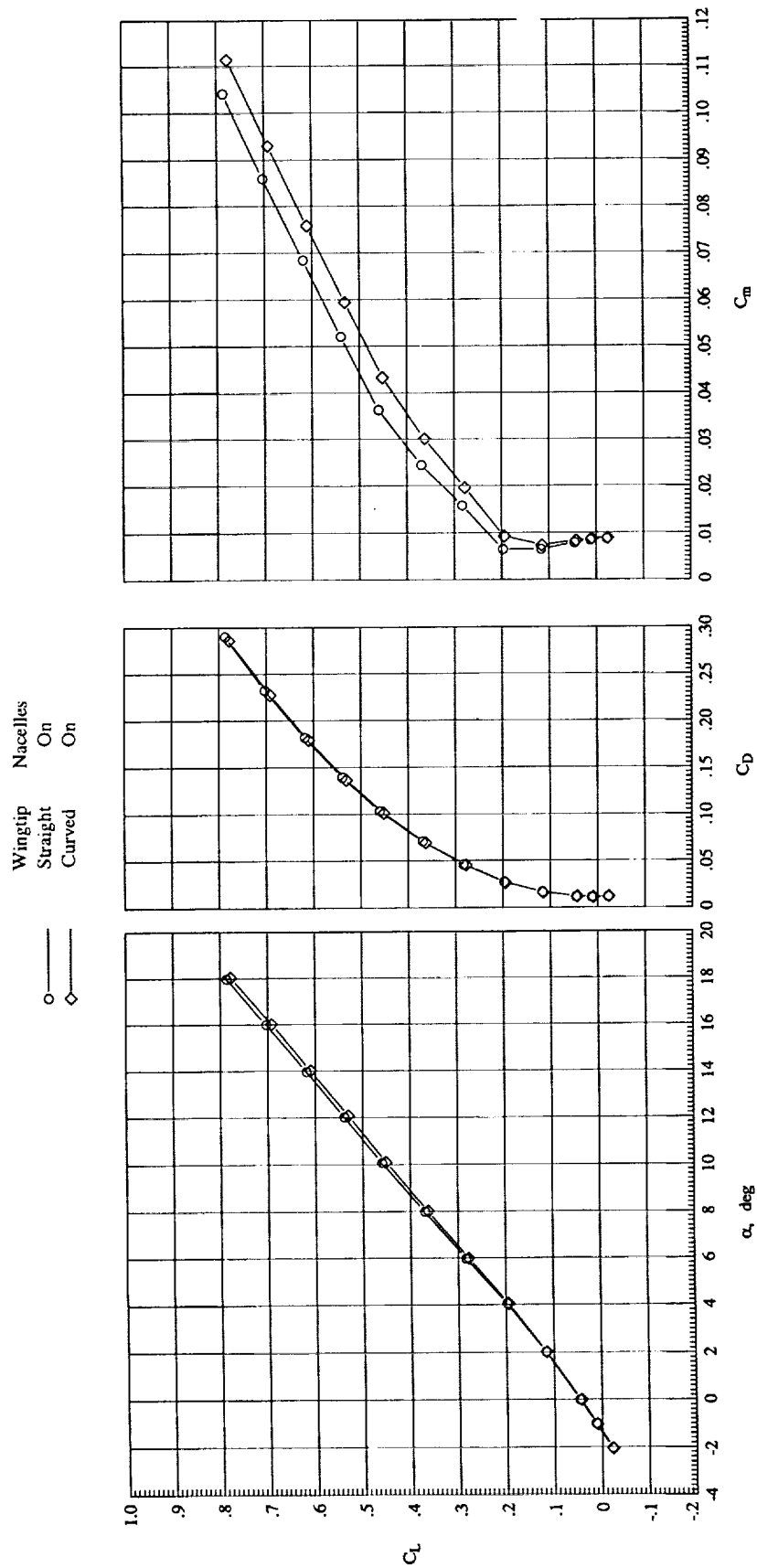
(i) $M_{\infty} = 1.10$.

Figure 7. Continued.



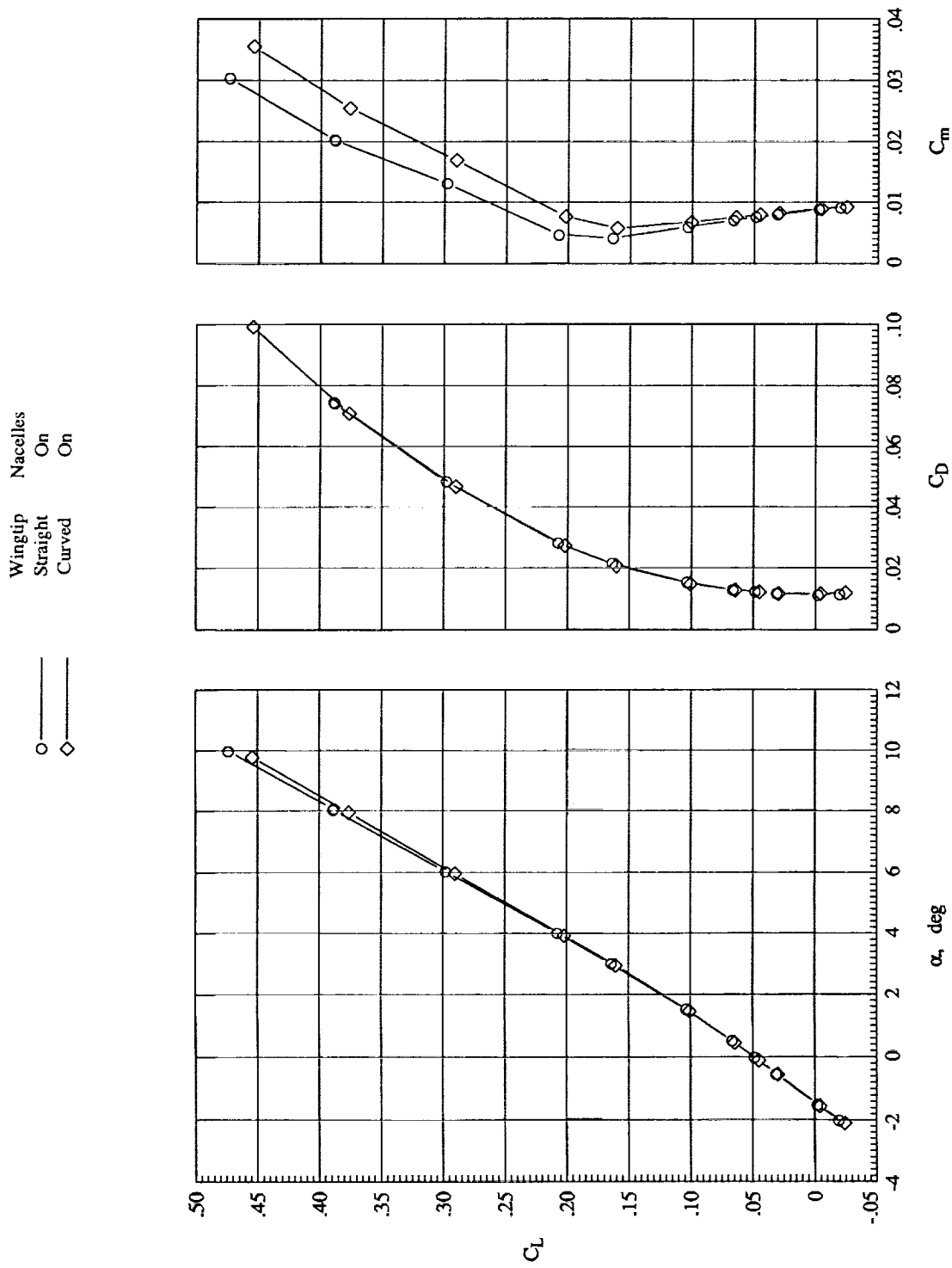
(i) $M_\infty = 1.19$.

Figure 7. Concluded.



(a) $M_\infty = 0.30$.

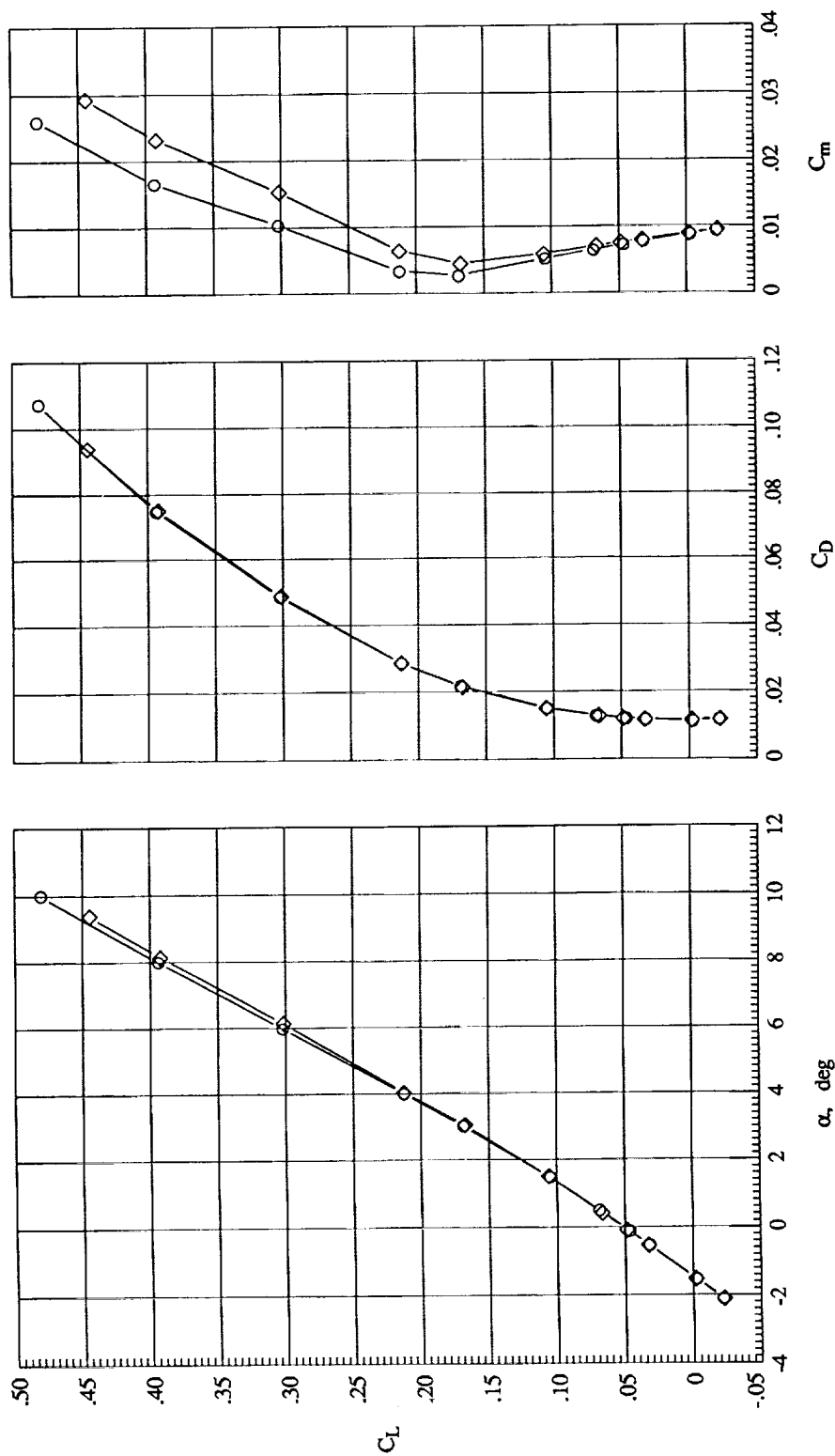
Figure 8. Longitudinal characteristics of the straight and curved wingtip models with $\beta = 0^\circ$ and nacelles on.



(b) $M_\infty = 0.60$.

Figure 8. Continued.

Wingtip Nacelles
 Straight On
 Curved On



(c) $M_\infty = 0.70$.

Figure 8. Continued.

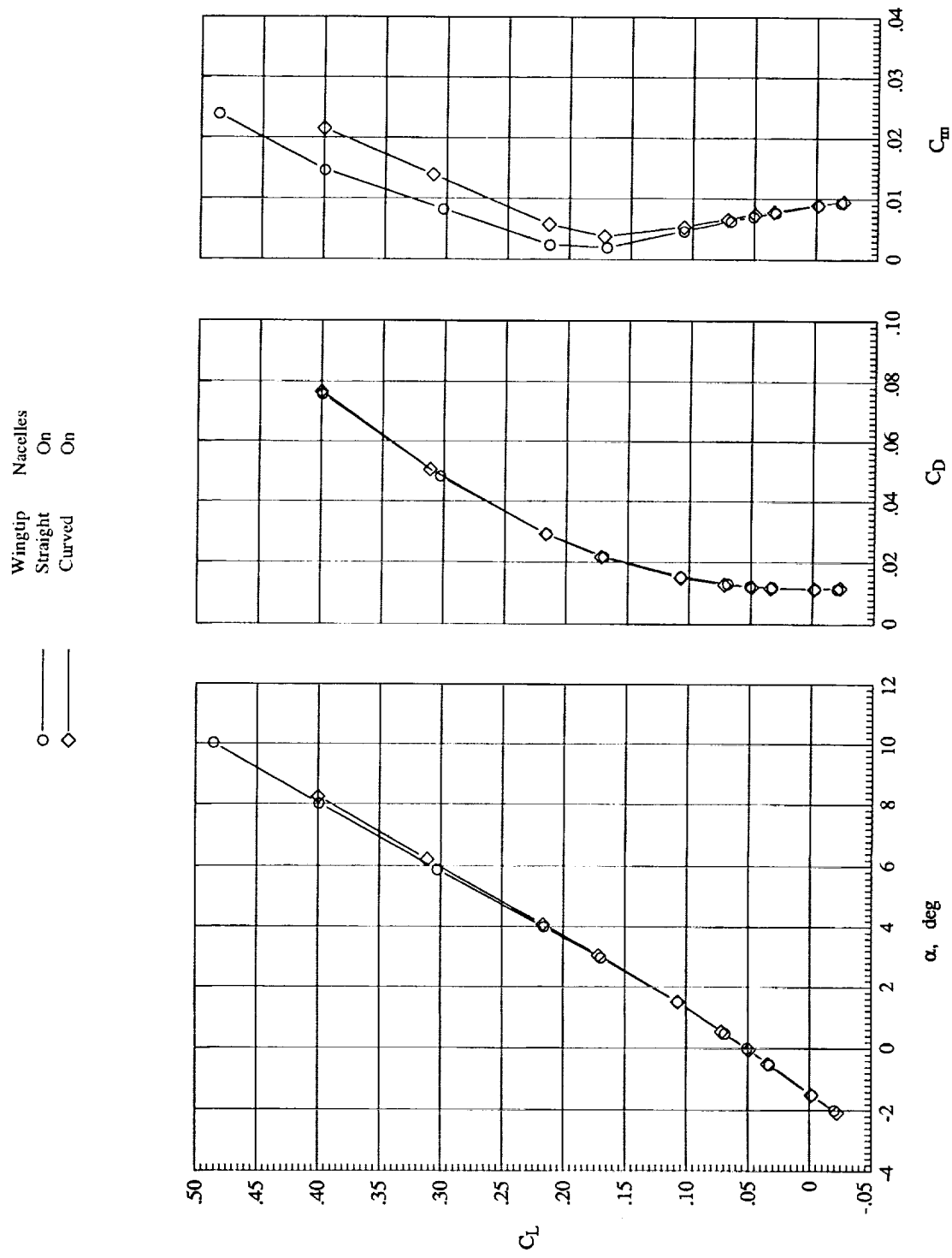
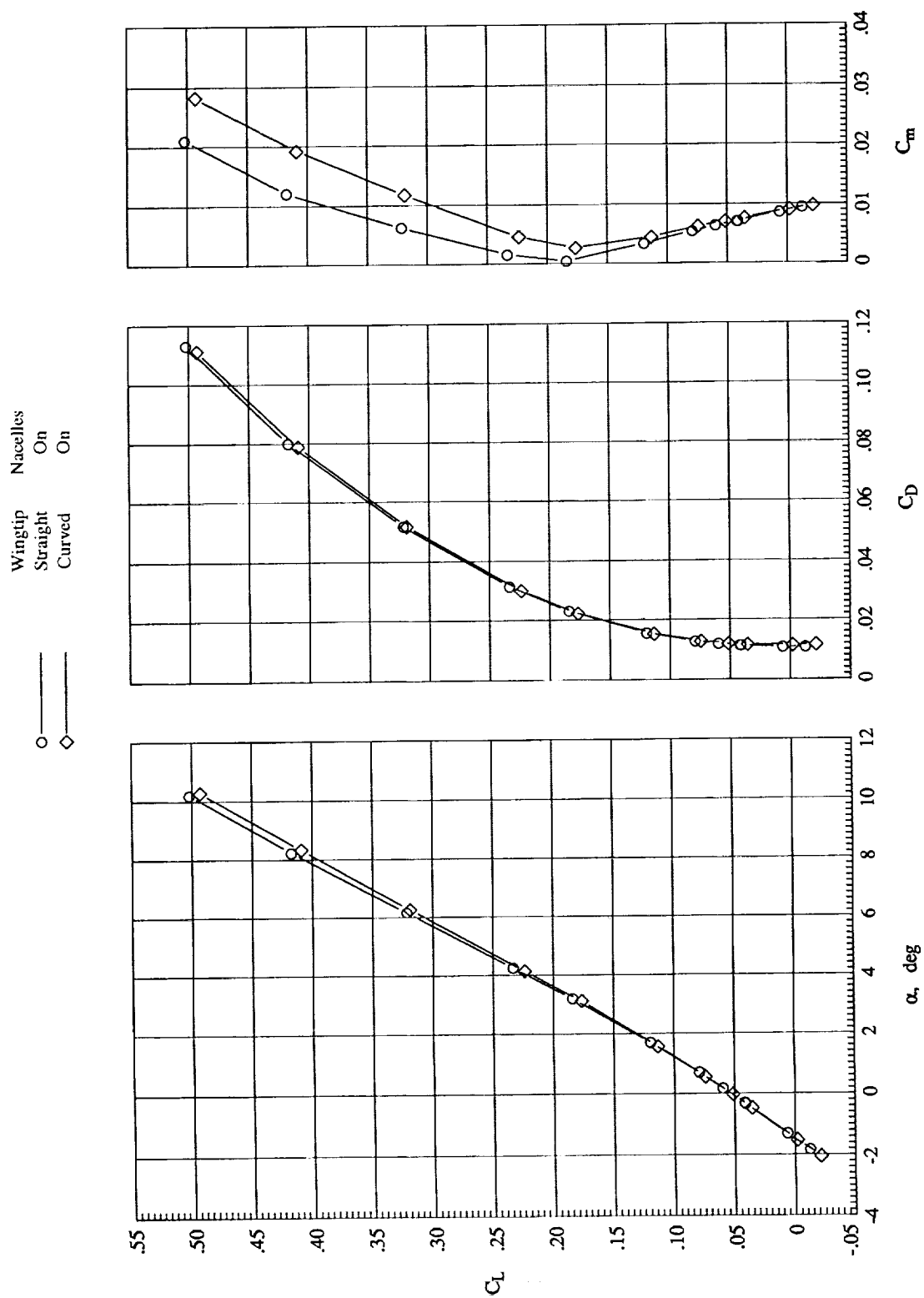
(d) $M_\infty = 0.75$.

Figure 8. Continued.



(e) $M_\infty = 0.80$.

Figure 8. Continued.

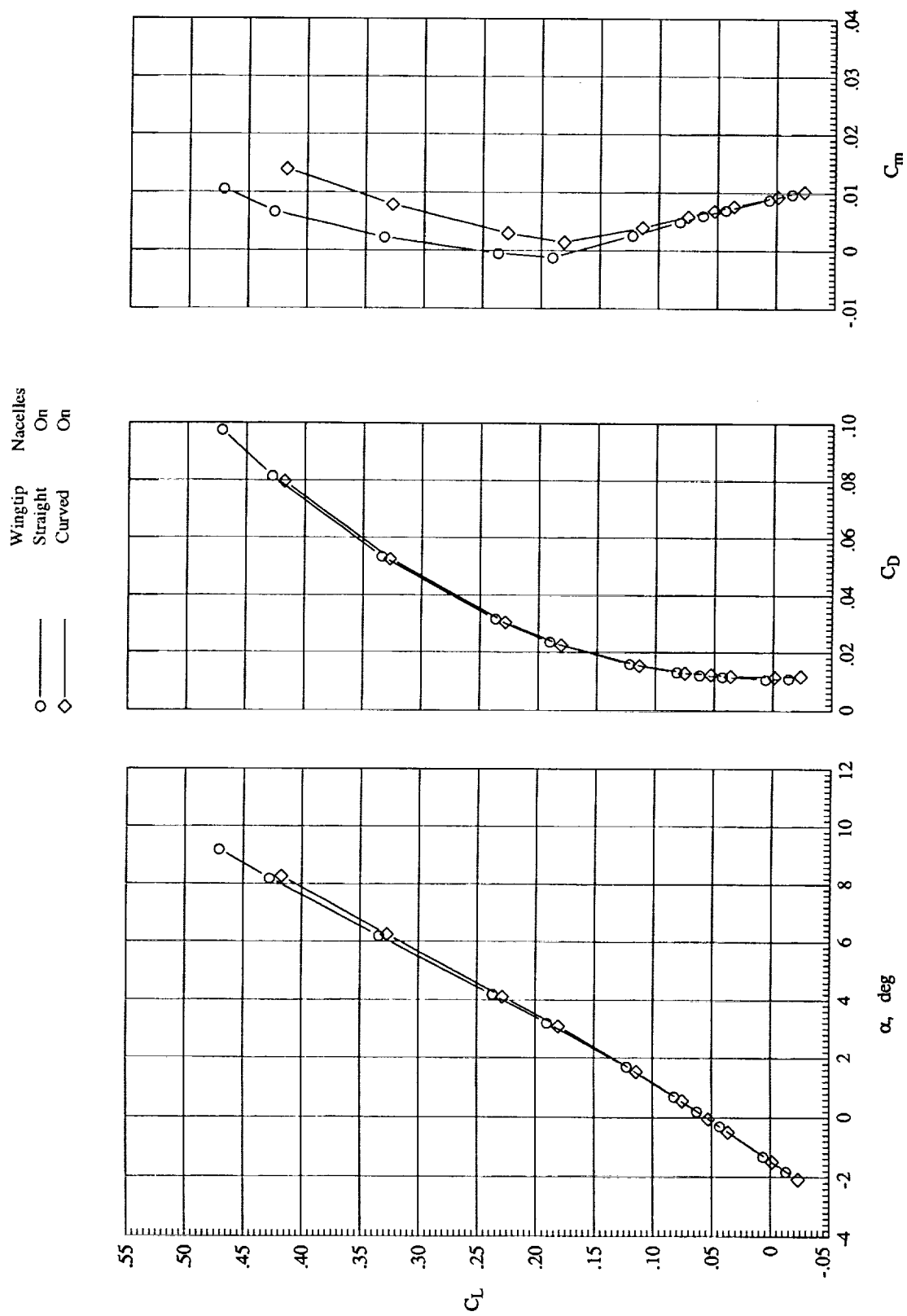
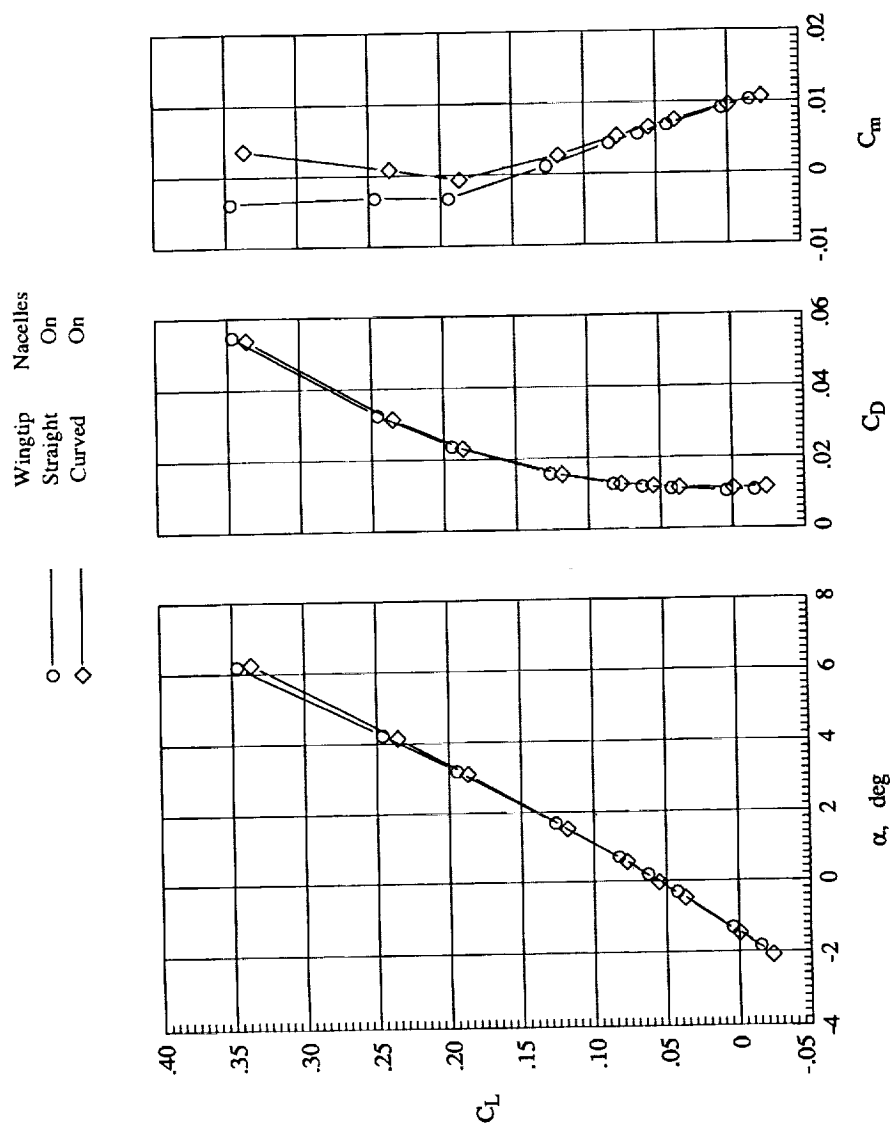
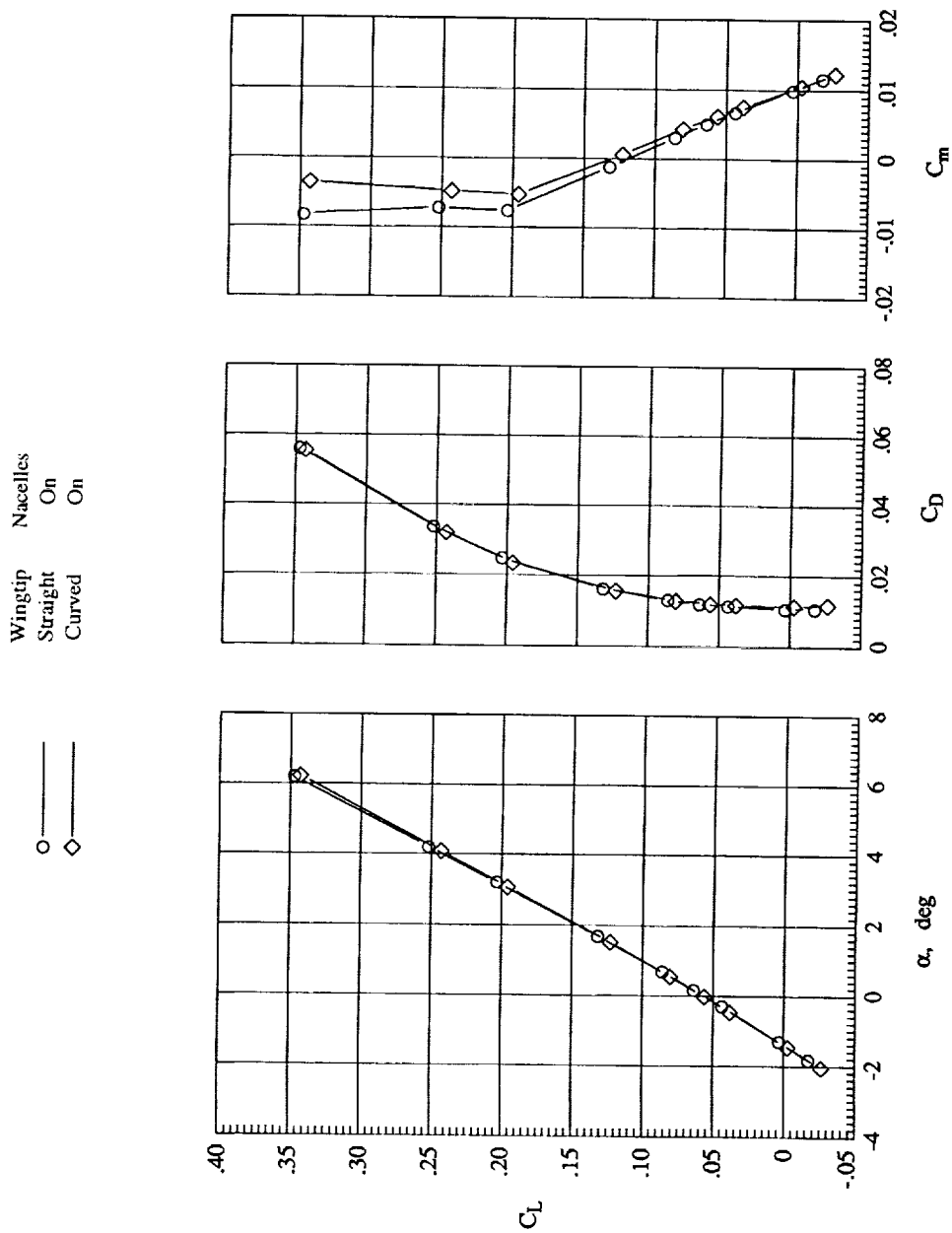
(f) $M_\infty = 0.85$.

Figure 8. Continued.



(g) $M_\infty = 0.90$.

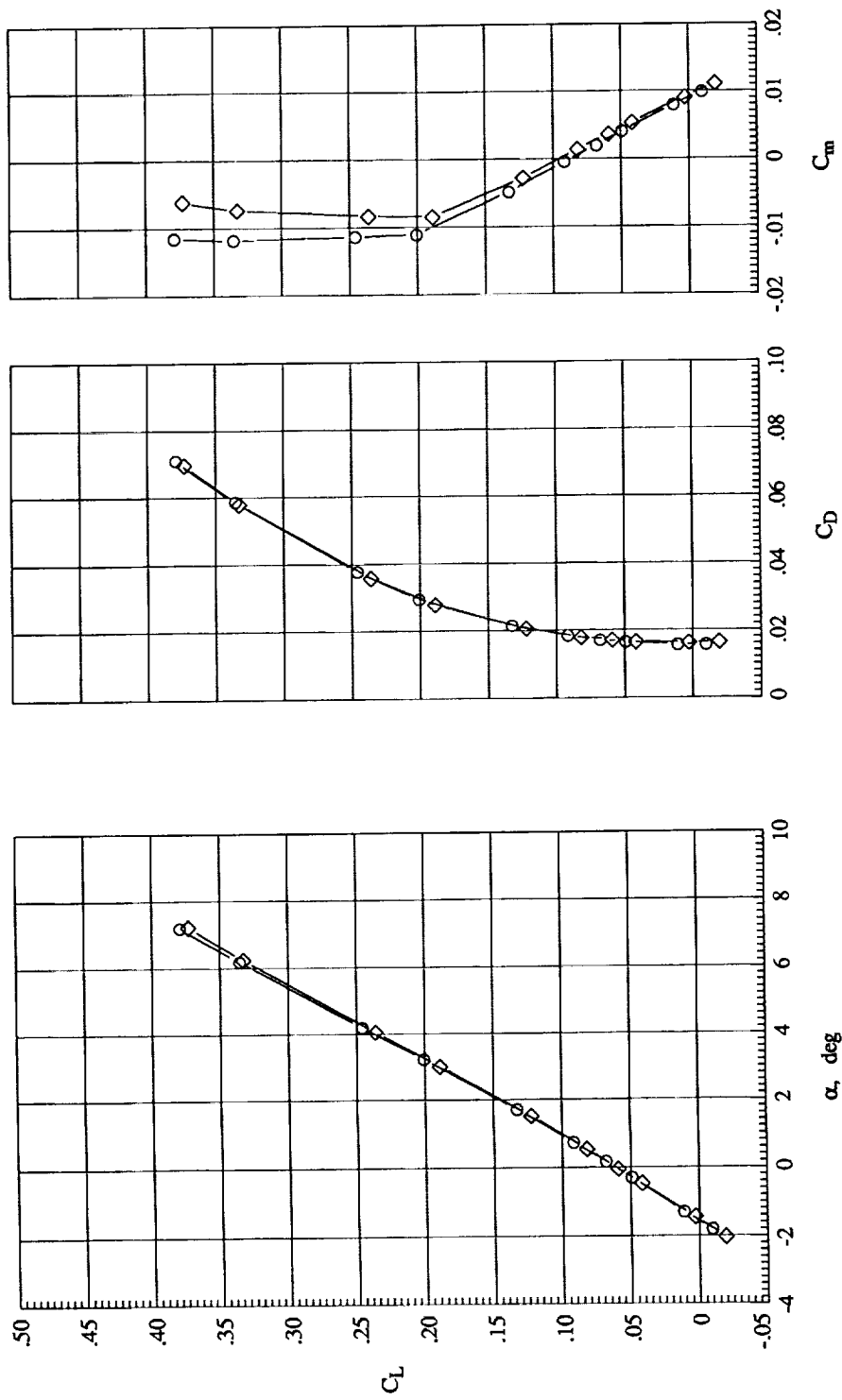
Figure 8. Continued.



(h) $M_\infty = 0.95$.

Figure 8. Continued.

Wingtip Nacelles
 Straight On
 Curved On



(i) $M_{\infty} = 1.10$.

Figure 8. Continued.

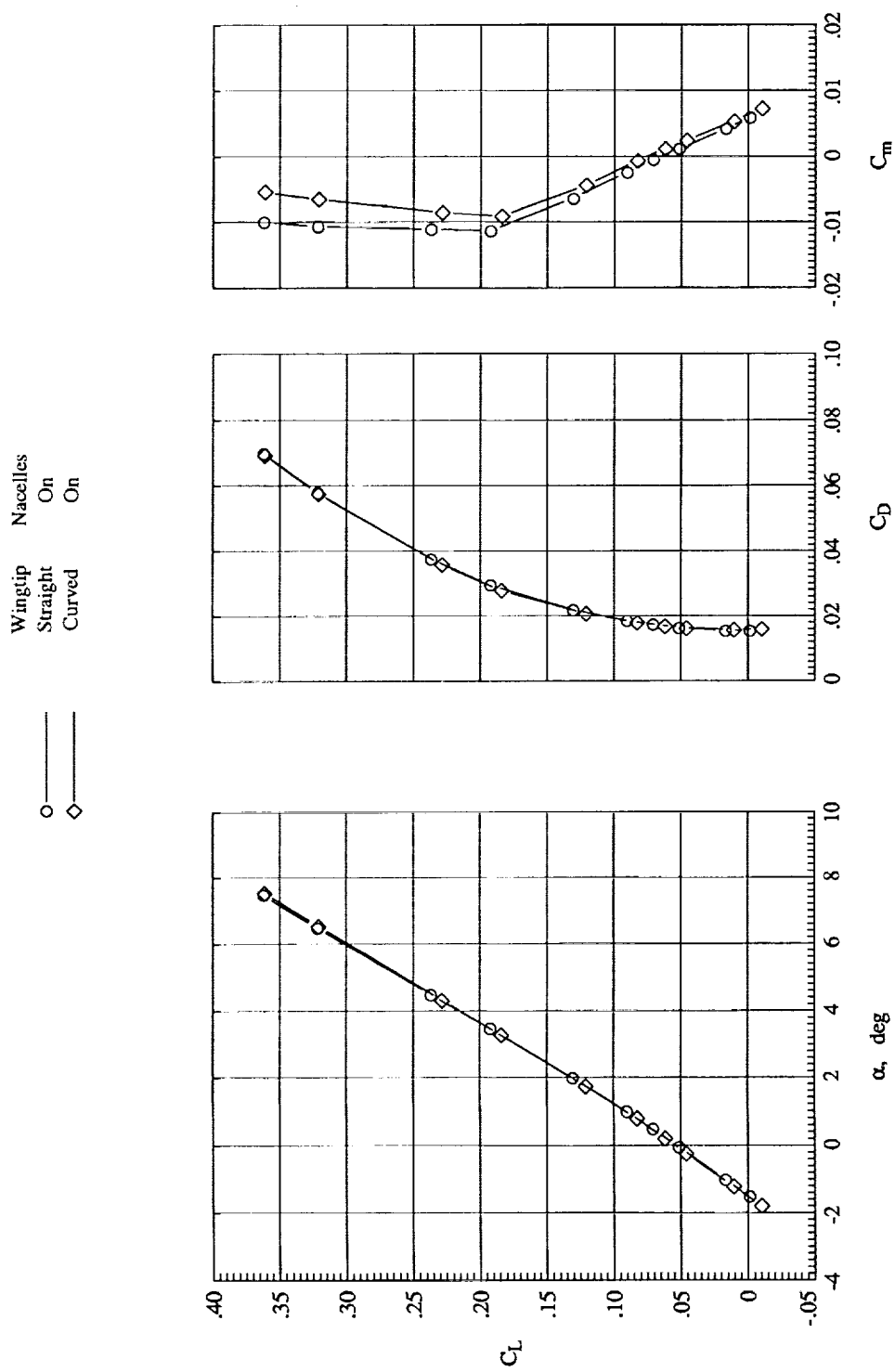
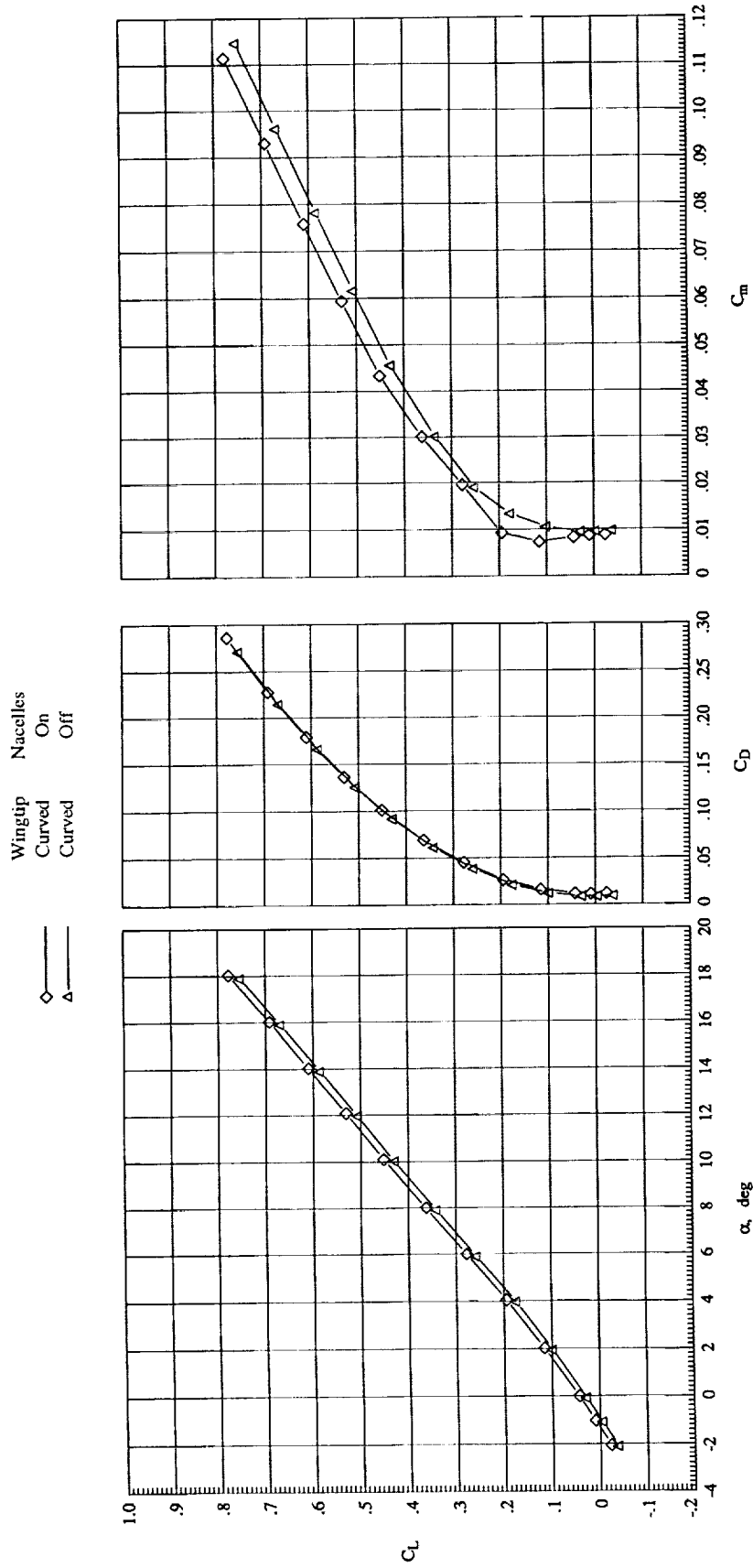
(j) $M_\infty = 1.19$.

Figure 8. Concluded.



(a) $M_\infty = 0.35$.
 Figure 9. Longitudinal characteristics of the curved wingtip model with $\beta = 0^\circ$.

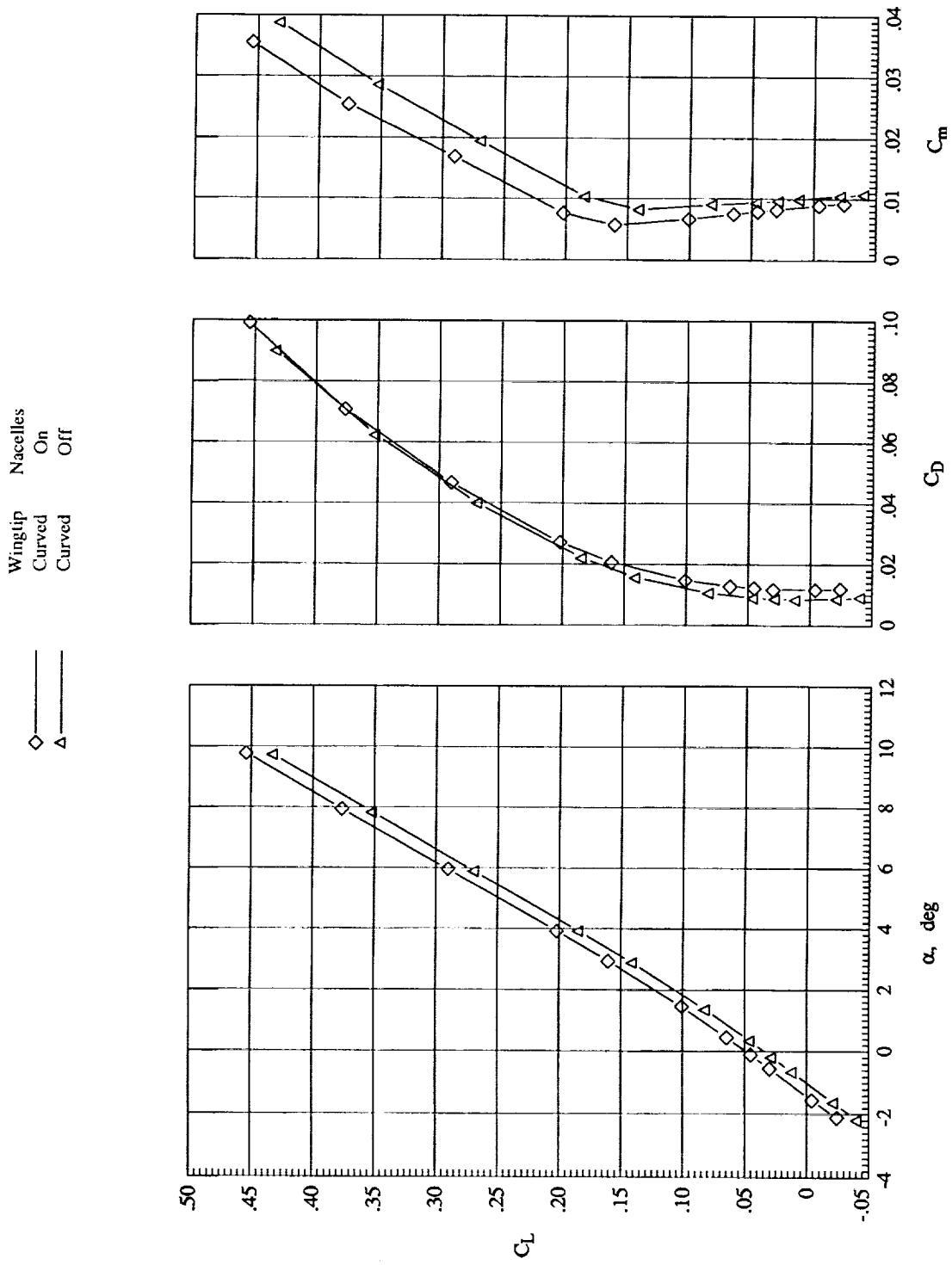
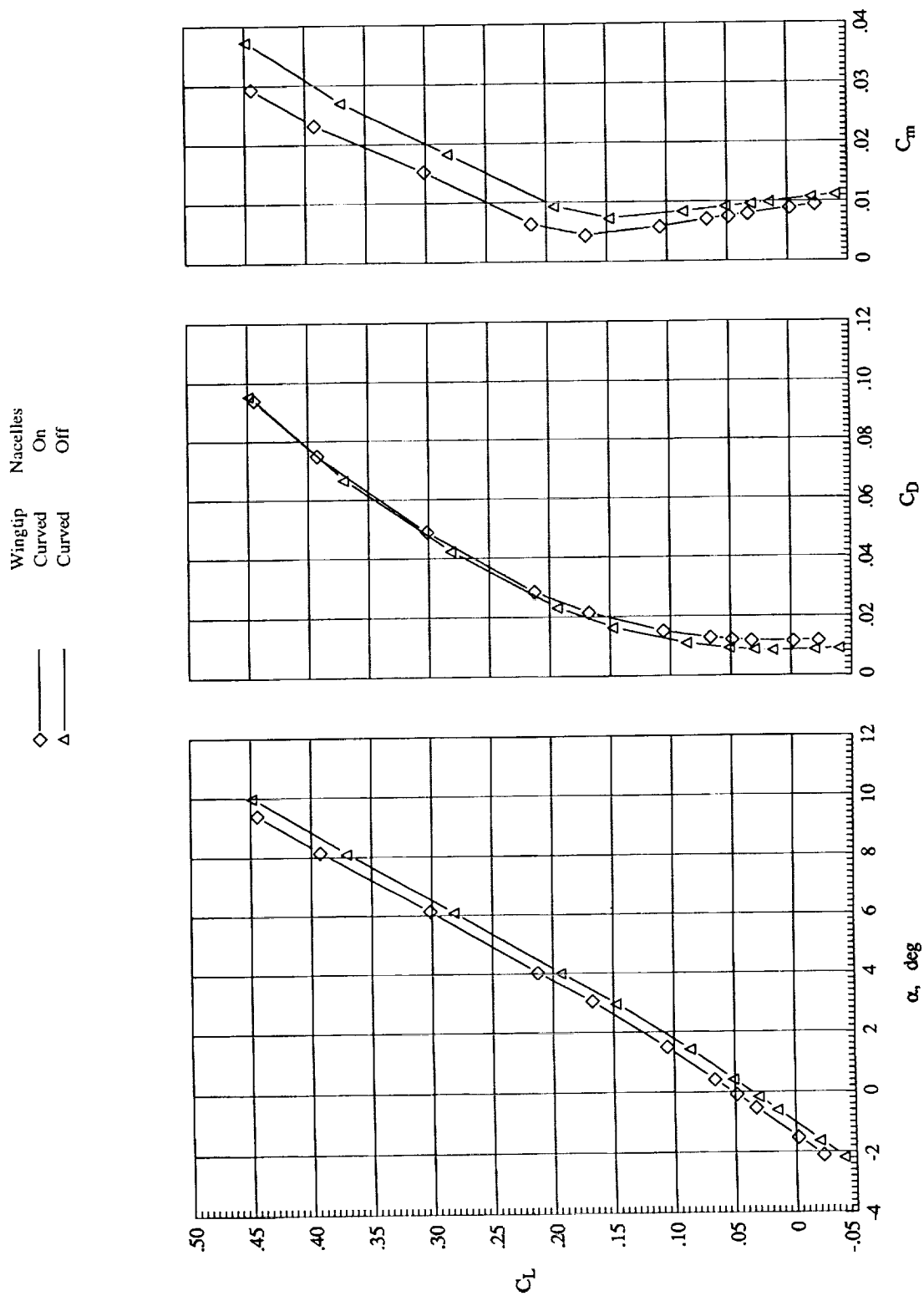
(b) $M_\infty = 0.60$.

Figure 9. Continued.

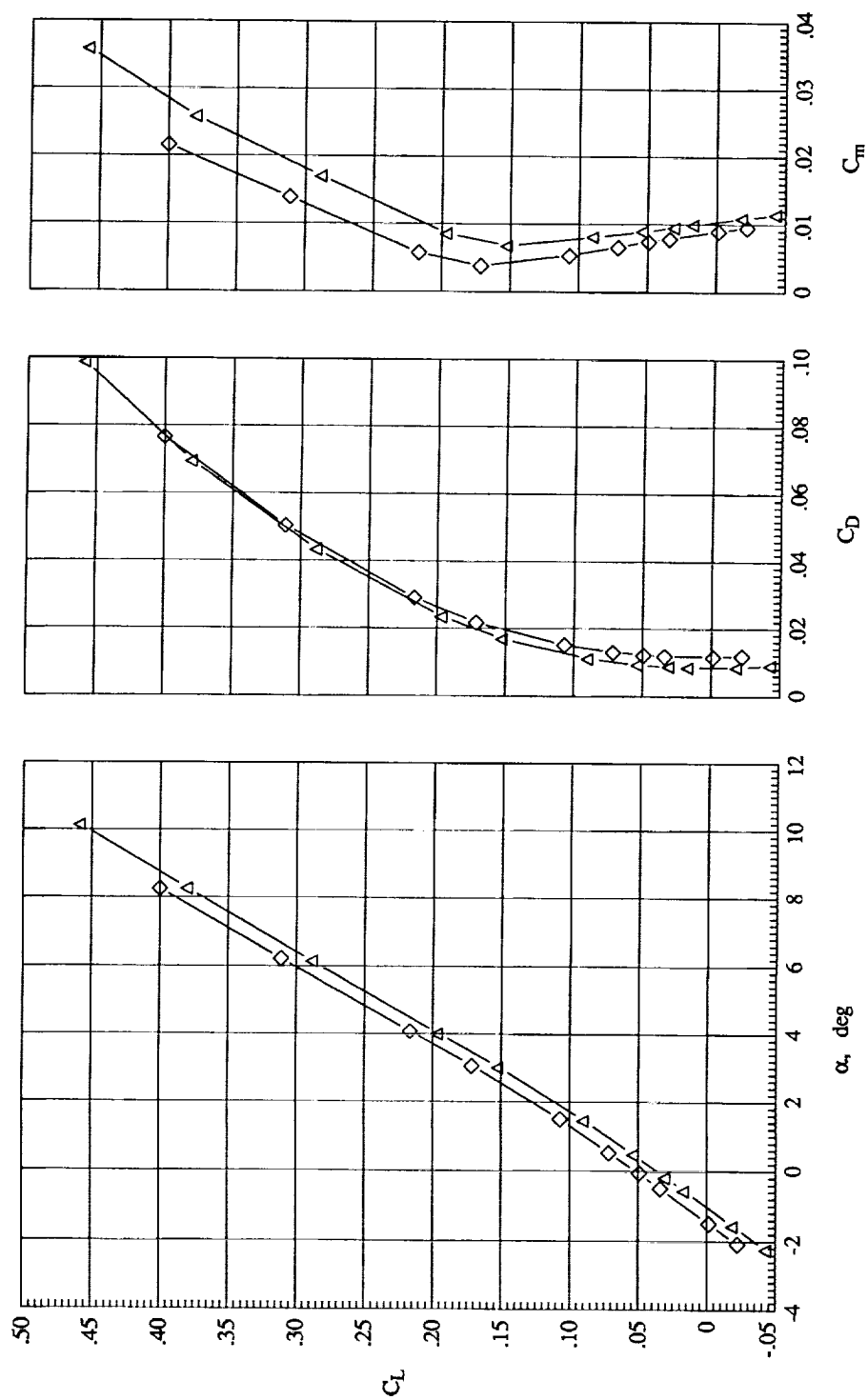


(c) $M_\infty = 0.70$.

Figure 9. Continued.

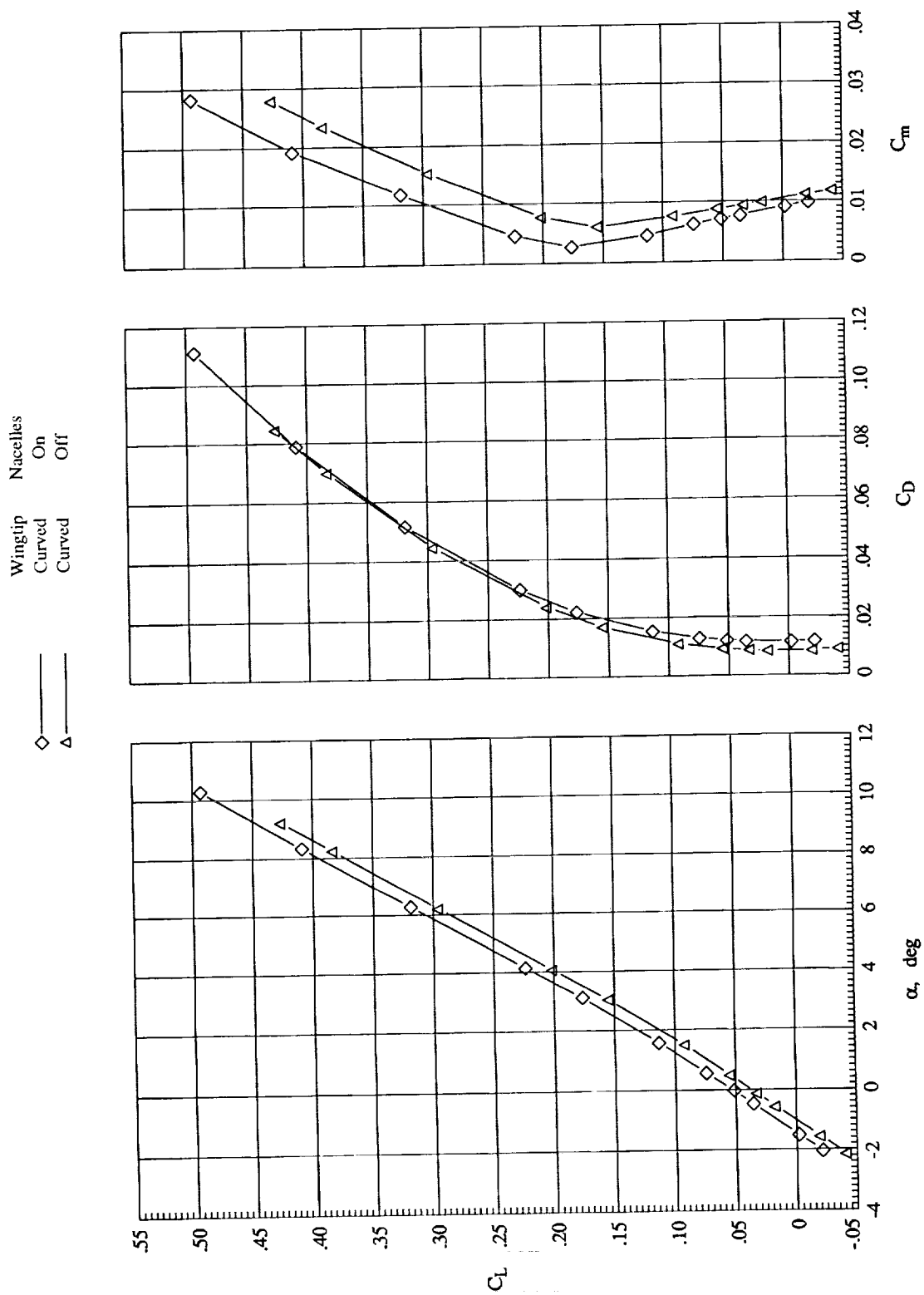
Wingtip Nacelles
Curved On
Curved Off

◇
△



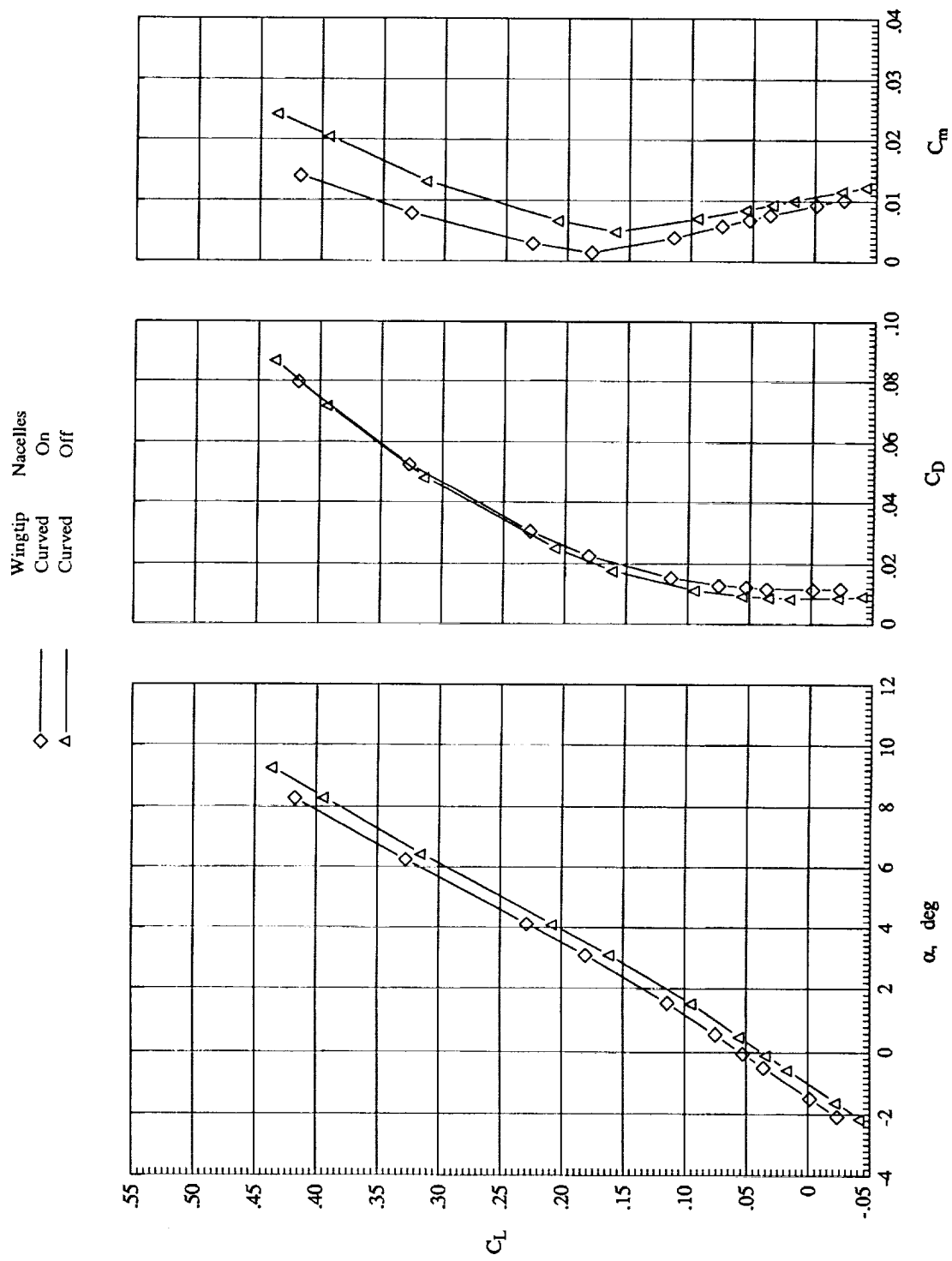
(d) $M_\infty = 0.75$.

Figure 9. Continued.



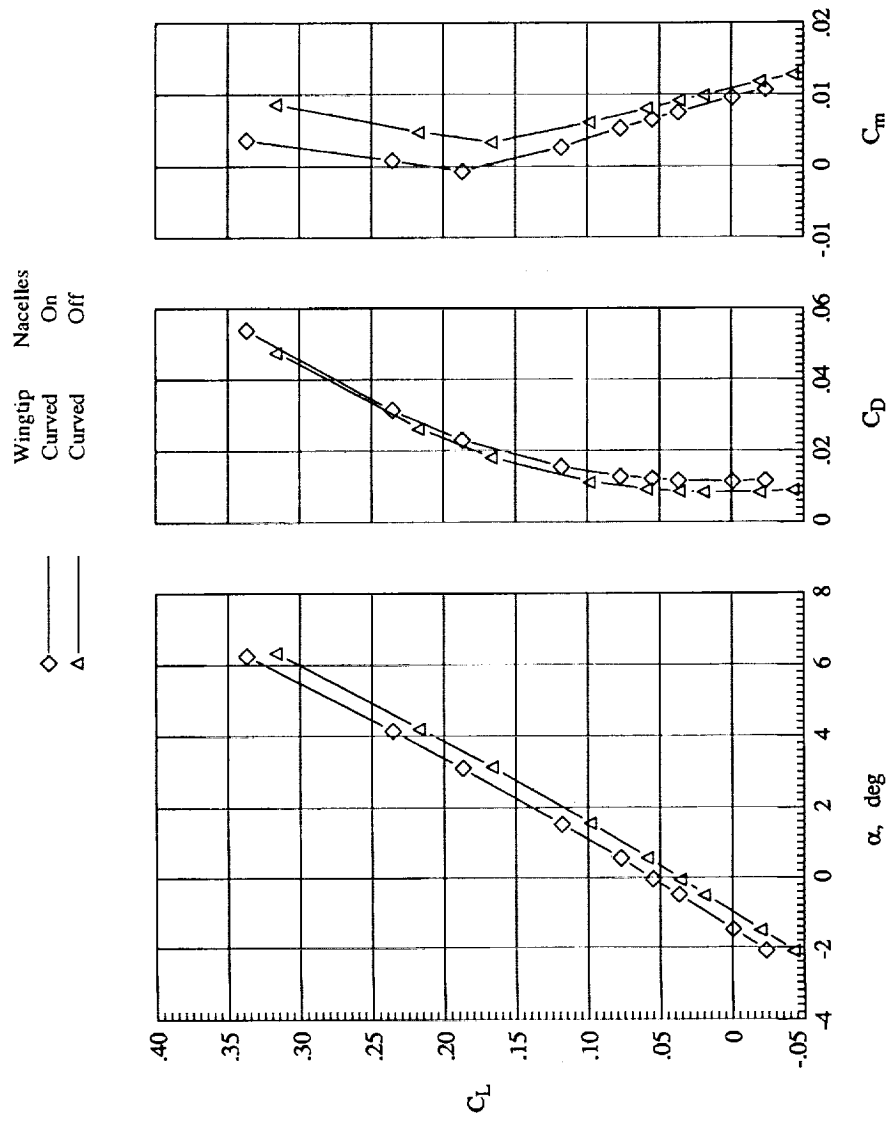
(e) $M_\infty = 0.80$.

Figure 9. Continued.



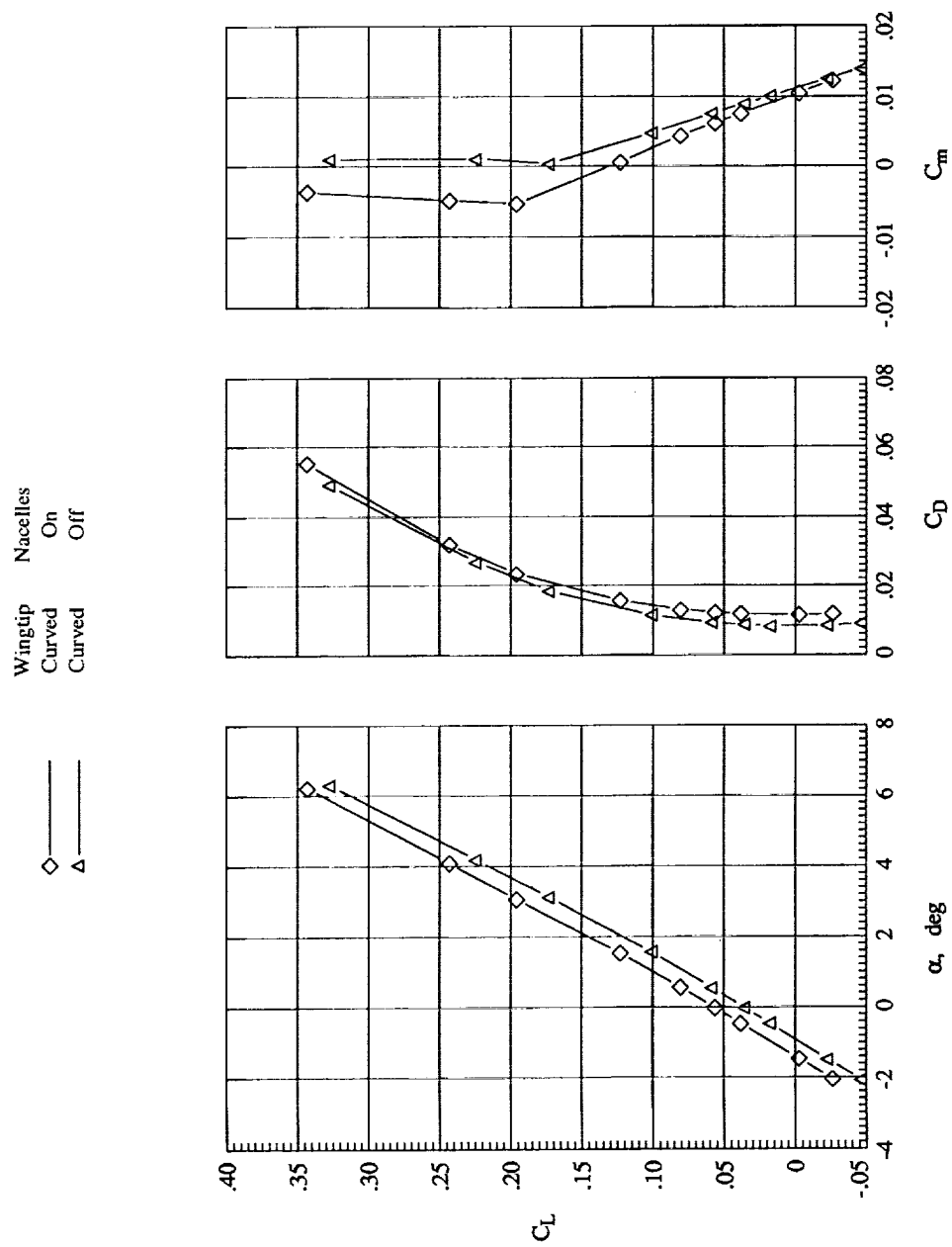
(f) $M_\infty = 0.85$.

Figure 9. Continued.



(g) $M_\infty = 0.90$.

Figure 9. Continued.

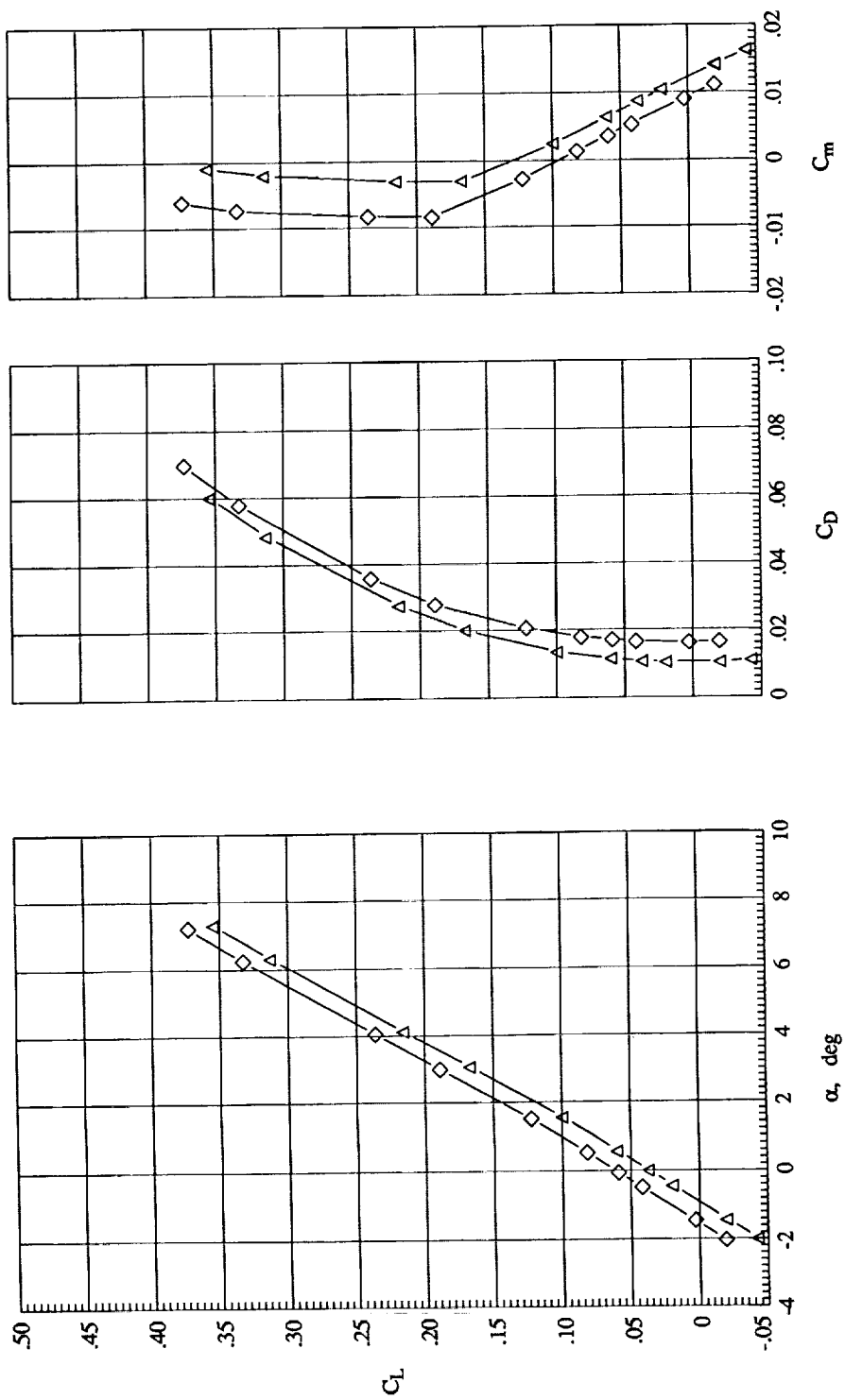


(h) $M_\infty = 0.95$.

Figure 9. Continued.

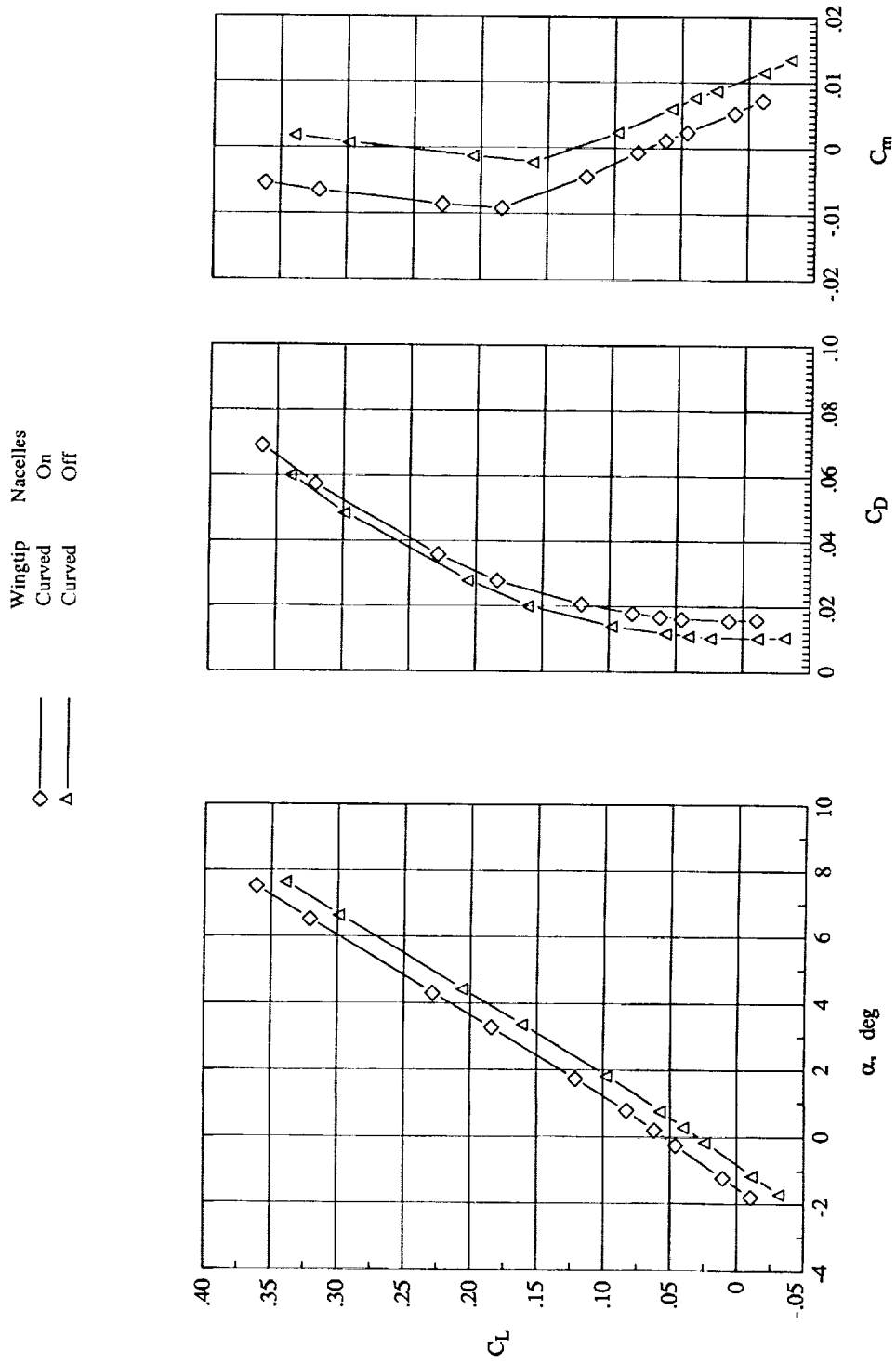
Wingtip Nacelles
 Curved On
 Curved Off

◇
 △



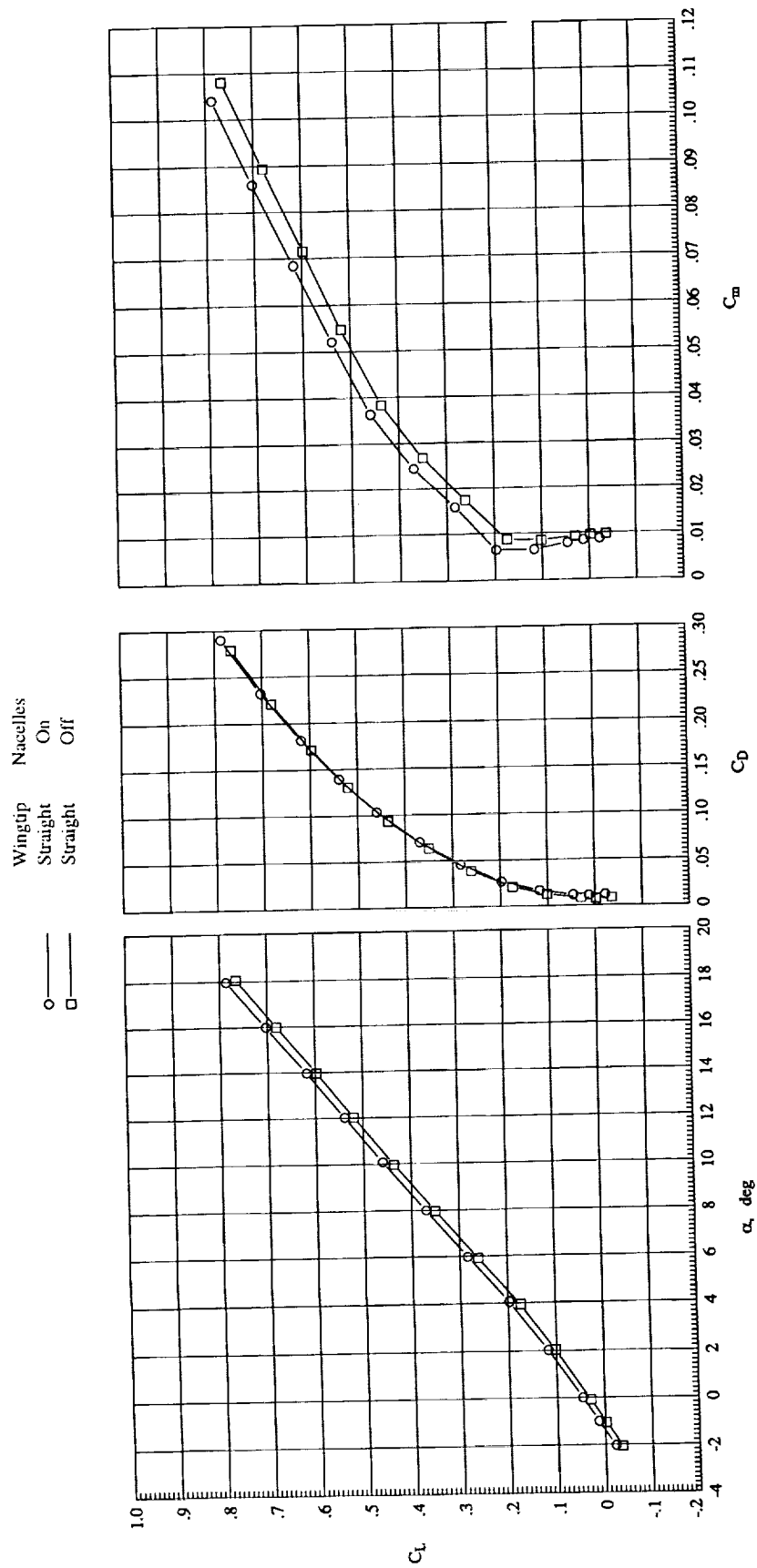
(i) $M_{\infty} = 1.10$.

Figure 9. Continued.



(j) $M_\infty = 1.19$.

Figure 9. Concluded.

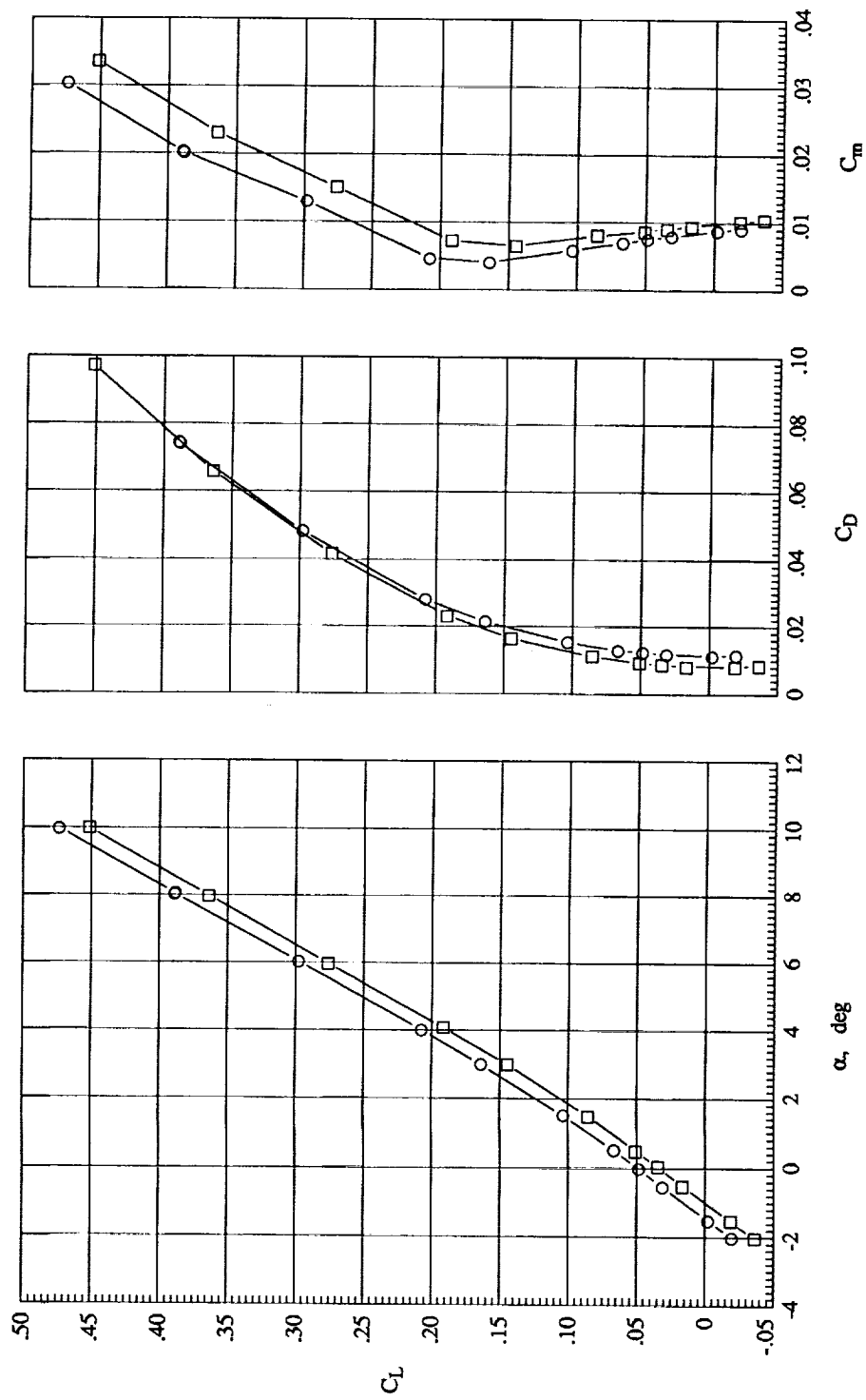


(a) $M_{\infty} = 0.30$.
 Figure 10. Longitudinal characteristics of the straight wingtip models with $\beta = 0^\circ$.

Wingtip
Straight
Straight

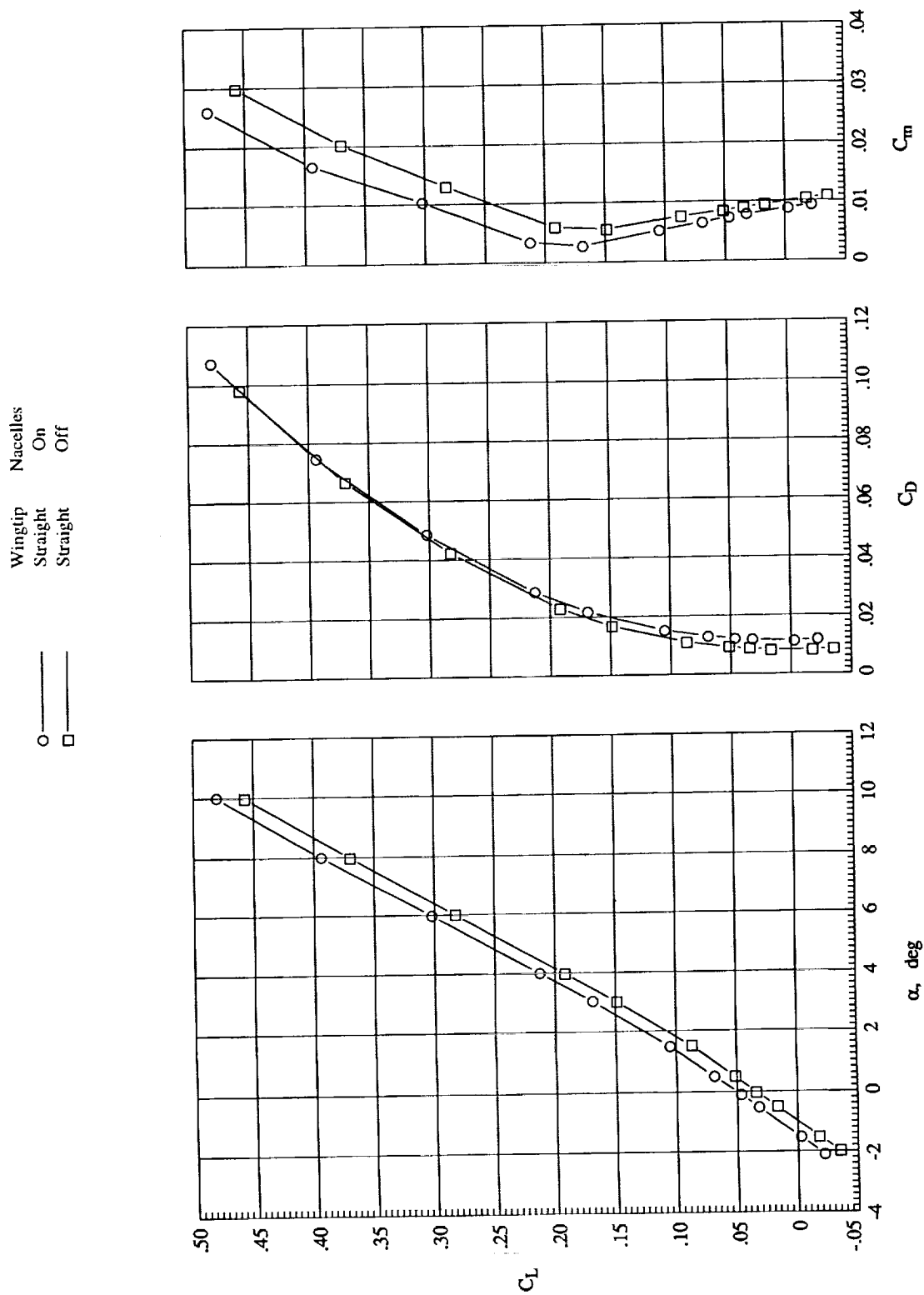
Nacelles
On
Off

○ □



(b) $M_\infty = 0.60$.

Figure 10. Continued.

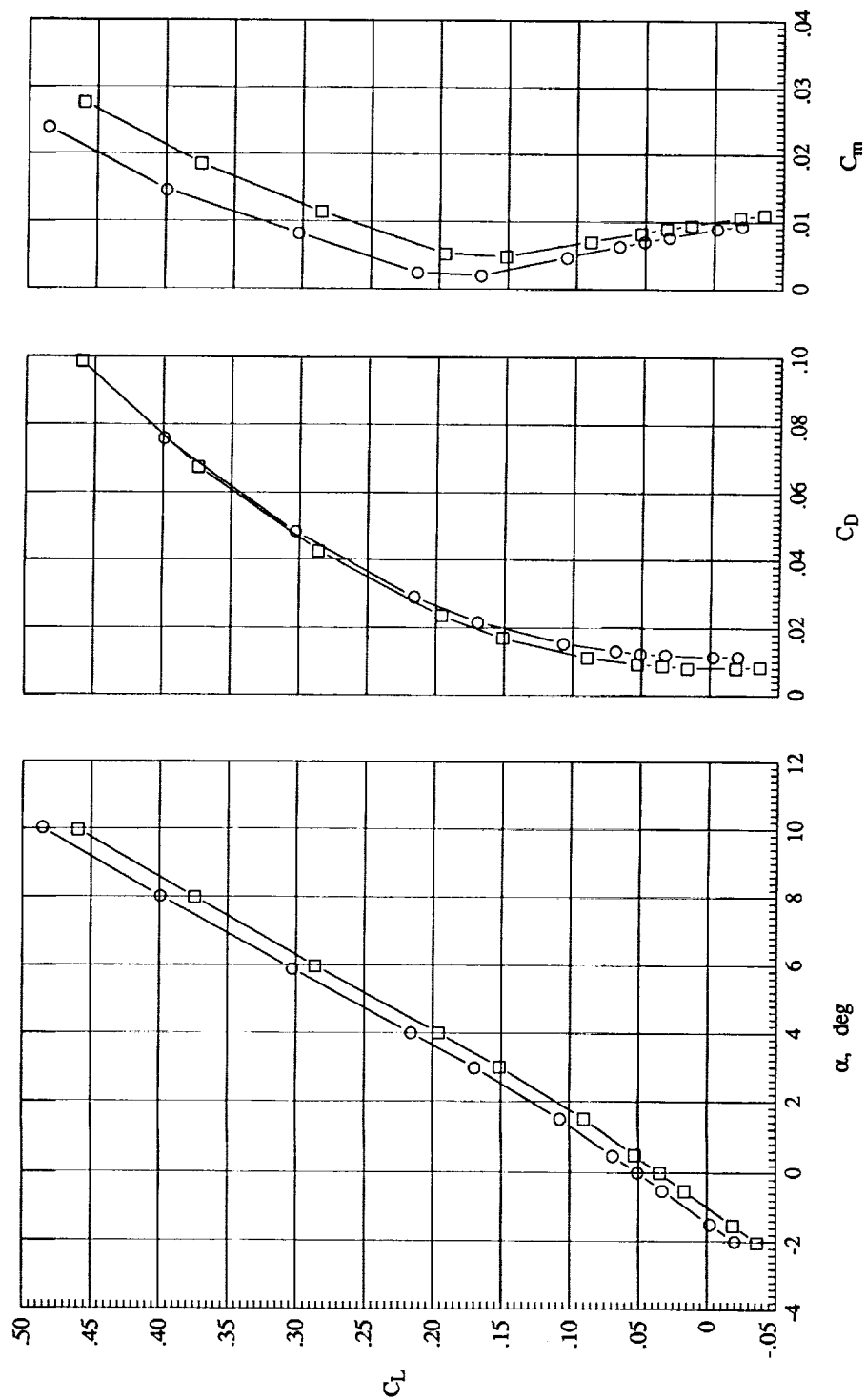


(c) $M_\infty = 0.70$.

Figure 10. Continued.

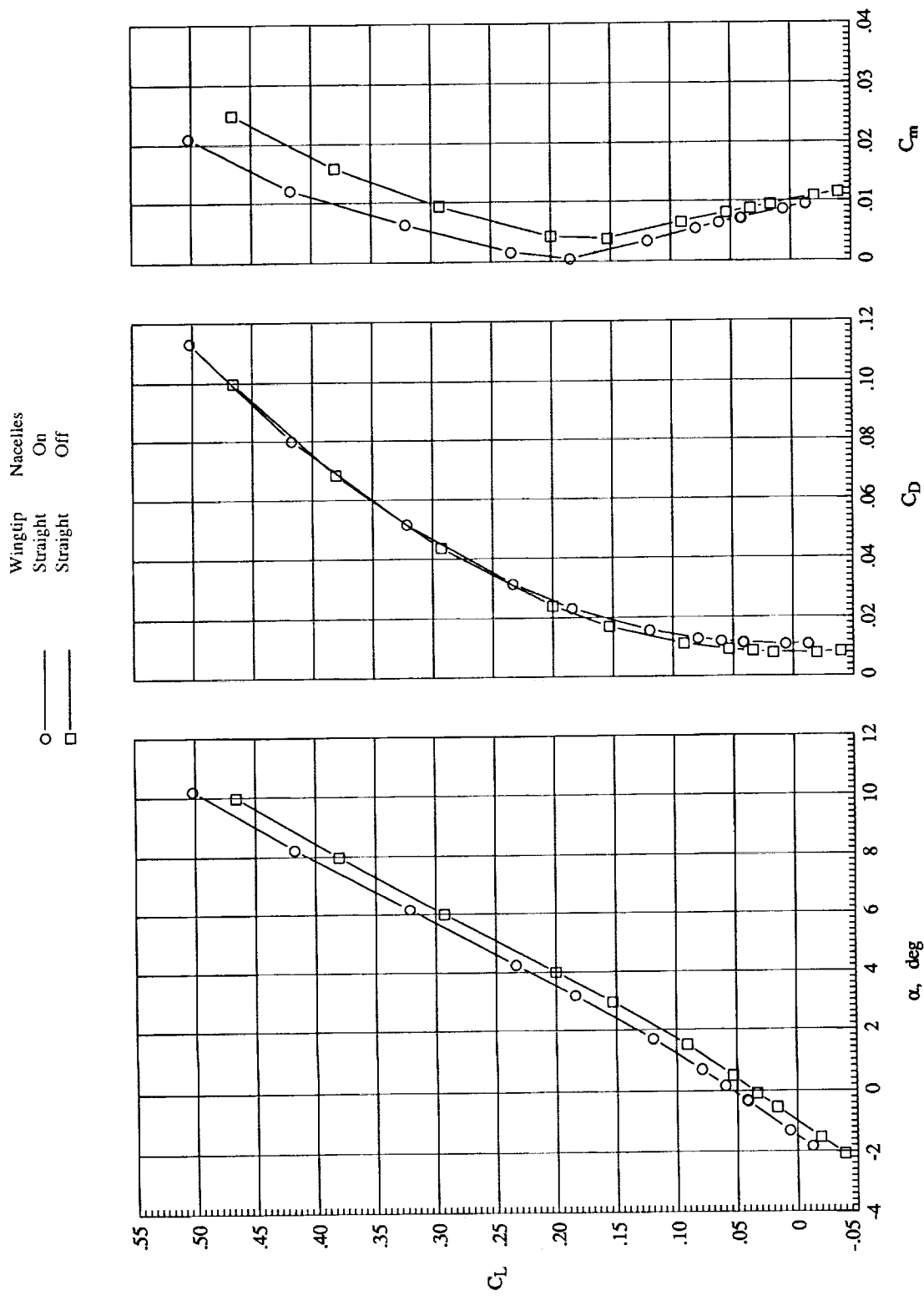
Wingtip Nacelles
Straight On
Straight Off

○ □



(d) $M_\infty = 0.75$.

Figure 10. Continued.



(e) $M_\infty = 0.80$.

Figure 10. Continued.

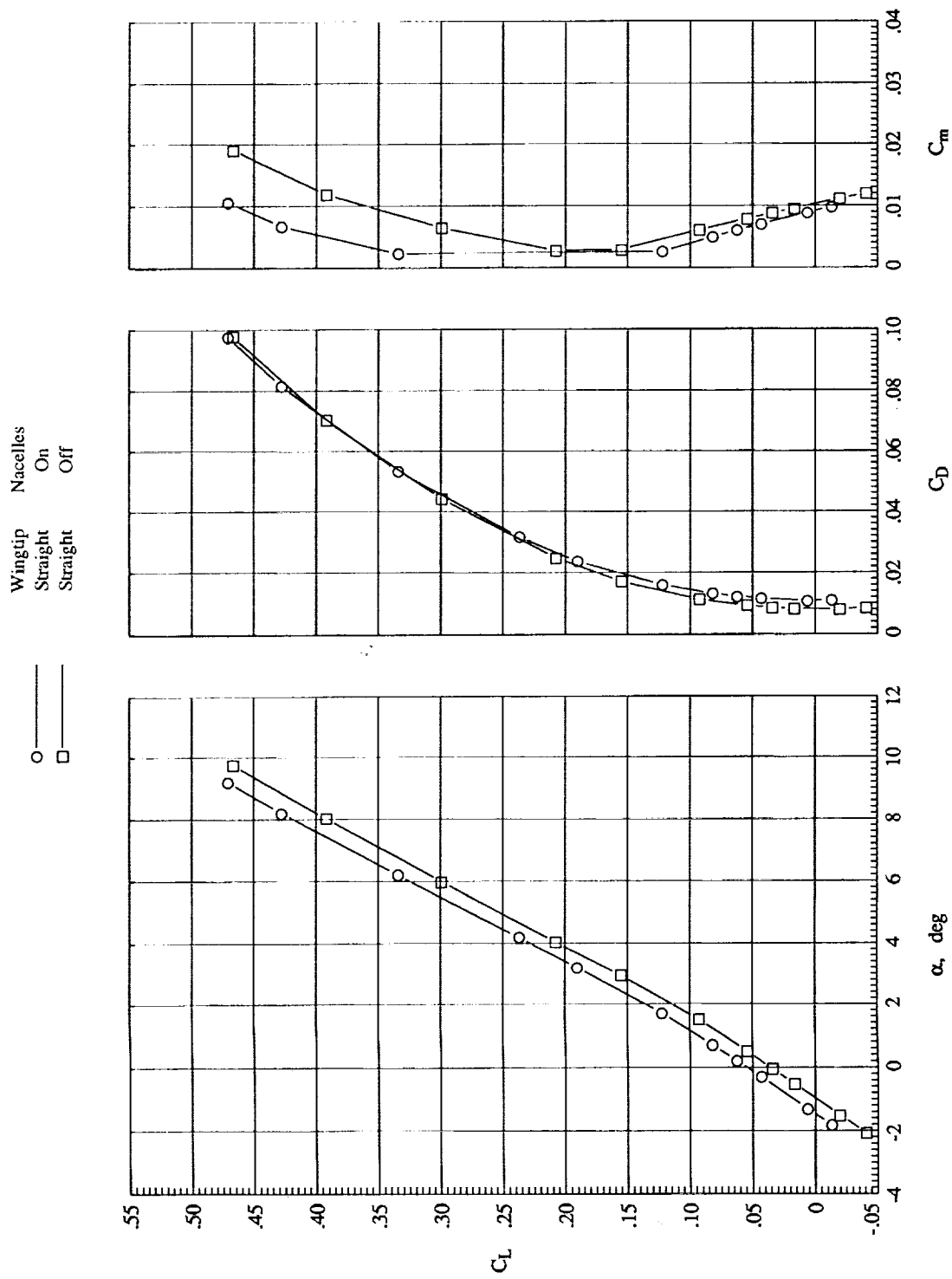
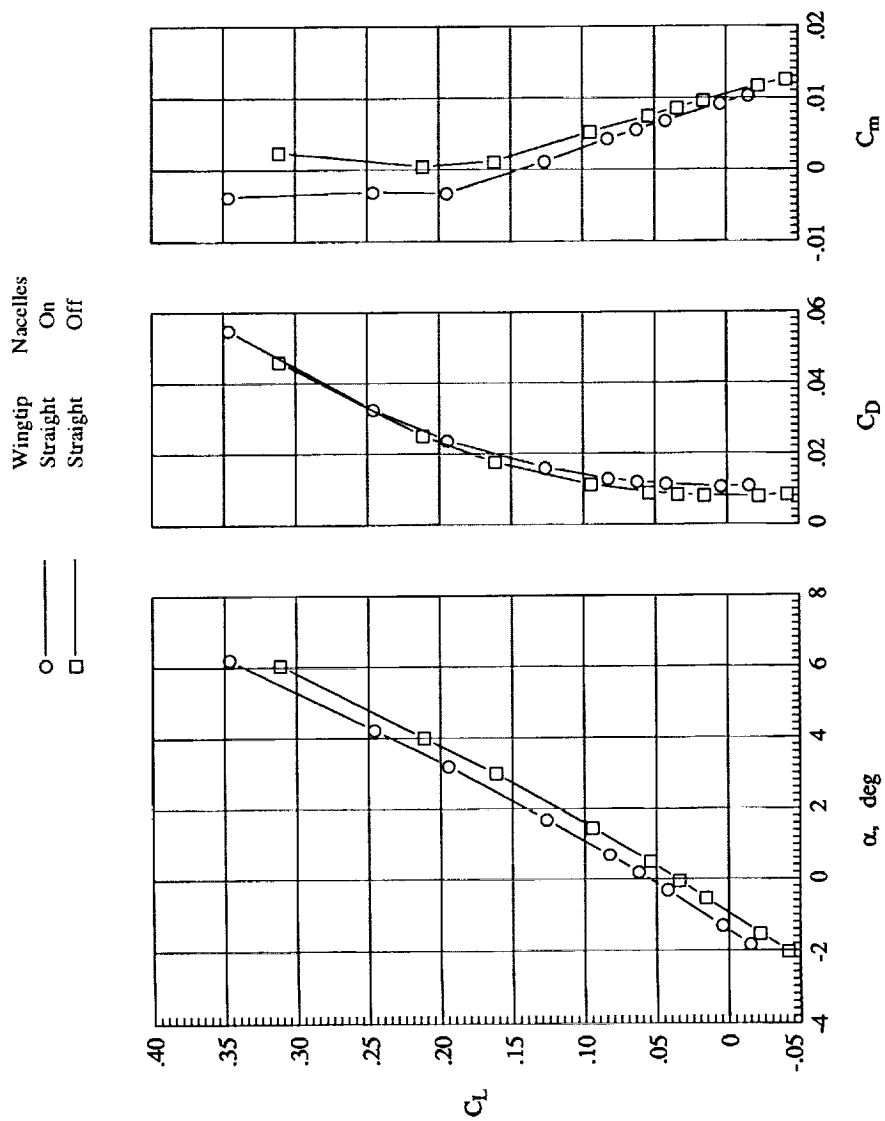
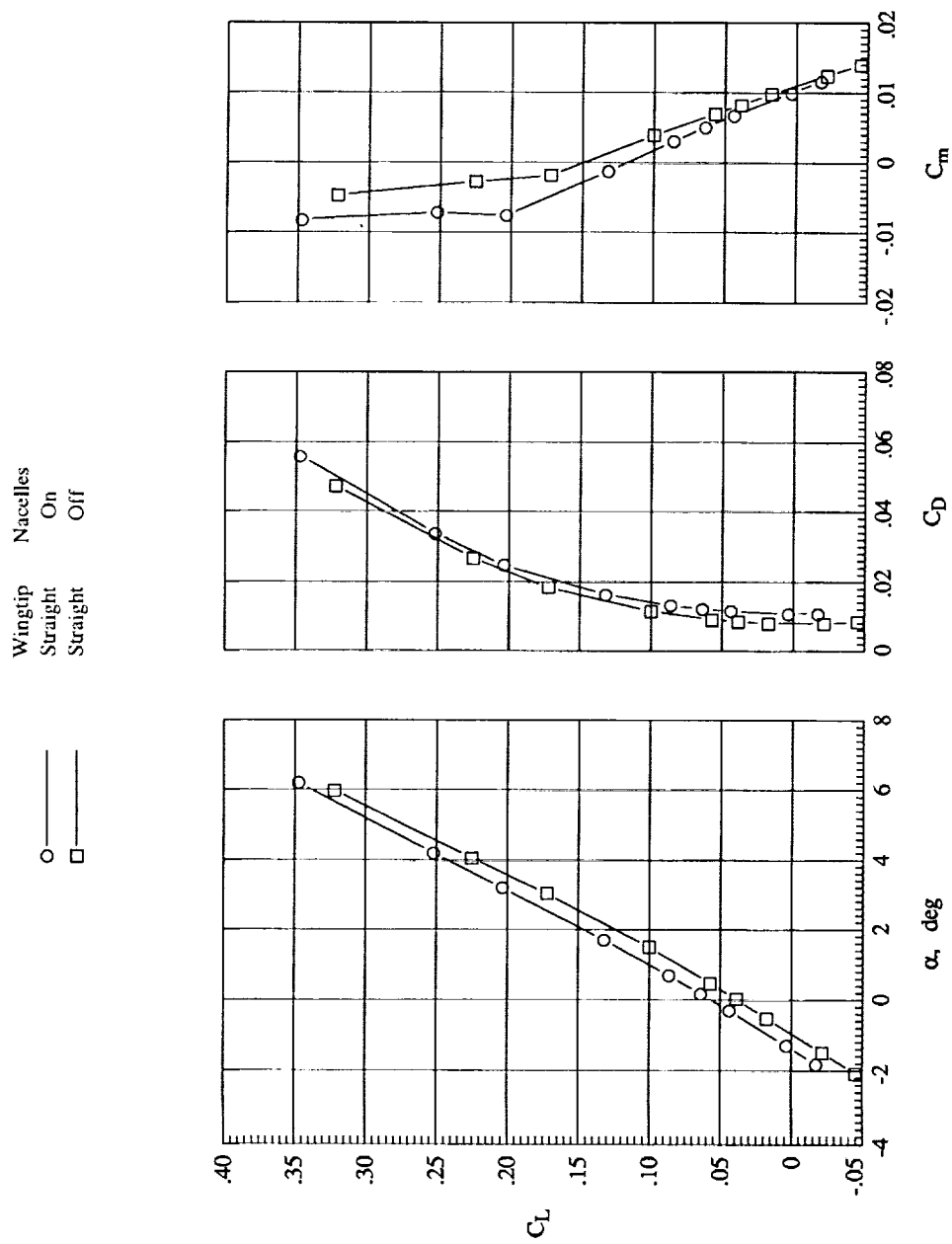
(f) $M_\infty = 0.85$.

Figure 10. Continued.



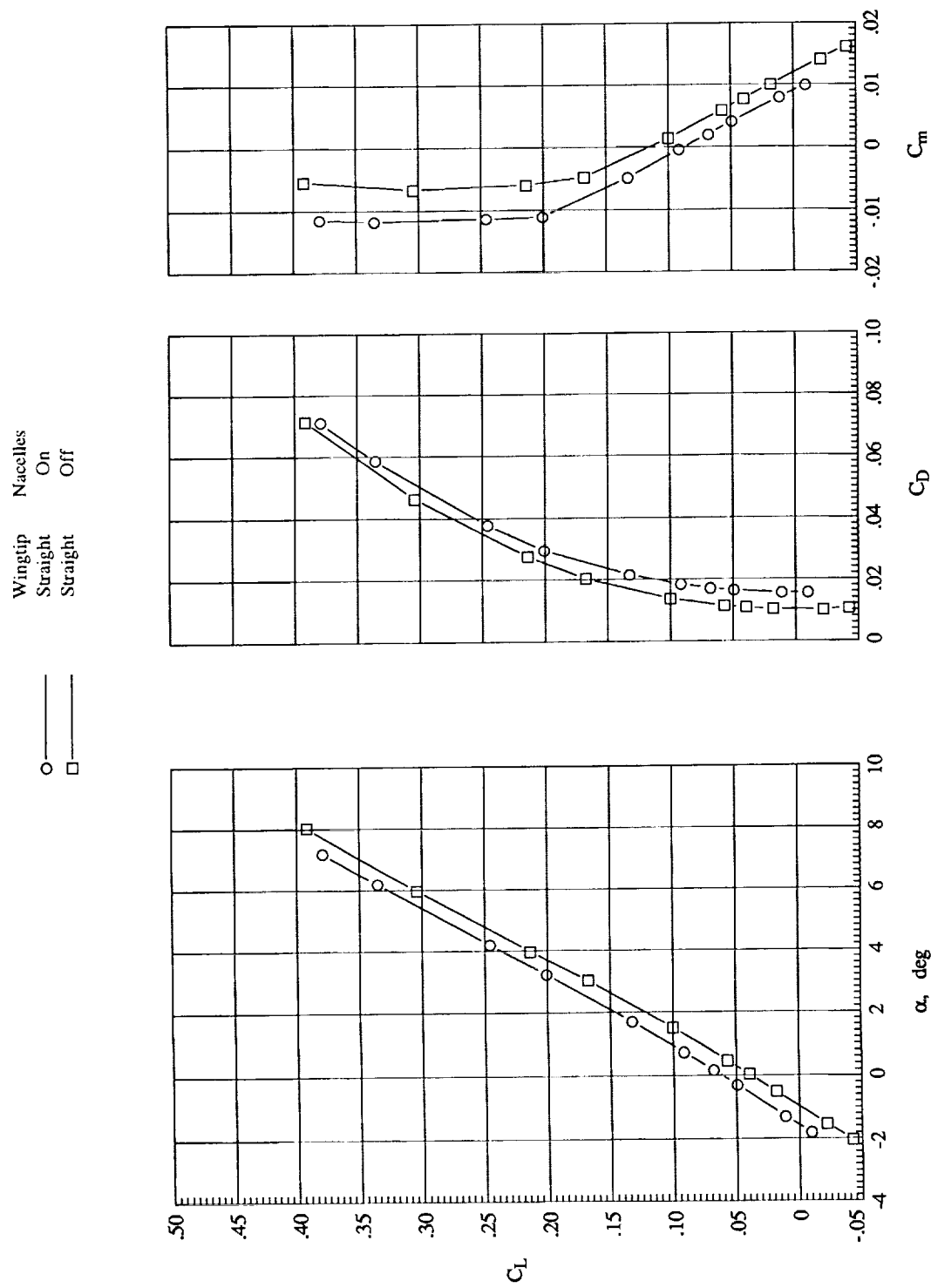
(g) $M_\infty = 0.90$.

Figure 10. Continued.



(h) $M_\infty = 0.95$.

Figure 10. Continued.

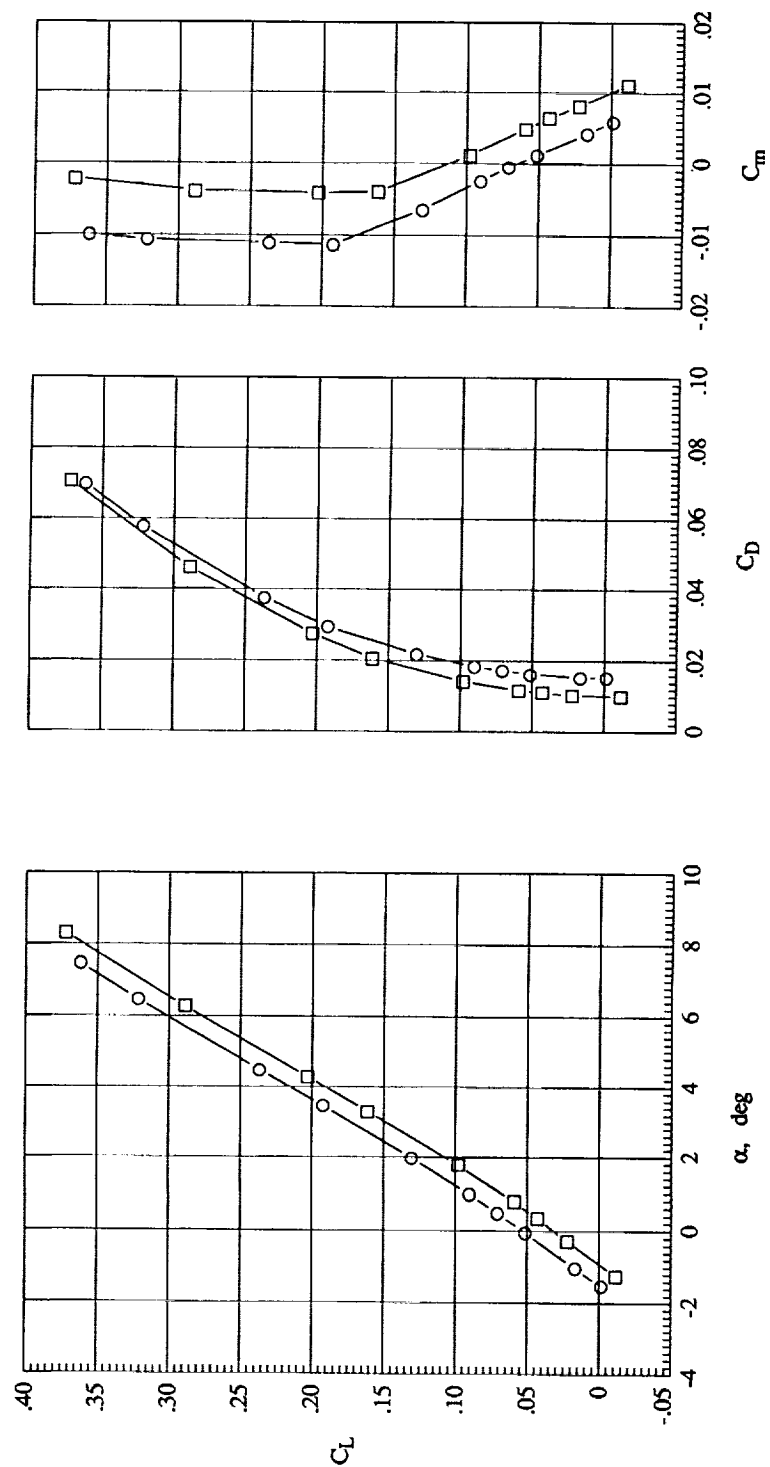


(i) $M_{\infty} = 1.10$.

Figure 10. Continued.

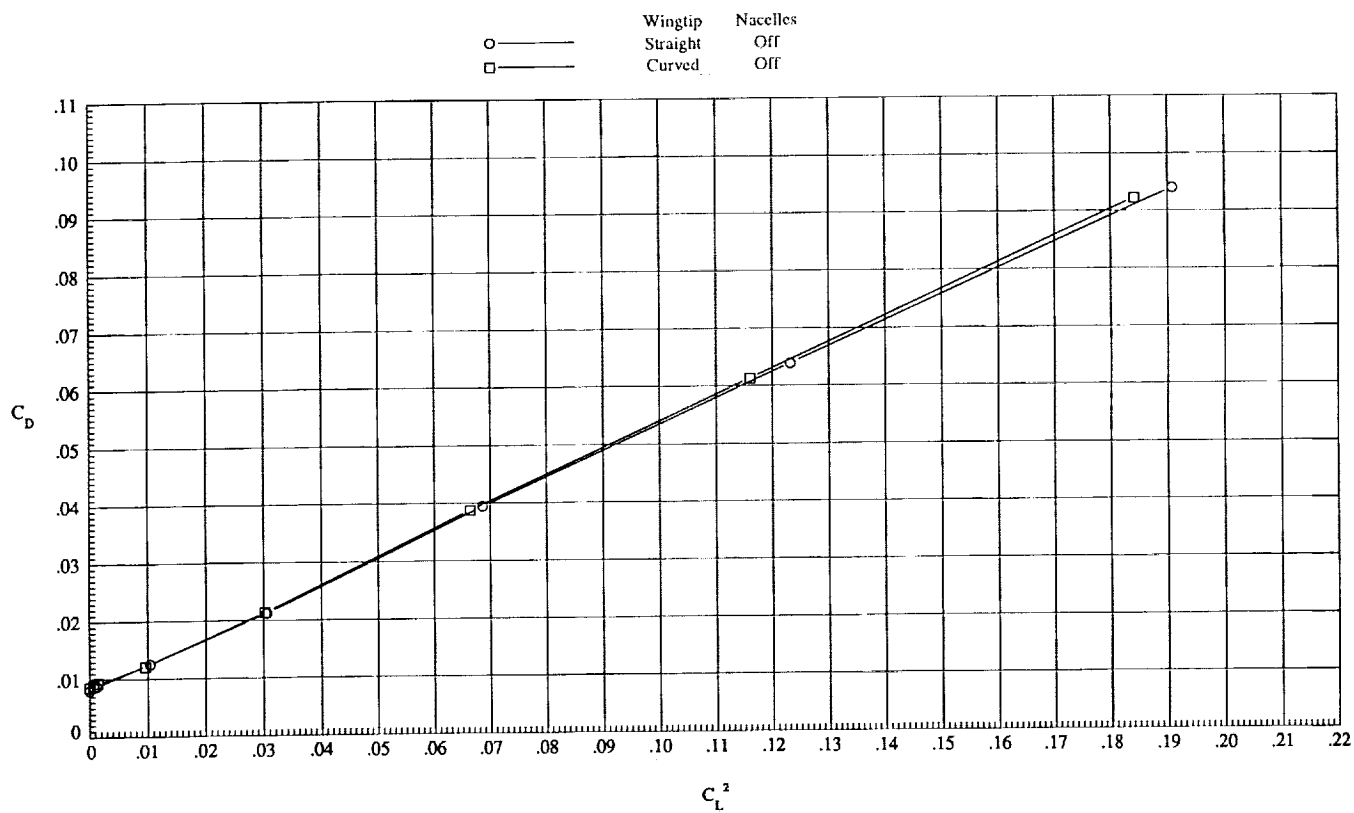
Wingtip Nacelles
 Straight On
 Straight Off

○
 □



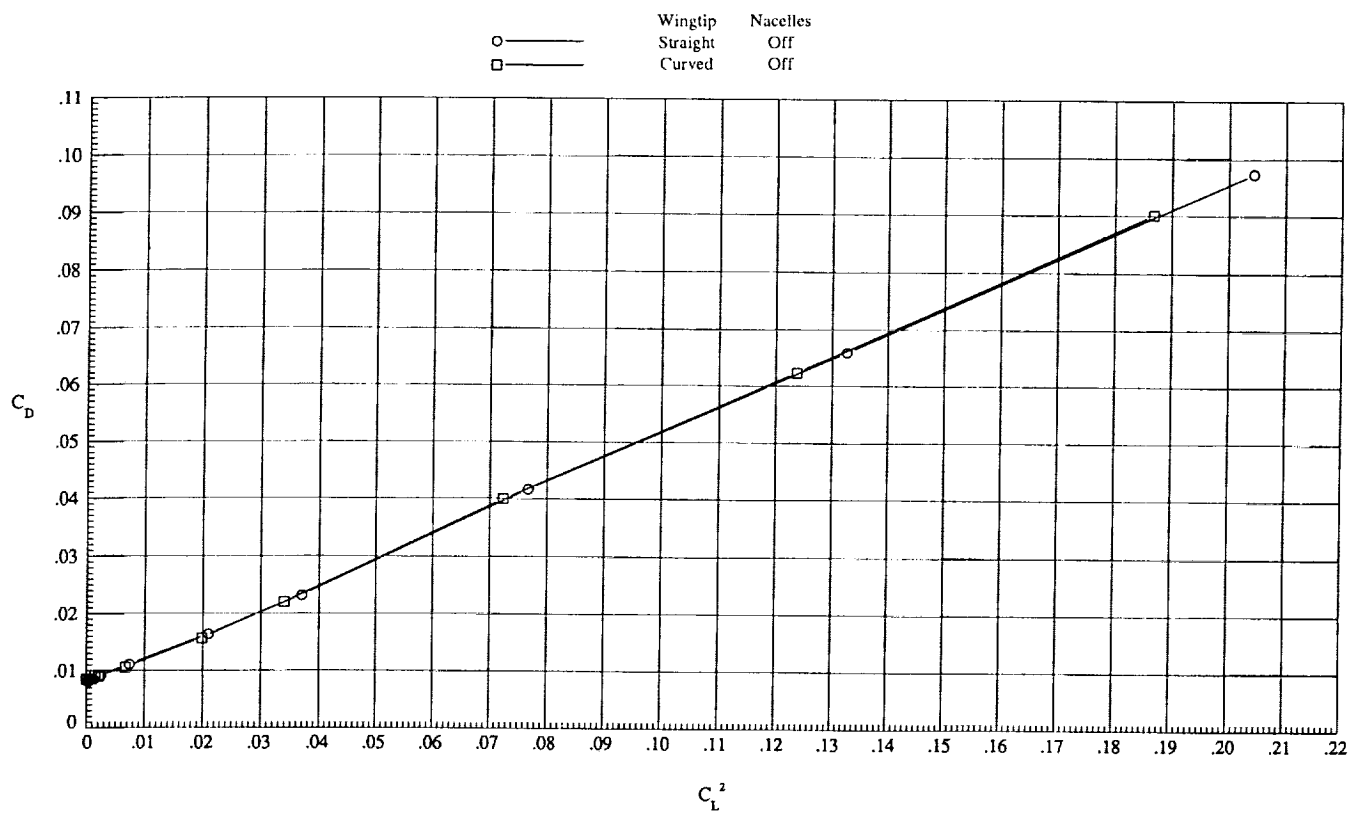
(j) $M_\infty = 1.19$.

Figure 10. Concluded.



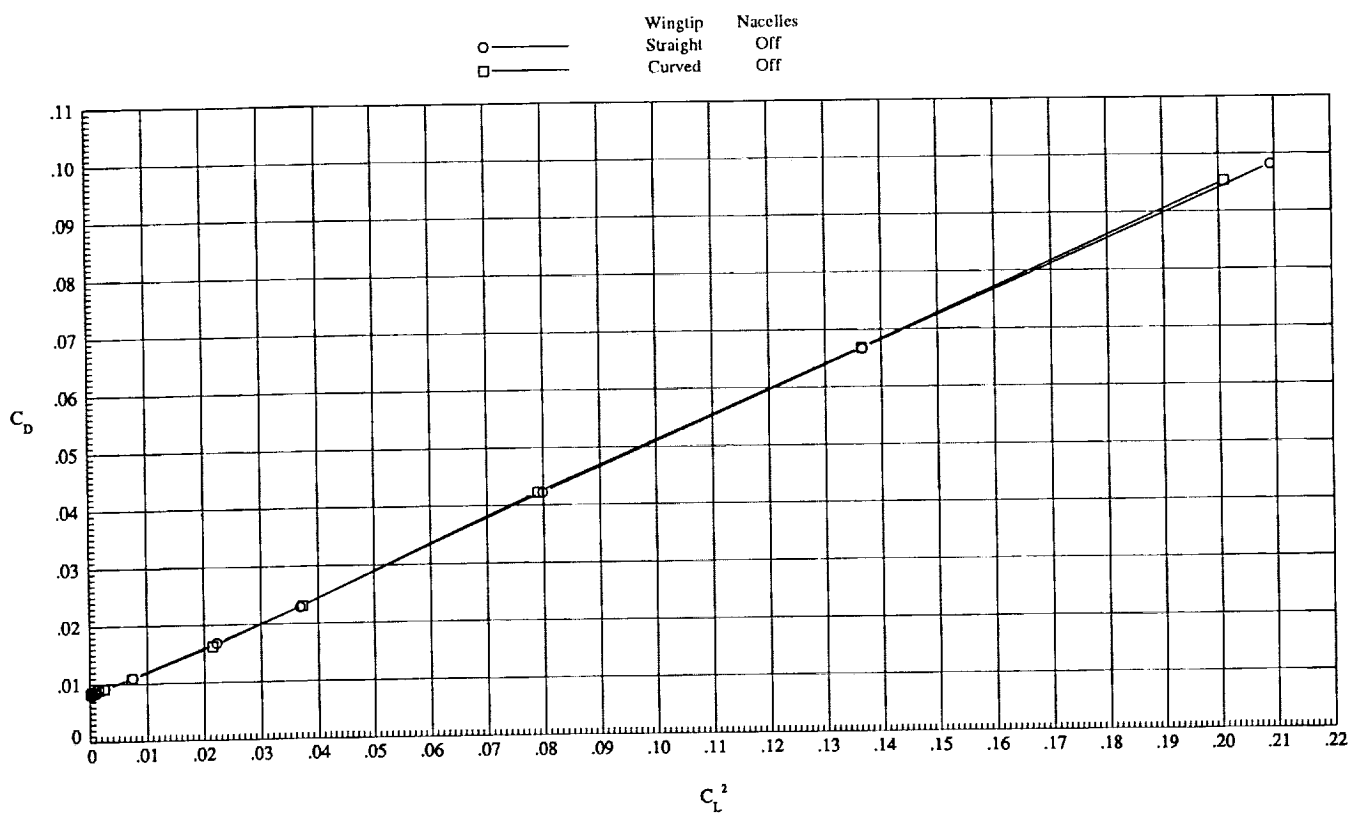
(a) $M_\infty = 0.30$.

Figure 11. Induced drag characteristics. Nacelles off.



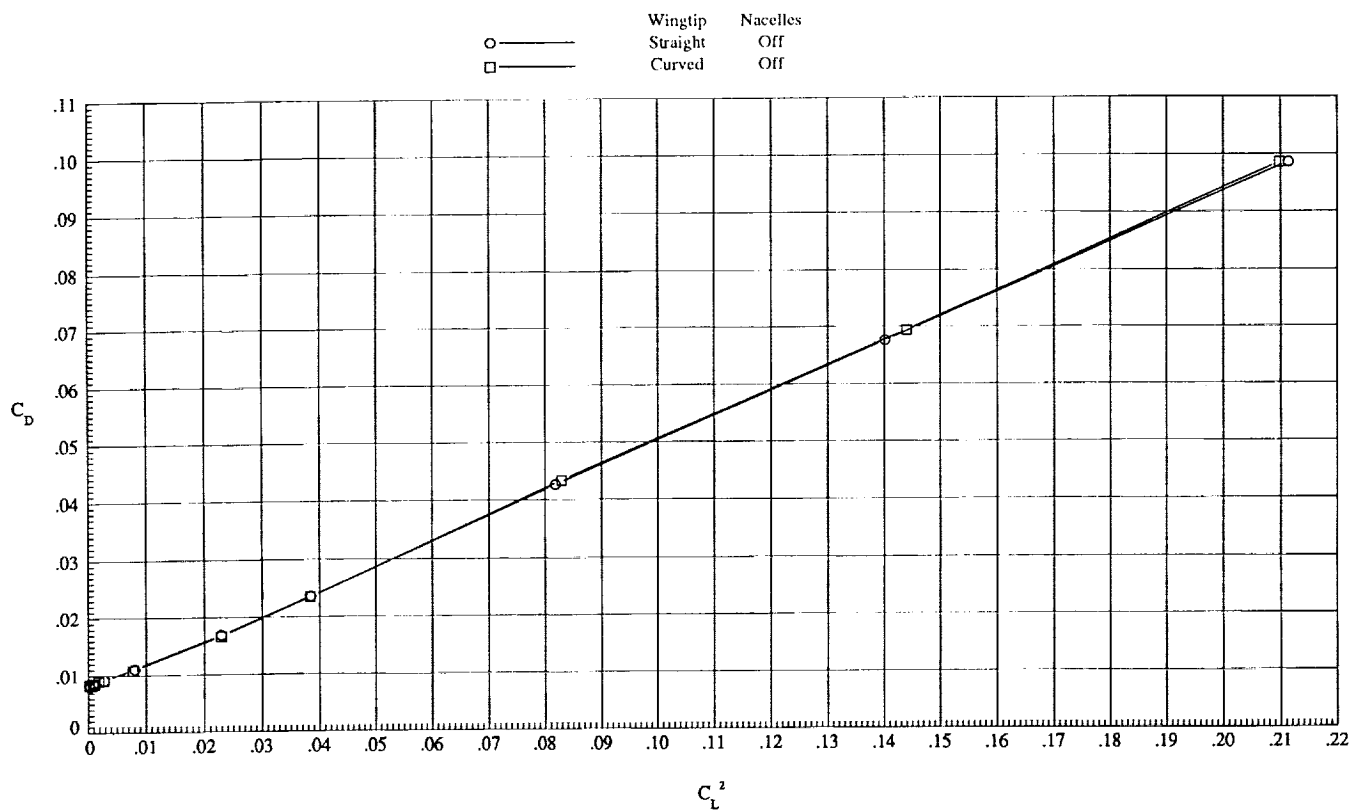
(b) $M_\infty = 0.60$.

Figure 11. Continued.



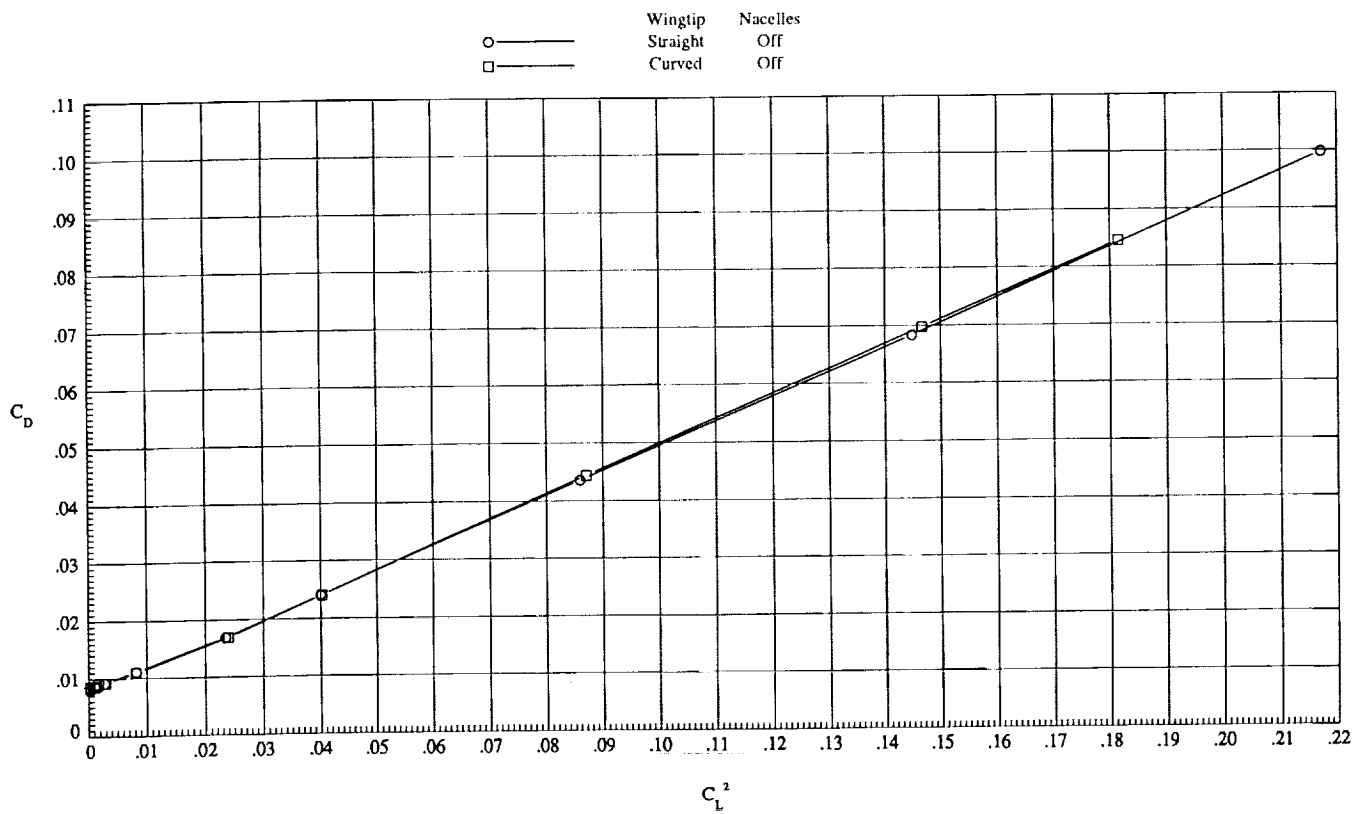
(c) $M_\infty = 0.70$.

Figure 11. Continued.



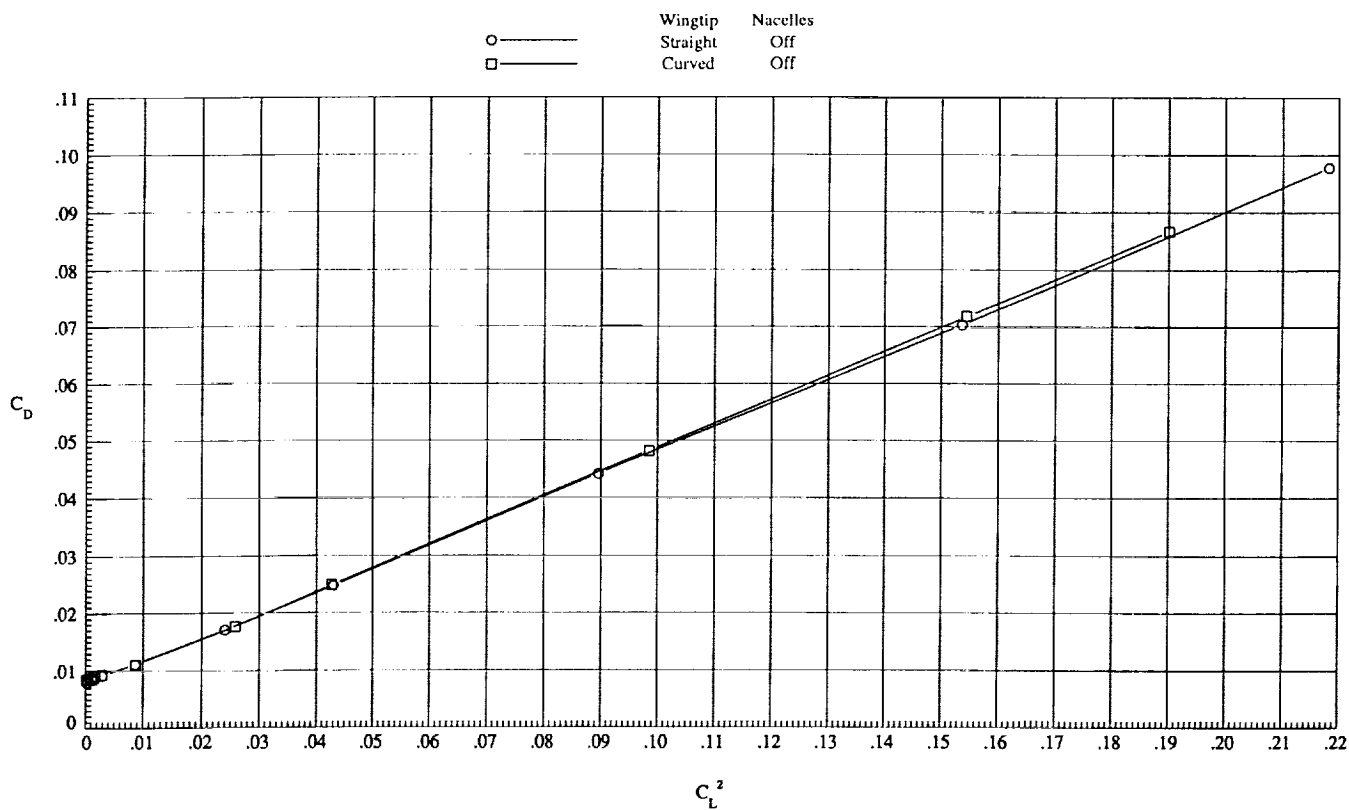
(d) $M_\infty = 0.75$.

Figure 11. Continued.



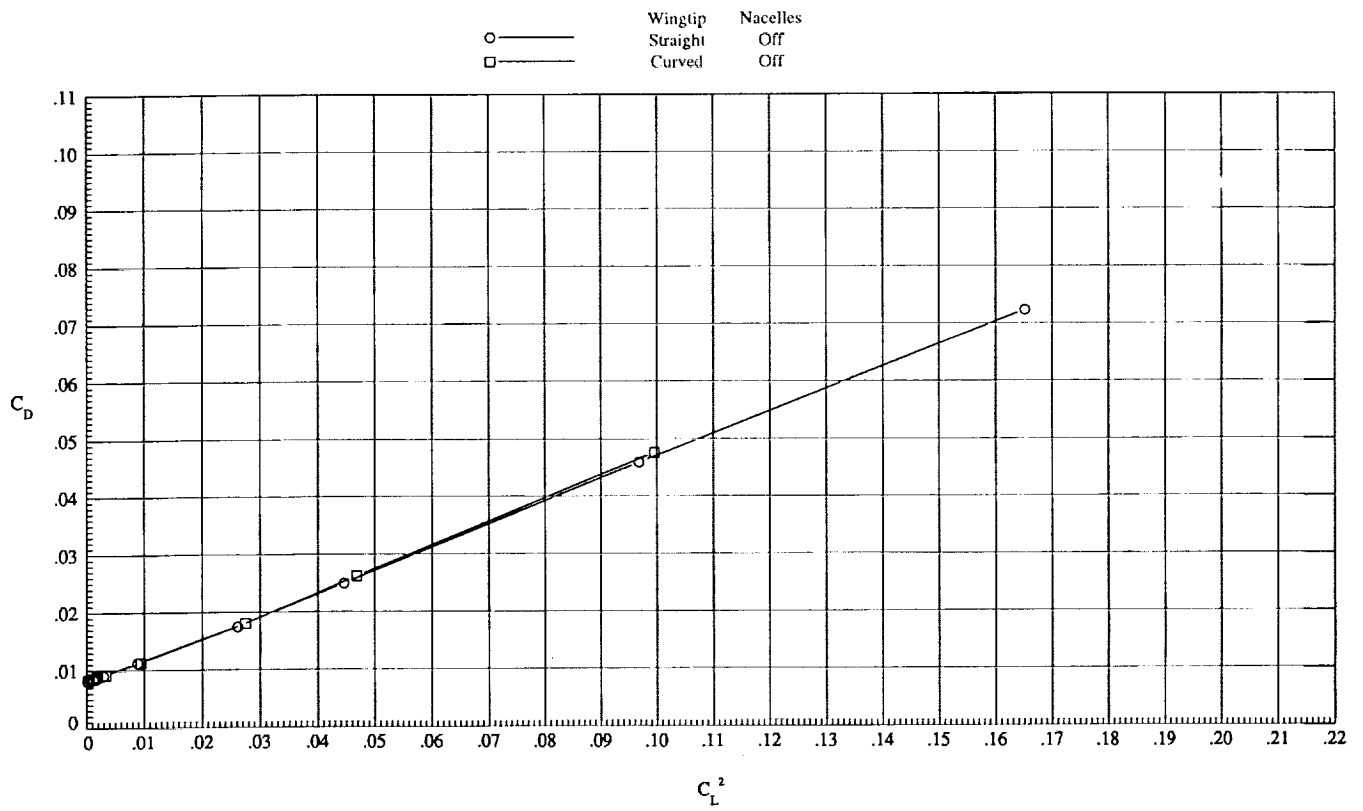
(e) $M_\infty = 0.80$.

Figure 11. Continued.



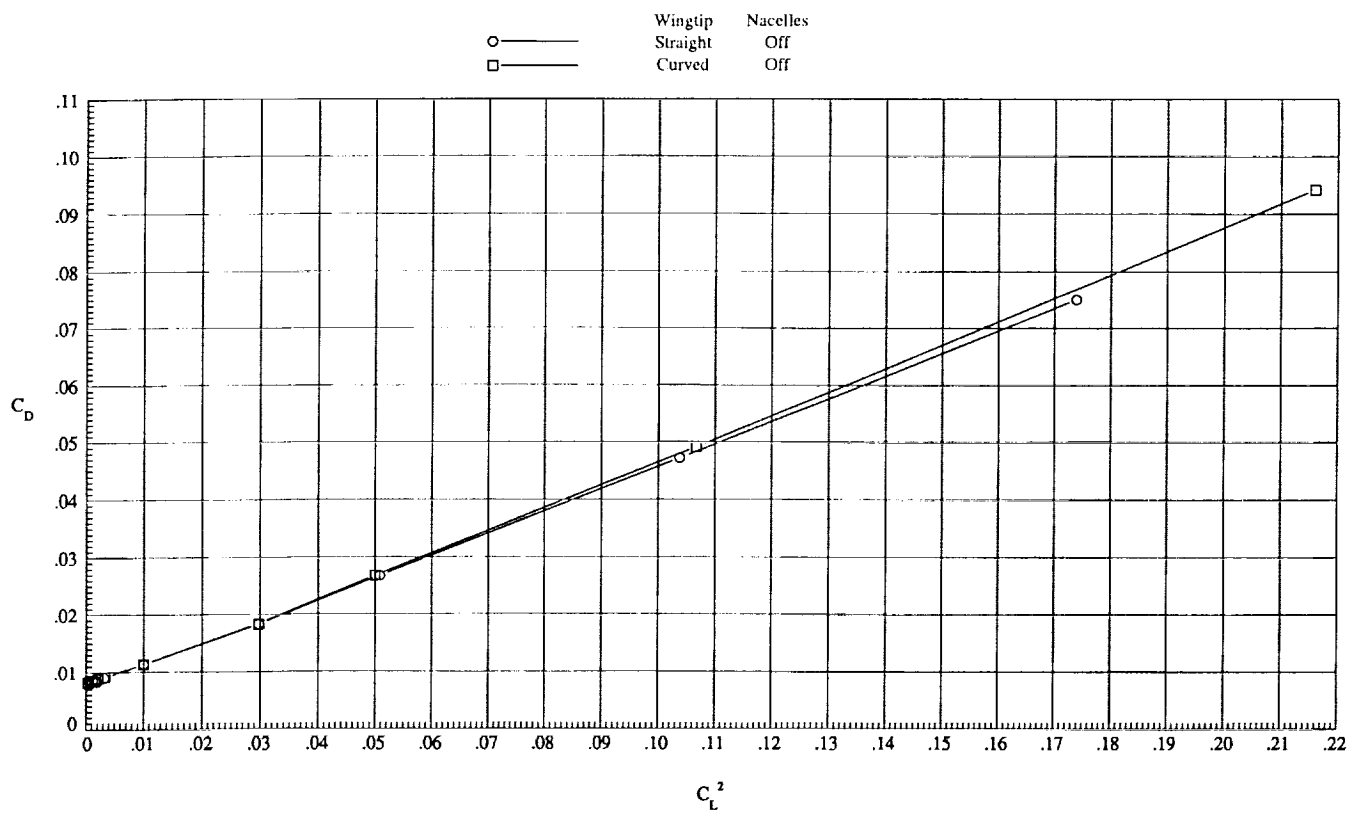
(f) $M_\infty = 0.85$.

Figure 11. Continued.



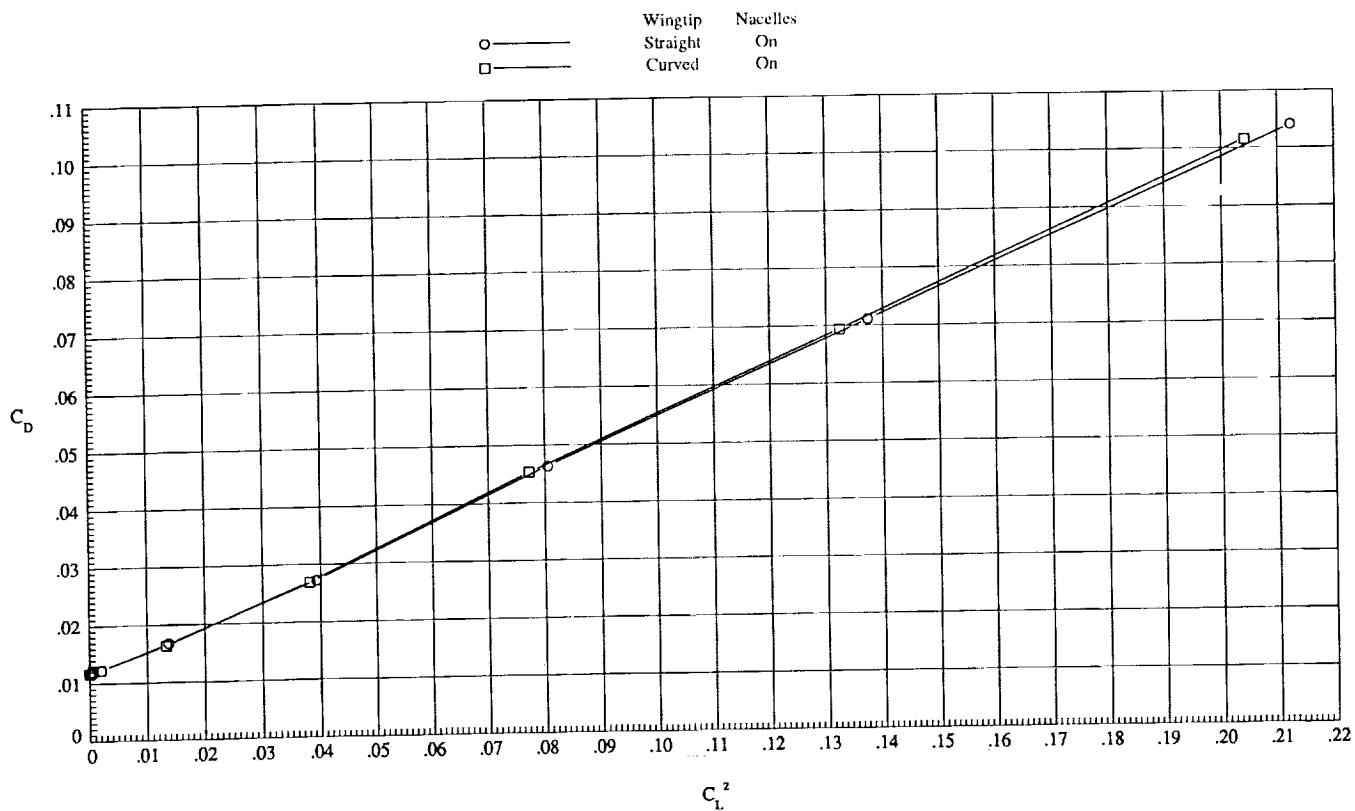
(g) $M_\infty = 0.90$.

Figure 11. Continued.



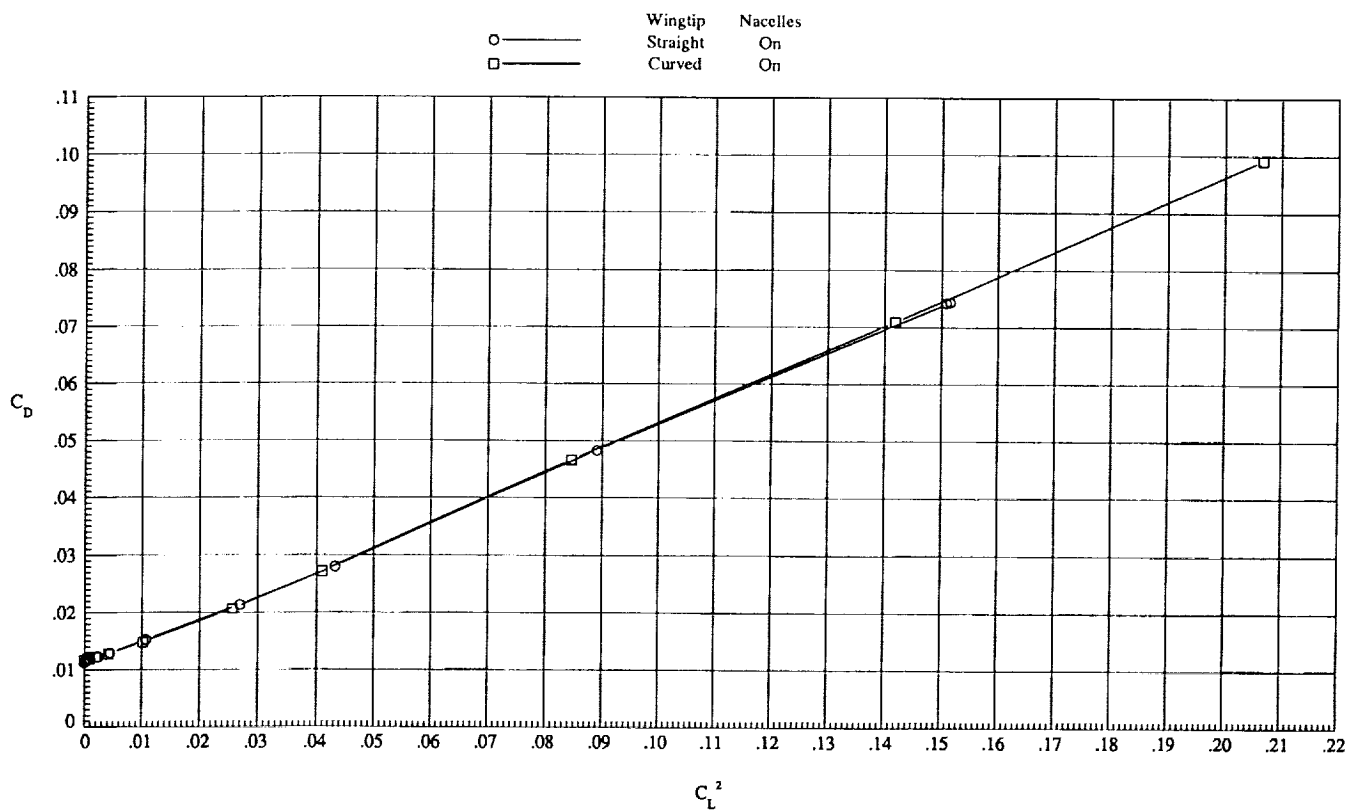
(h) $M_\infty = 0.95$.

Figure 11. Concluded.



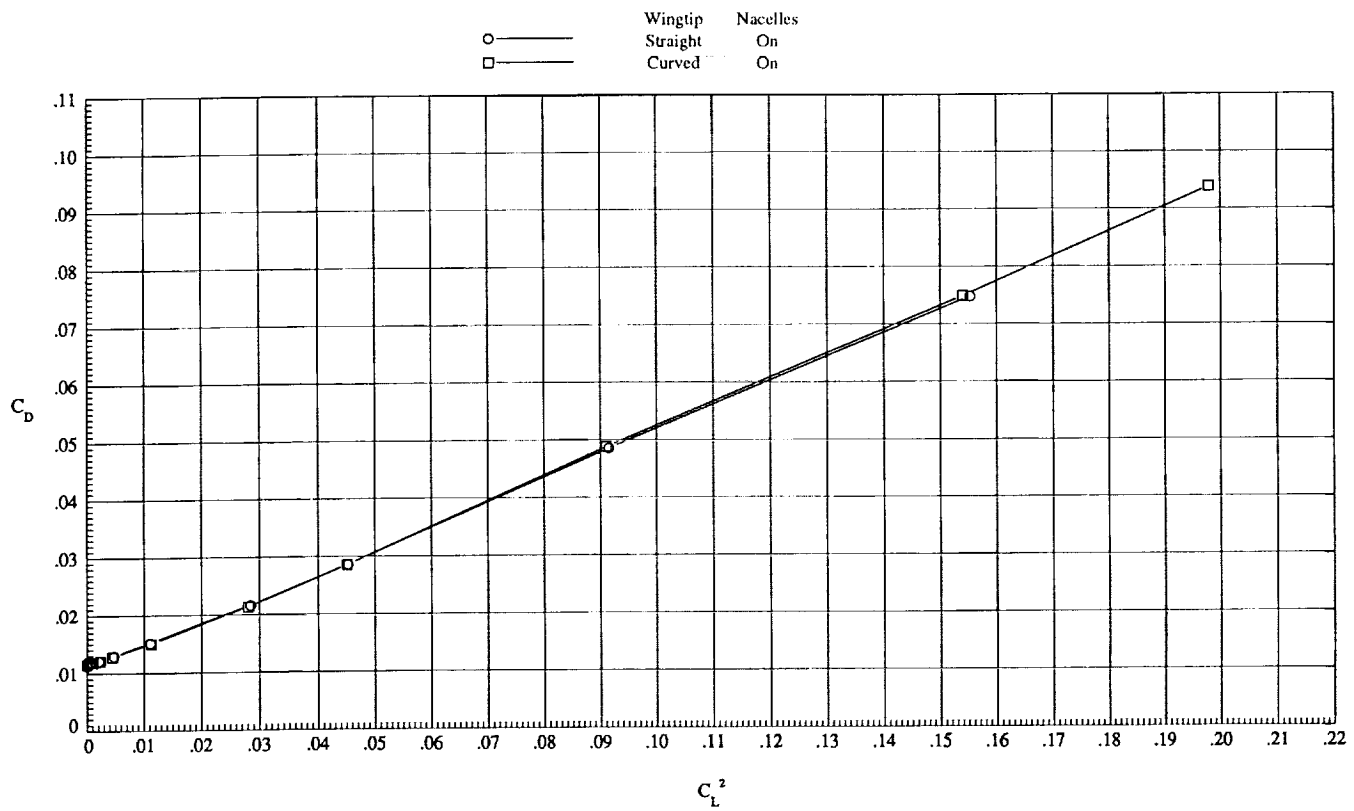
(a) $M_\infty = 0.30$.

Figure 12. Induced drag characteristics. Nacelles on.



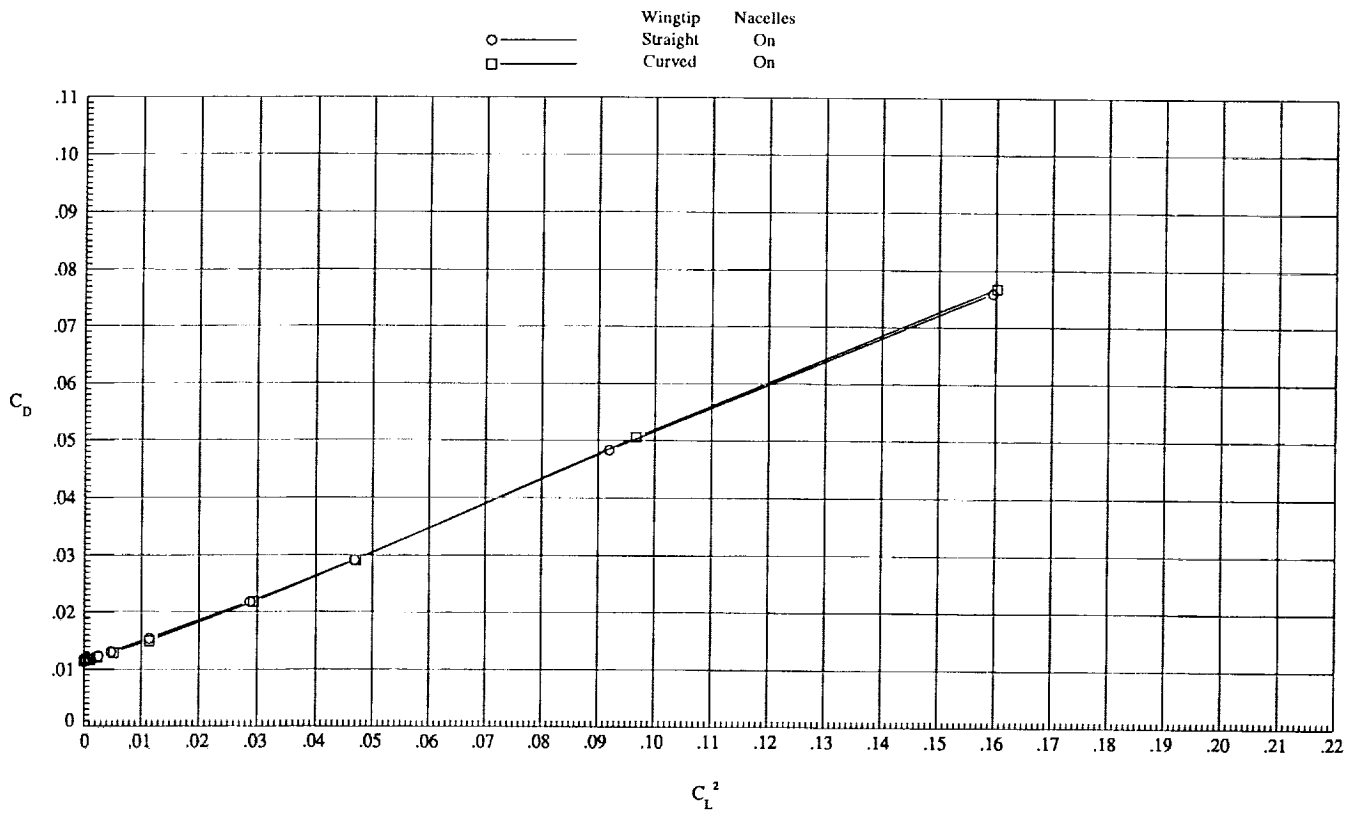
(b) $M_\infty = 0.60$.

Figure 12. Continued.



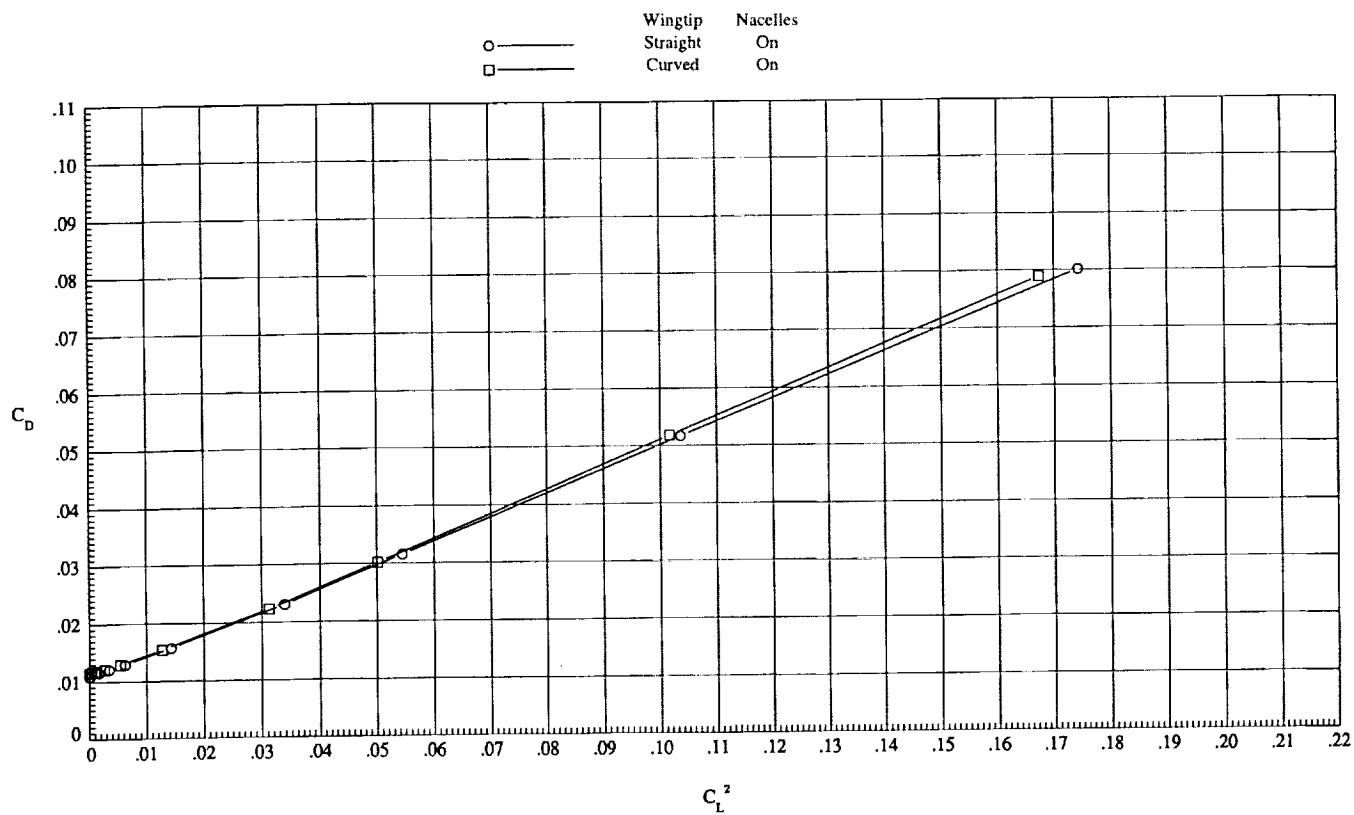
(c) $M_\infty = 0.70$.

Figure 12. Continued.



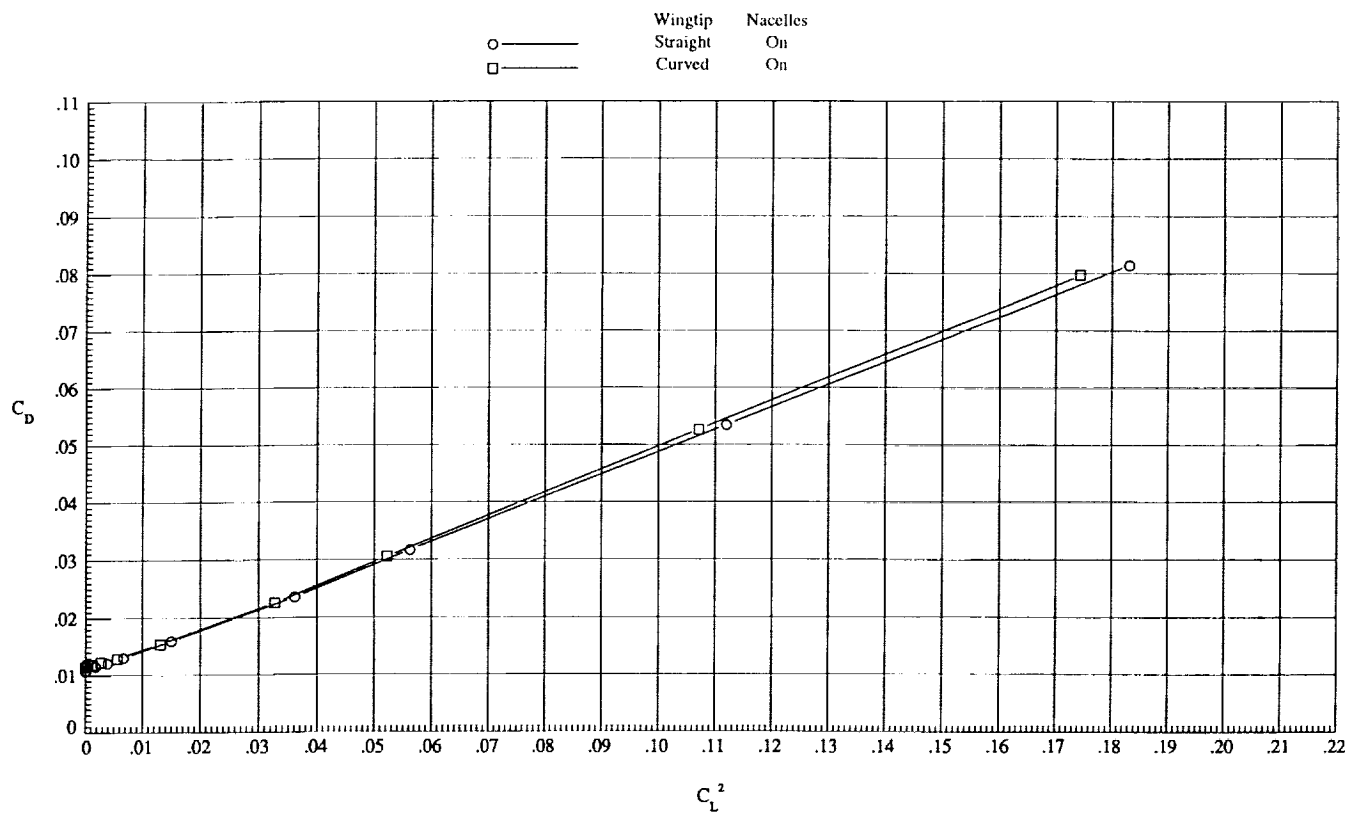
(d) $M_\infty = 0.75$.

Figure 12. Continued.



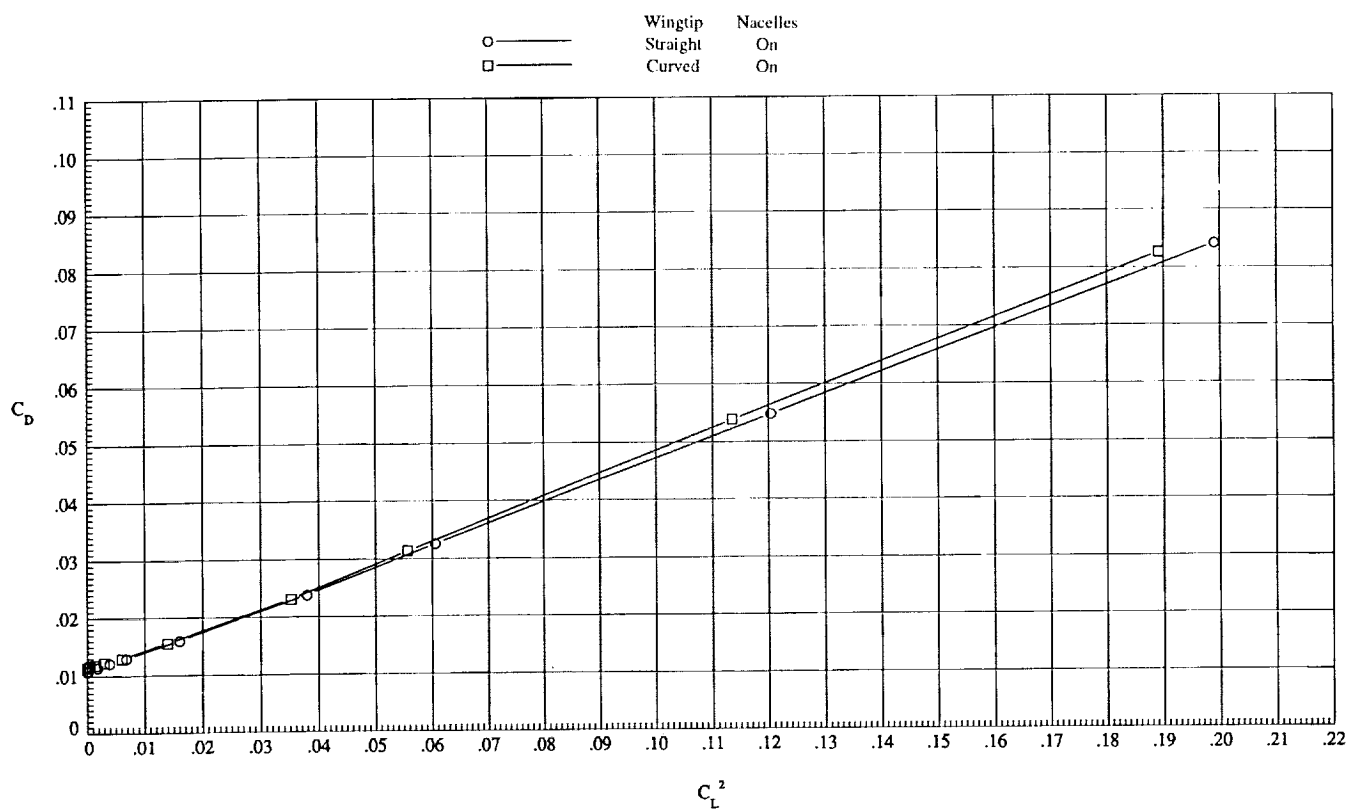
(e) $M_\infty = 0.80$.

Figure 12. Continued.



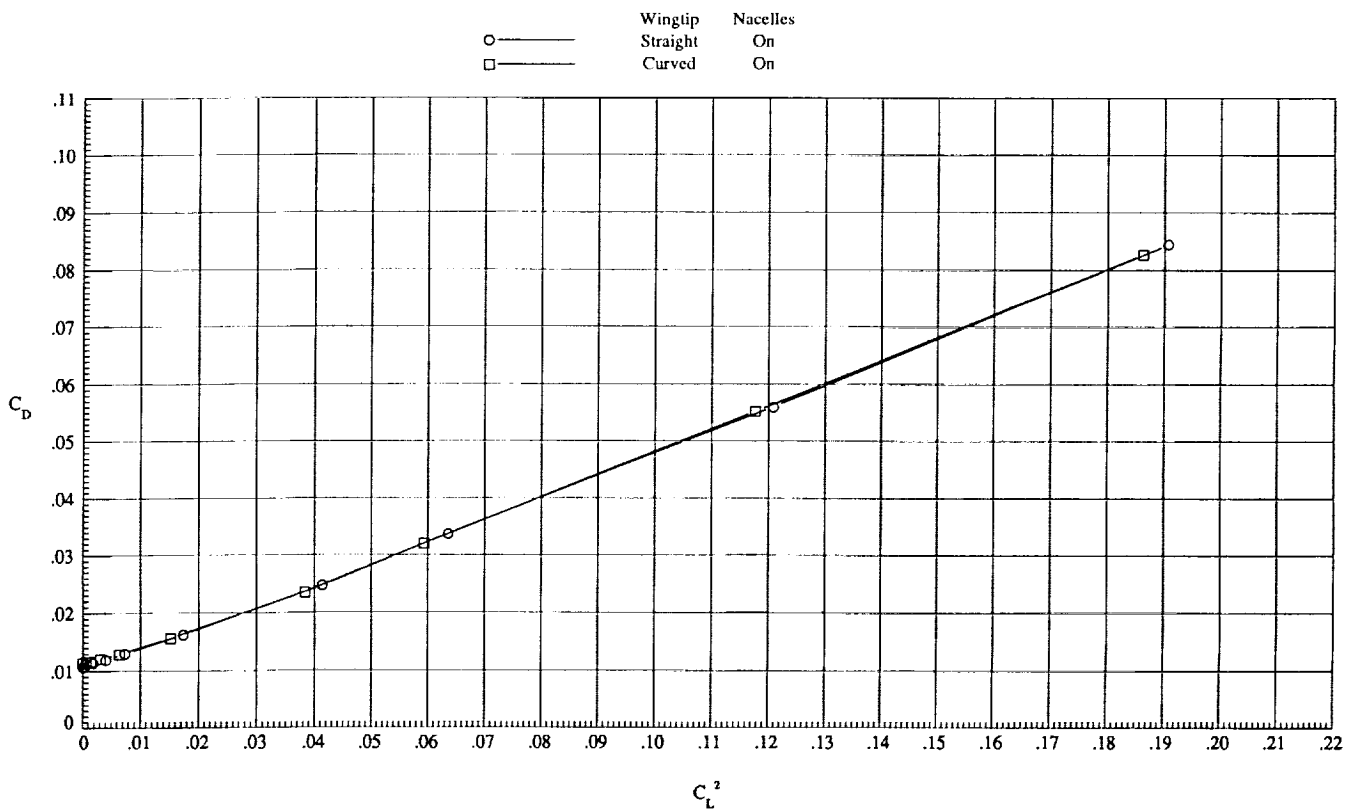
(f) $M_\infty = 0.85$.

Figure 12. Continued.



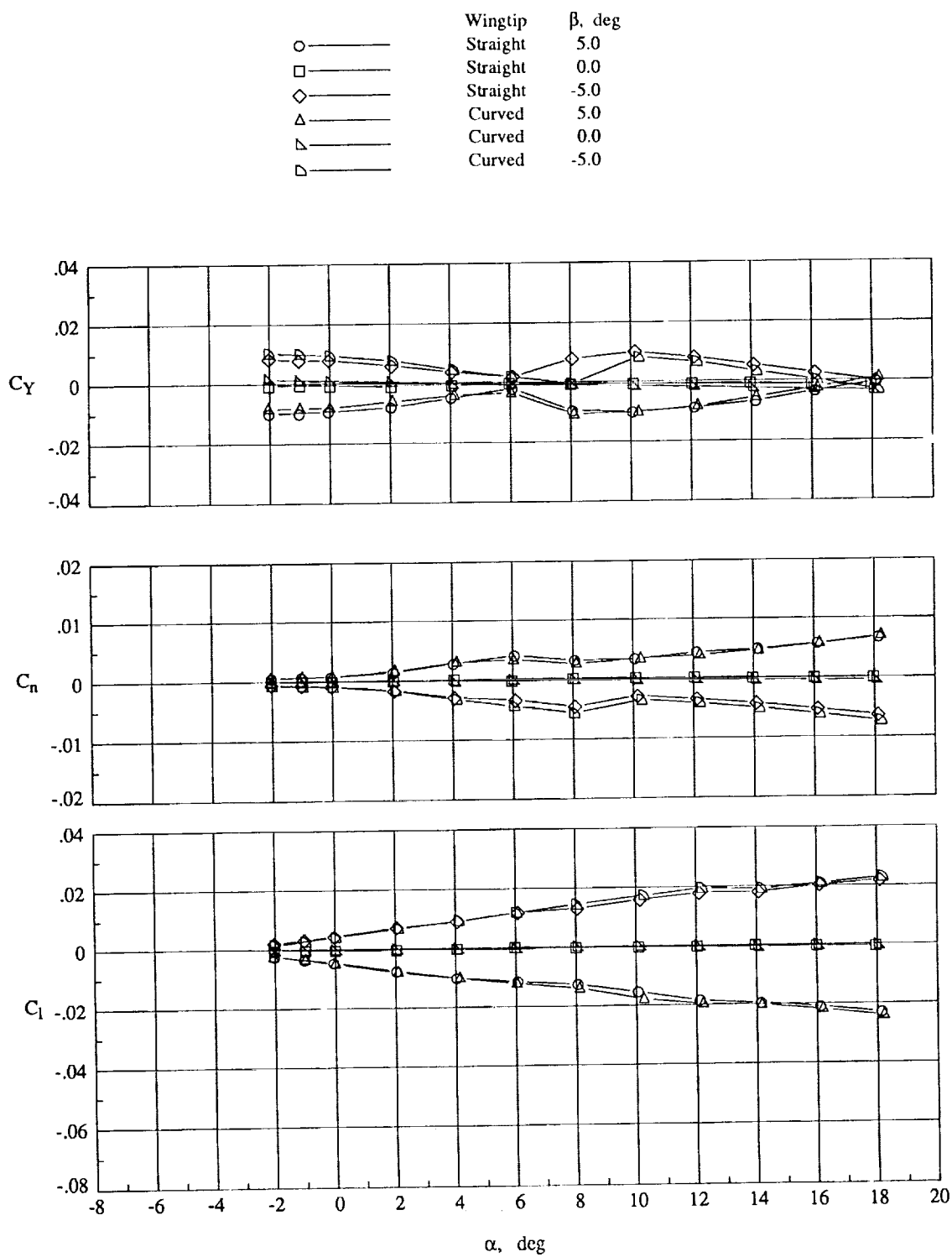
(g) $M_\infty = 0.90$.

Figure 12. Continued.



(h) $M_\infty = 0.95$.

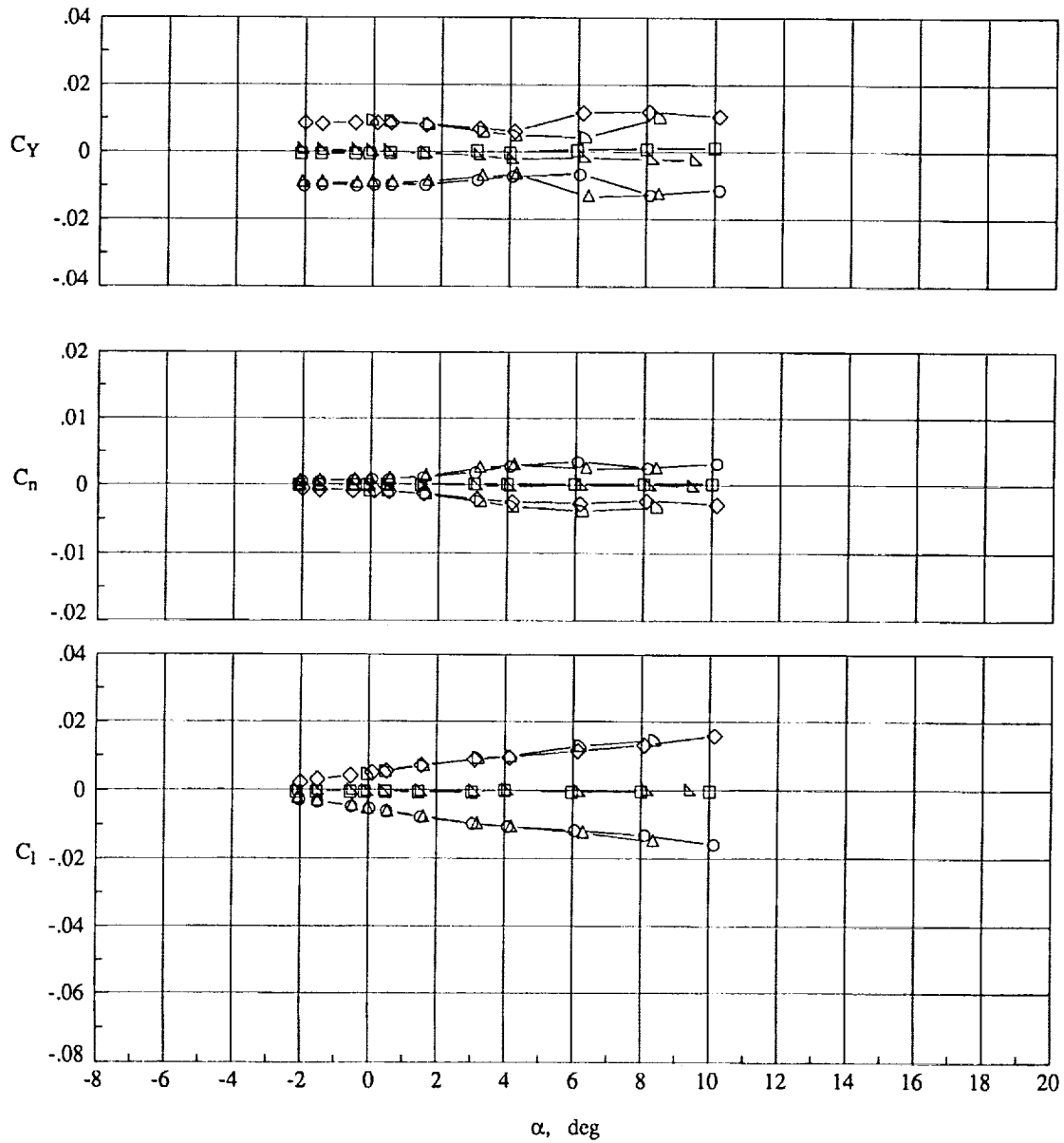
Figure 12. Concluded.



(a) $M_\infty = 0.30$.

Figure 13. Lateral characteristics of the straight and curved wingtip models with nacelles on.

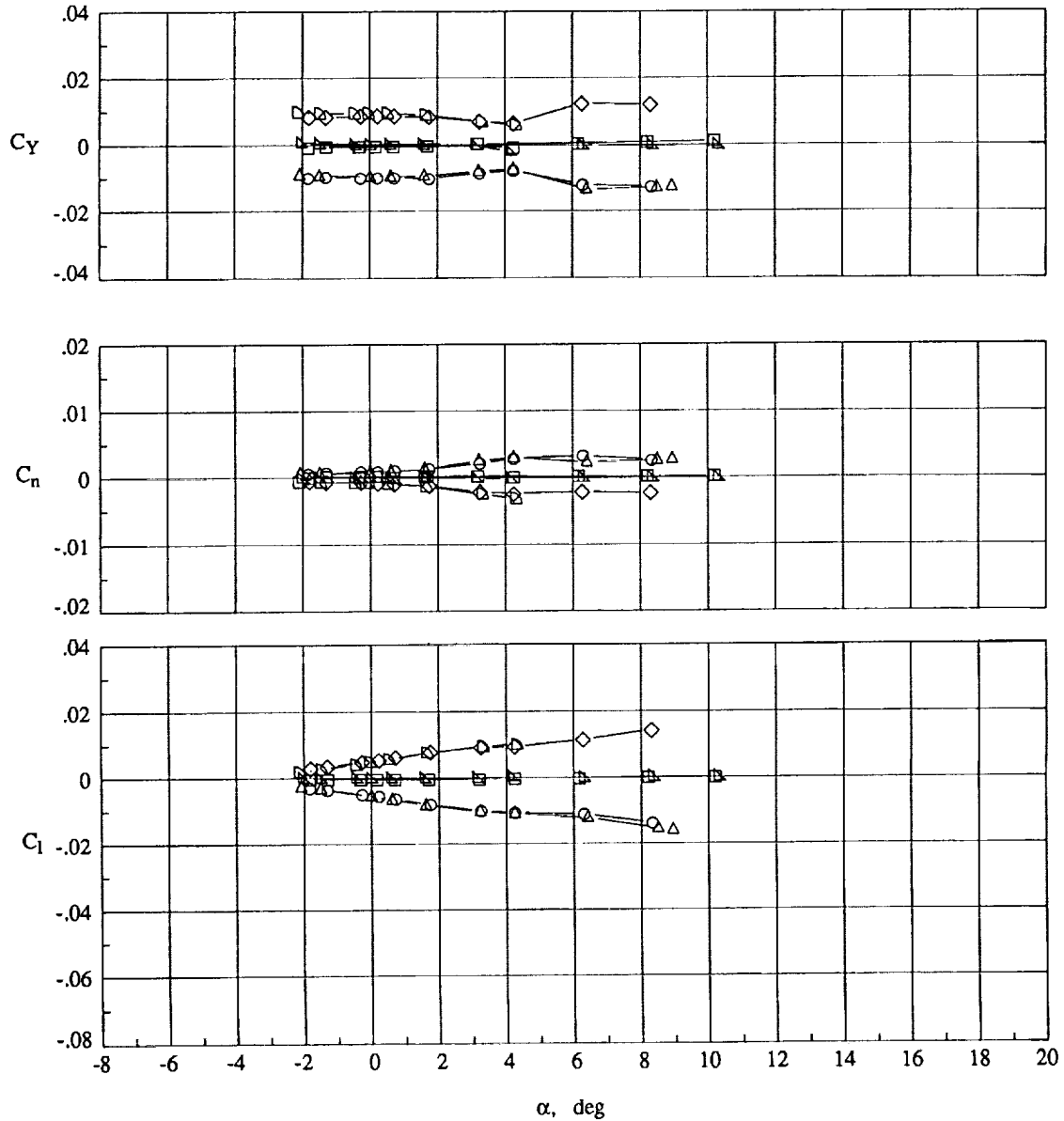
	Wingtip	β , deg
○	Straight	5.0
□	Straight	0.0
◇	Straight	-5.0
△	Curved	5.0
▴	Curved	0.0
▾	Curved	-5.0



(b) $M_\infty = 0.70$.

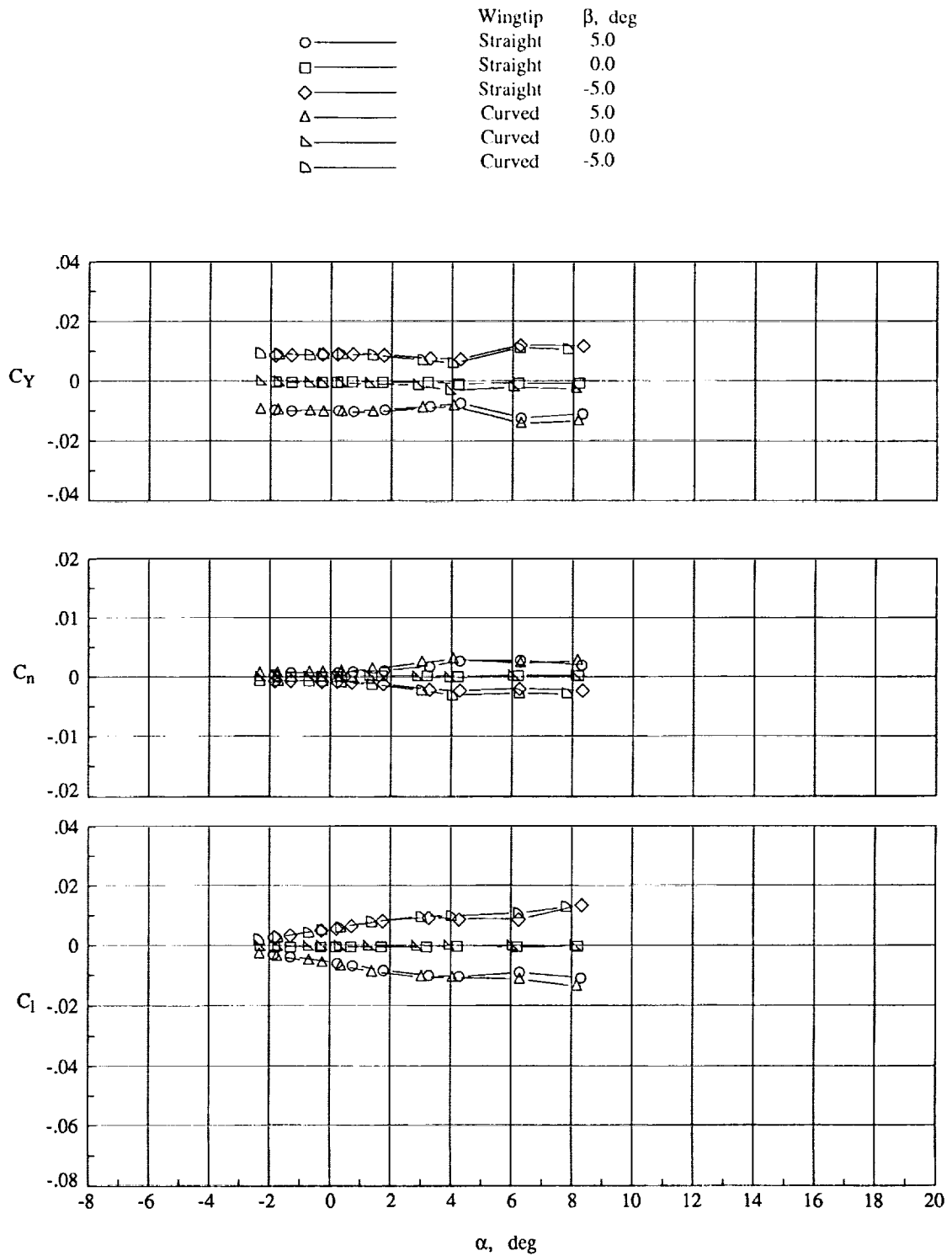
Figure 13. Continued.

	Wingtip	β , deg
○	Straight	5.0
□	Straight	0.0
◇	Straight	-5.0
△	Curved	5.0
▴	Curved	0.0
▾	Curved	-5.0



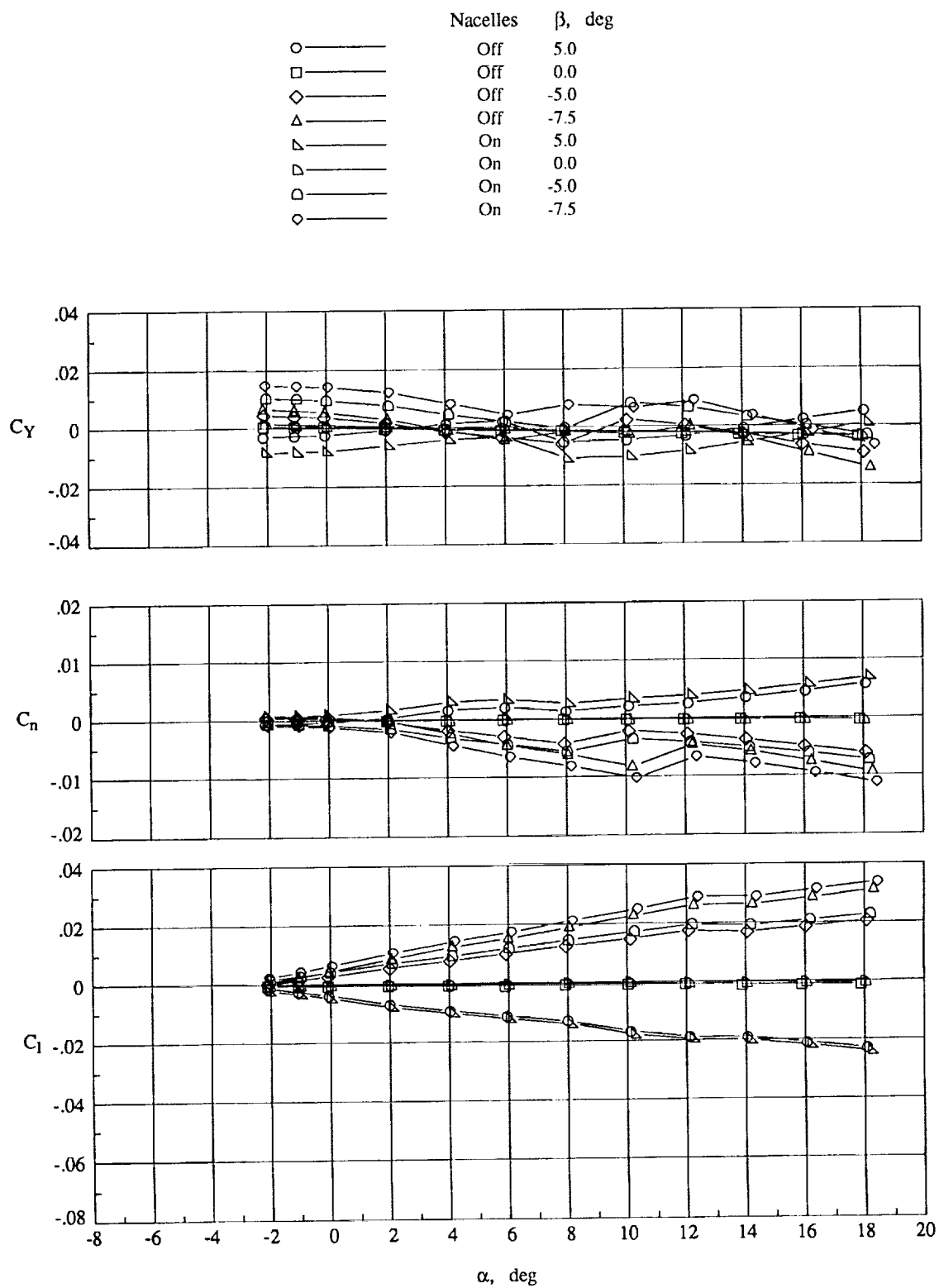
(c) $M_\infty = 0.80$.

Figure 13. Continued.



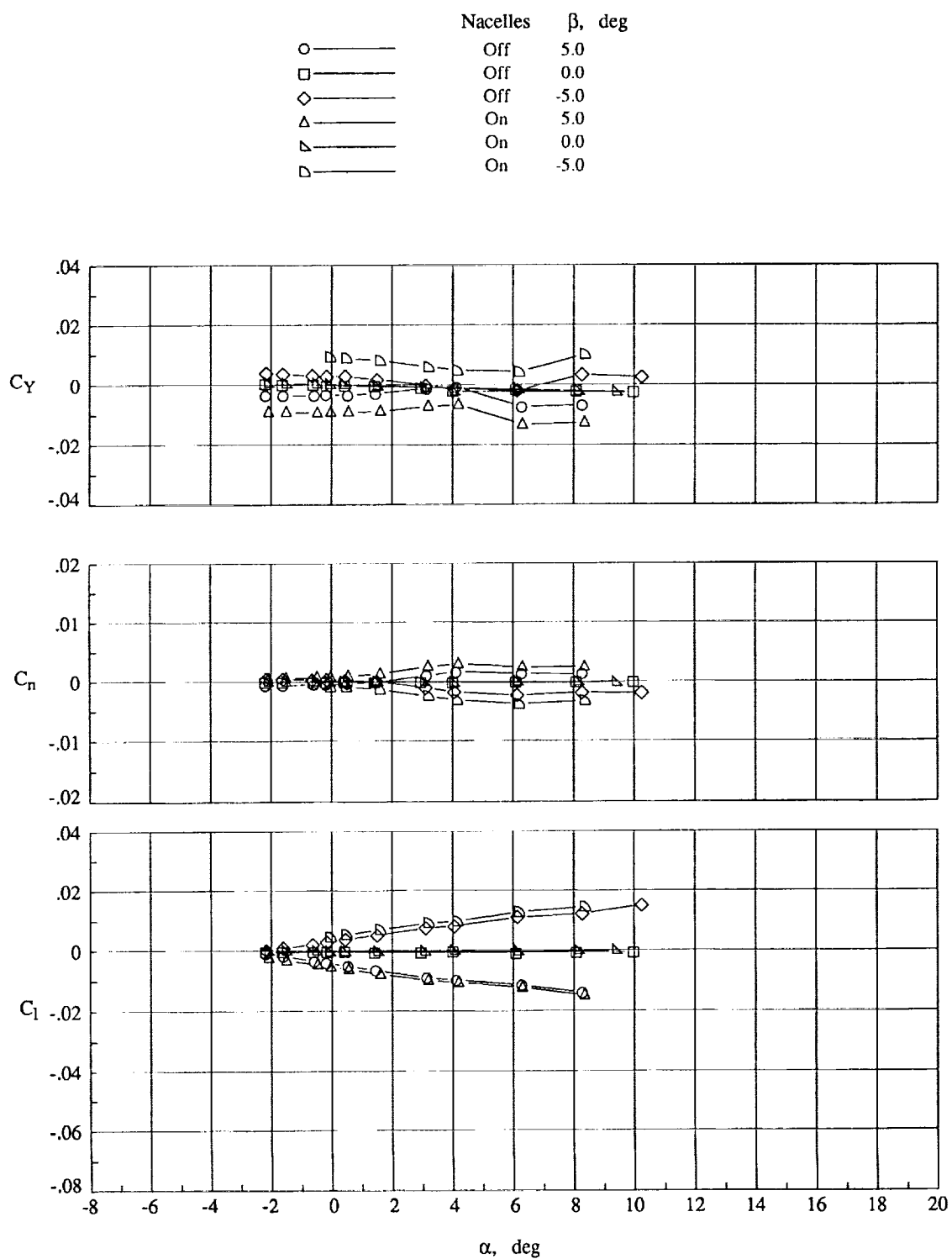
(d) $M_\infty = 0.90$.

Figure 13. Concluded.



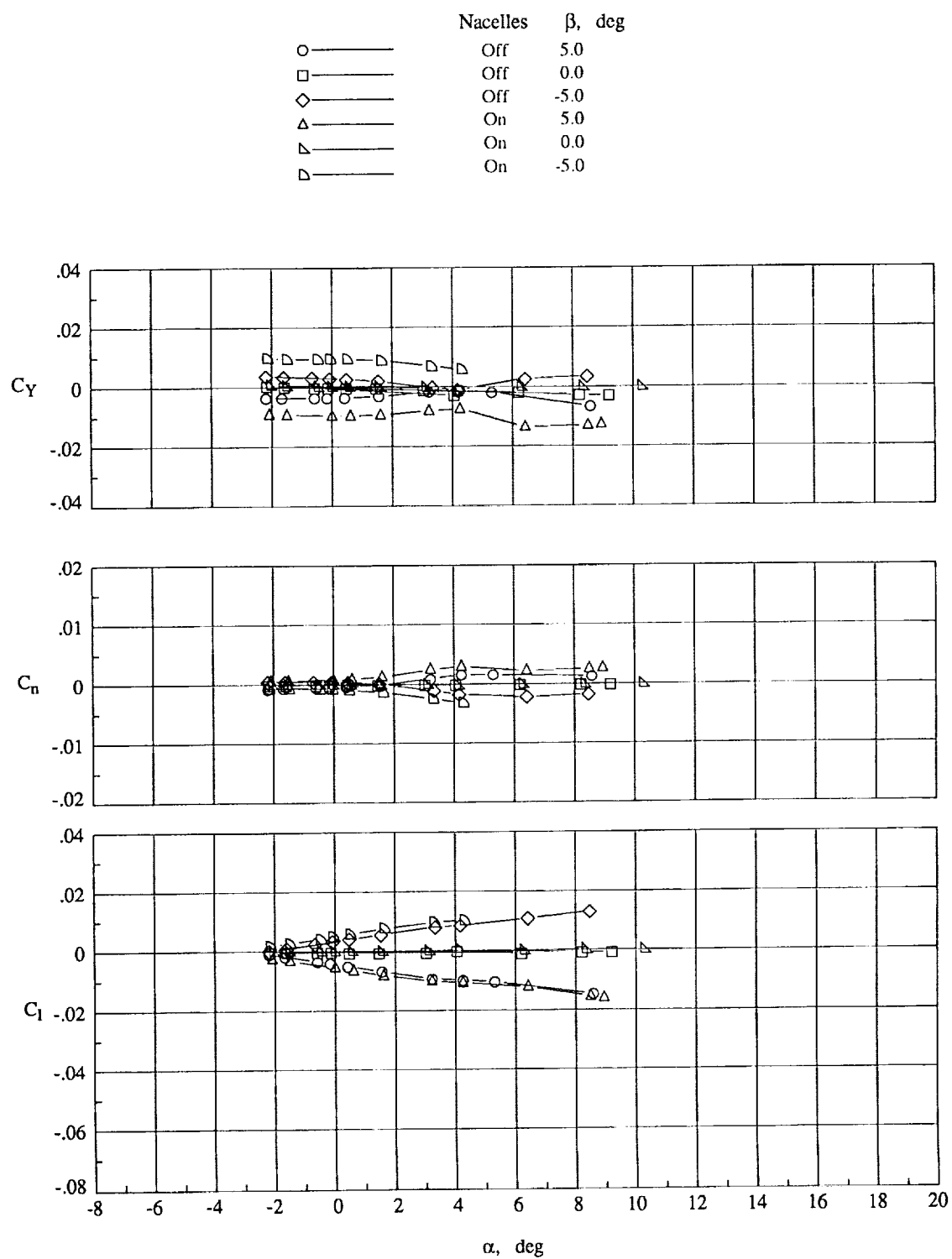
(a) $M_\infty = 0.30$.

Figure 14. Lateral characteristics of the curved wingtip model.



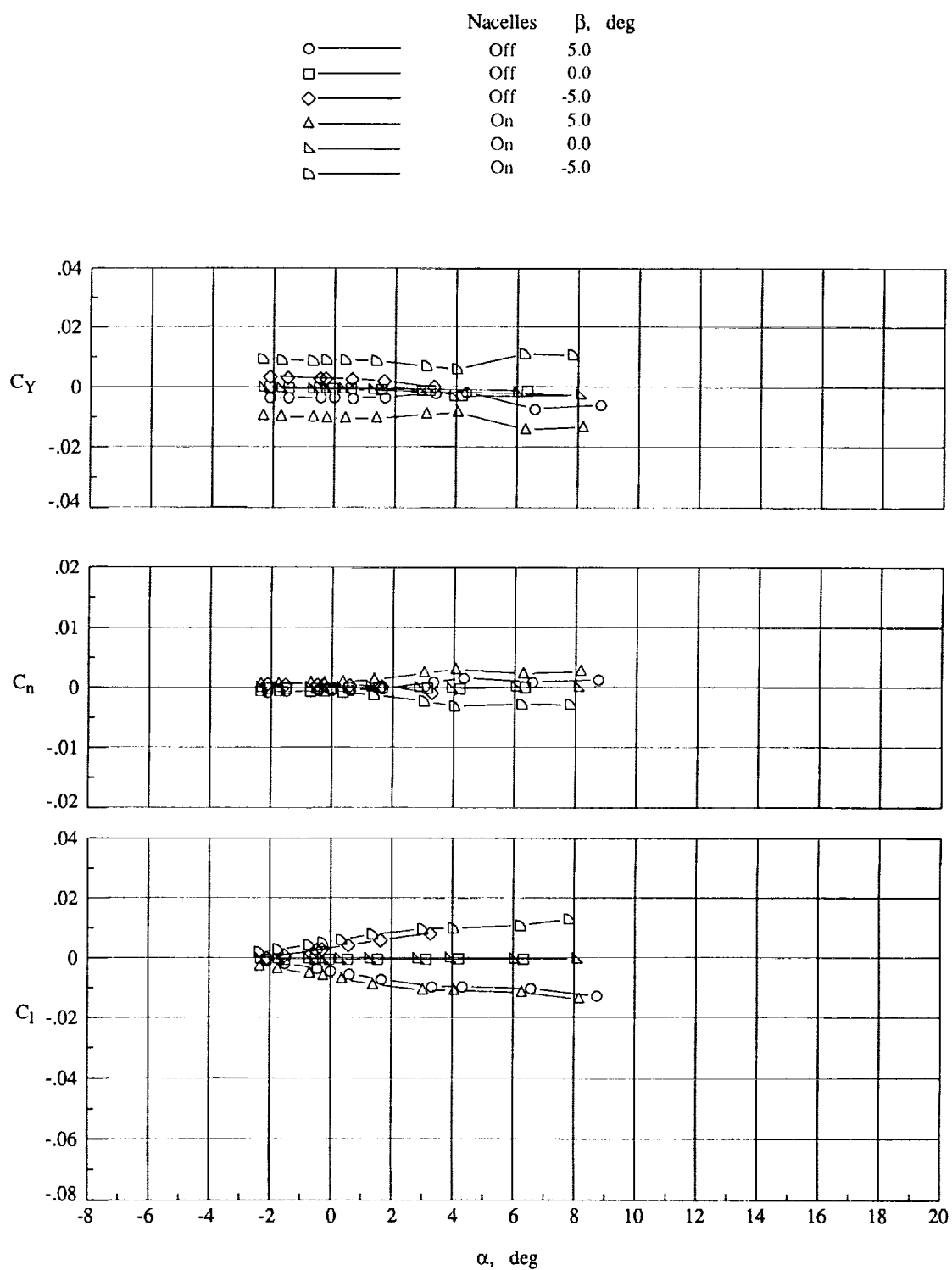
(b) $M_\infty = 0.70$.

Figure 14. Continued.



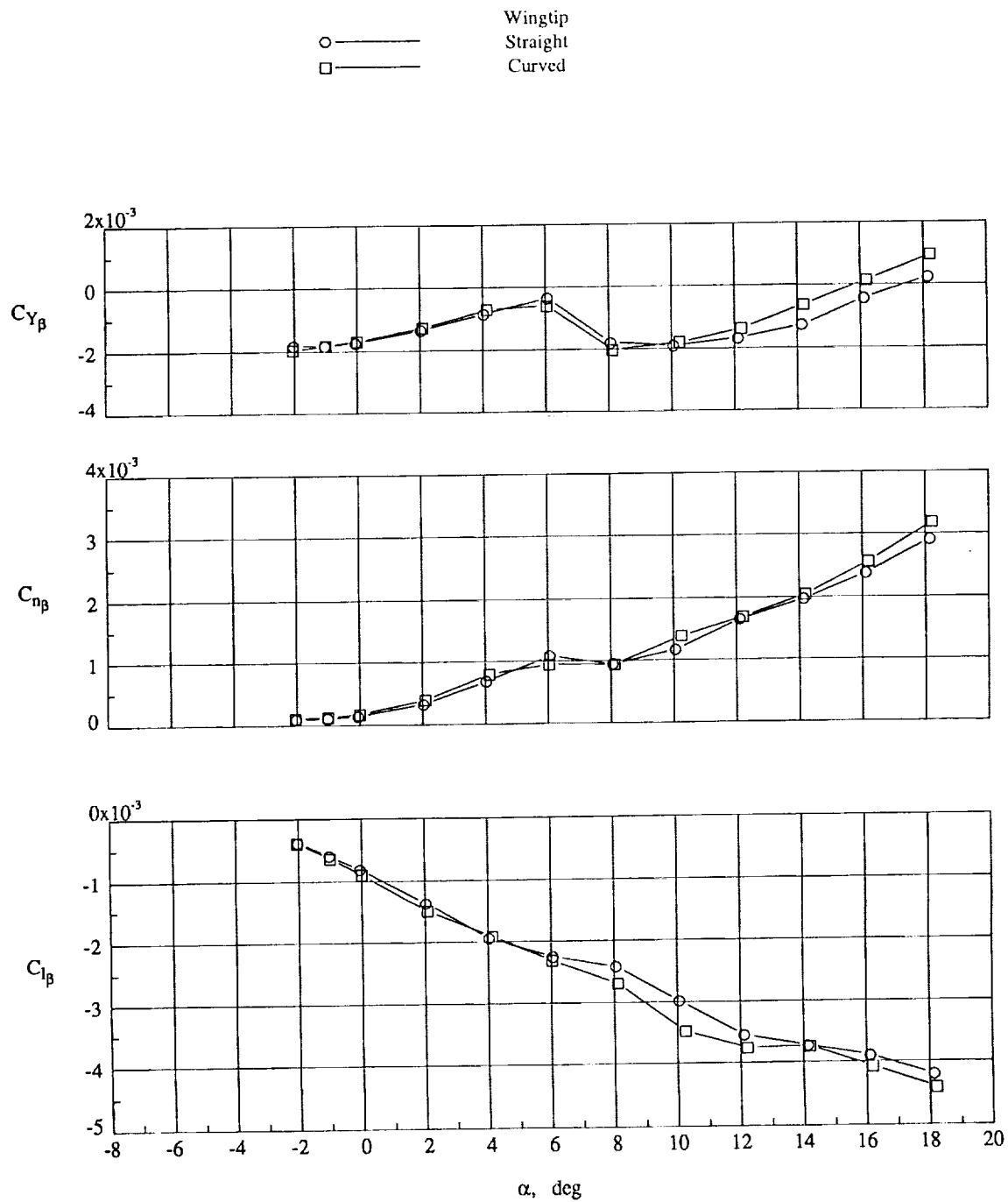
(c) $M_\infty = 0.80$.

Figure 14. Continued.



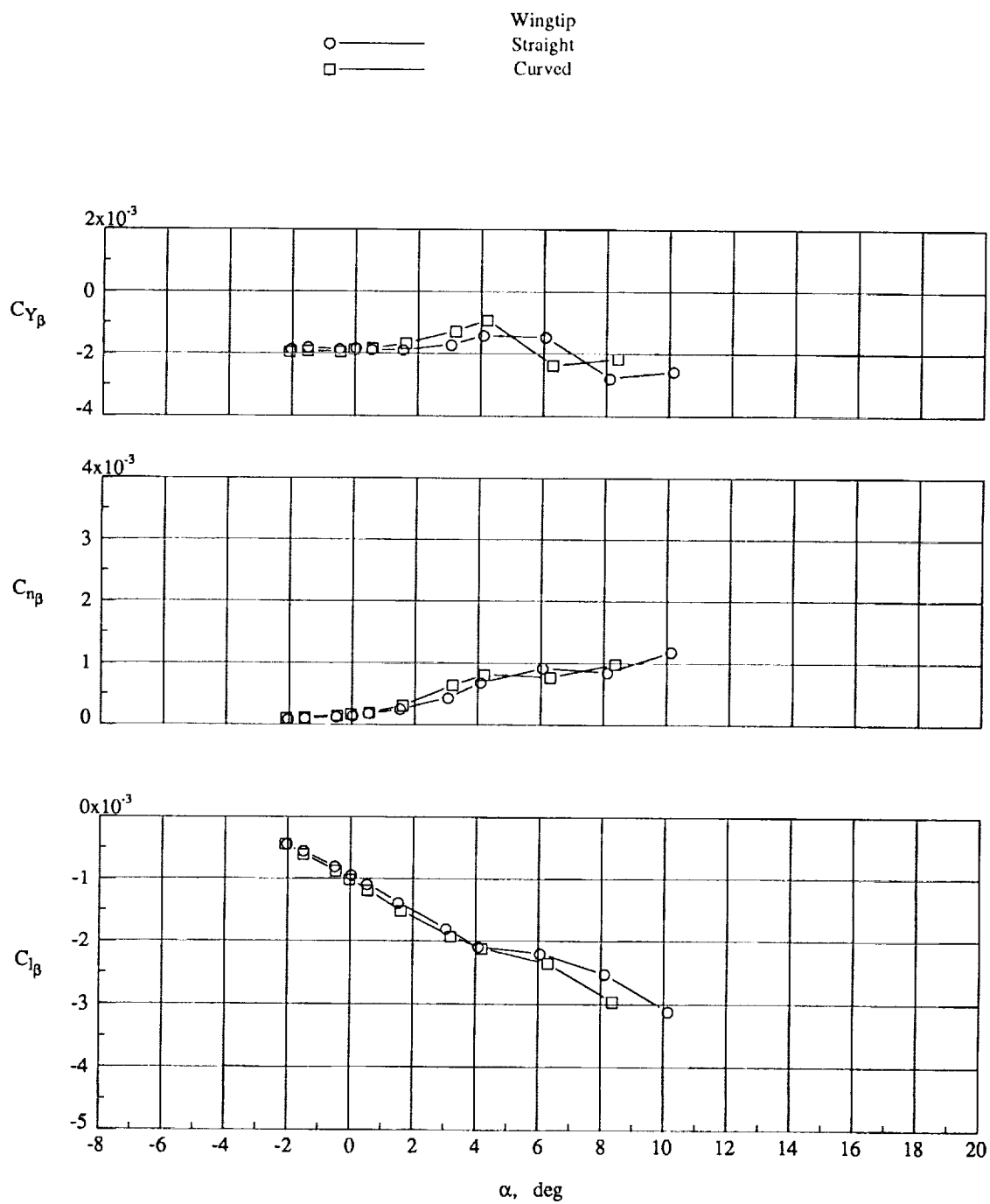
(d) $M_\infty = 0.90$.

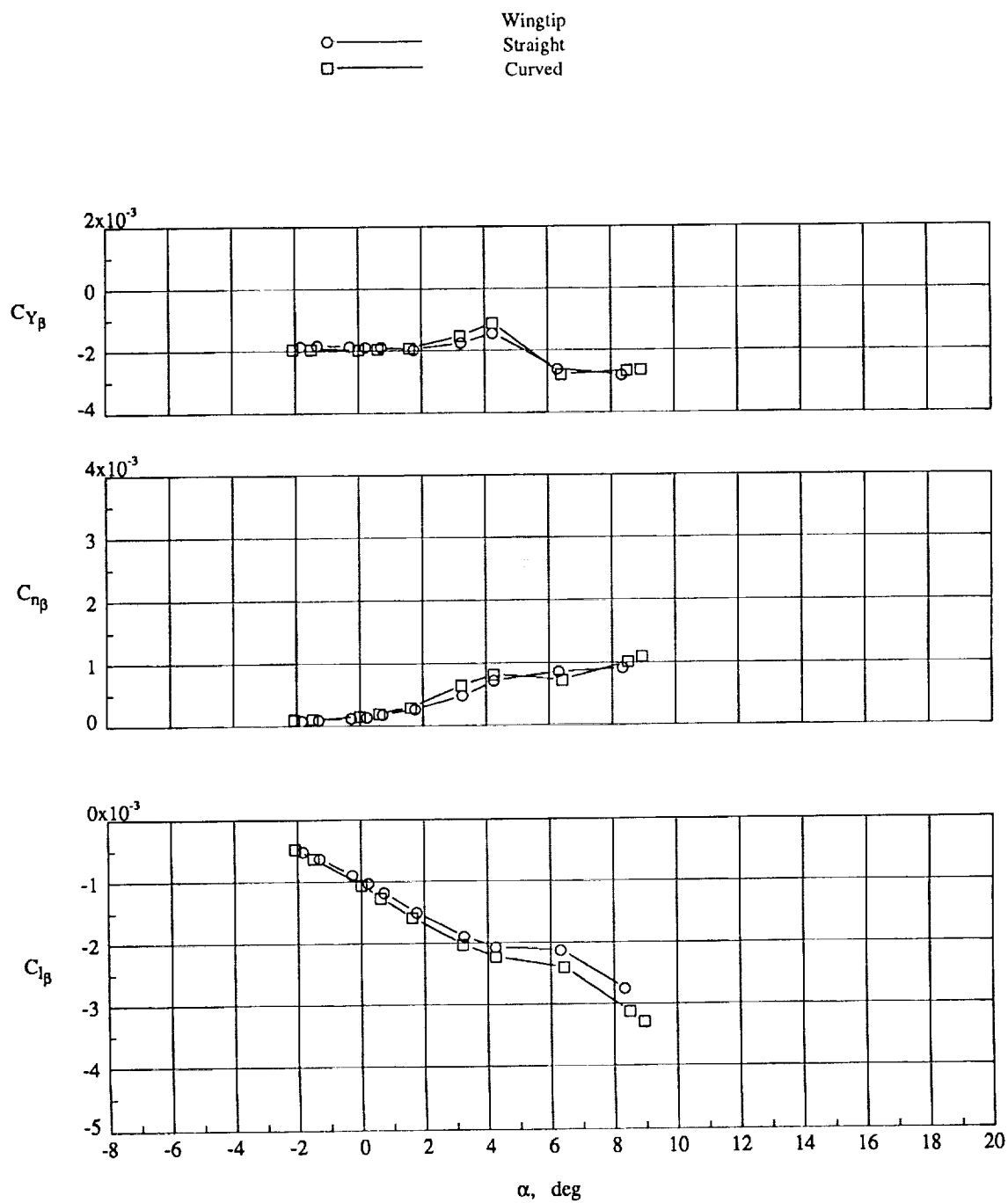
Figure 14. Concluded.



(a) $M_\infty = 0.30$.

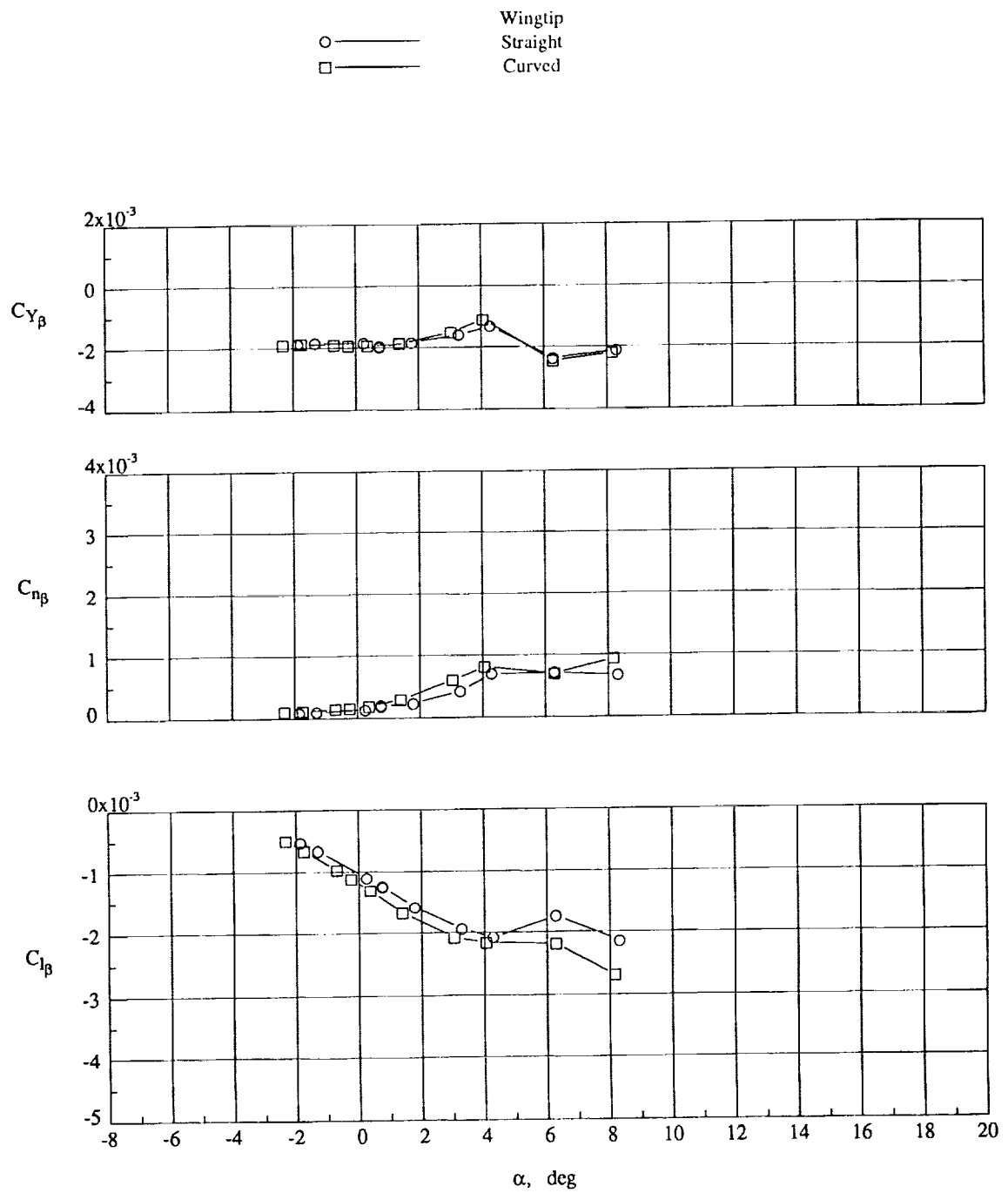
Figure 15. Lateral-directional stability derivatives of the straight and curved wingtip models with nacelles on.





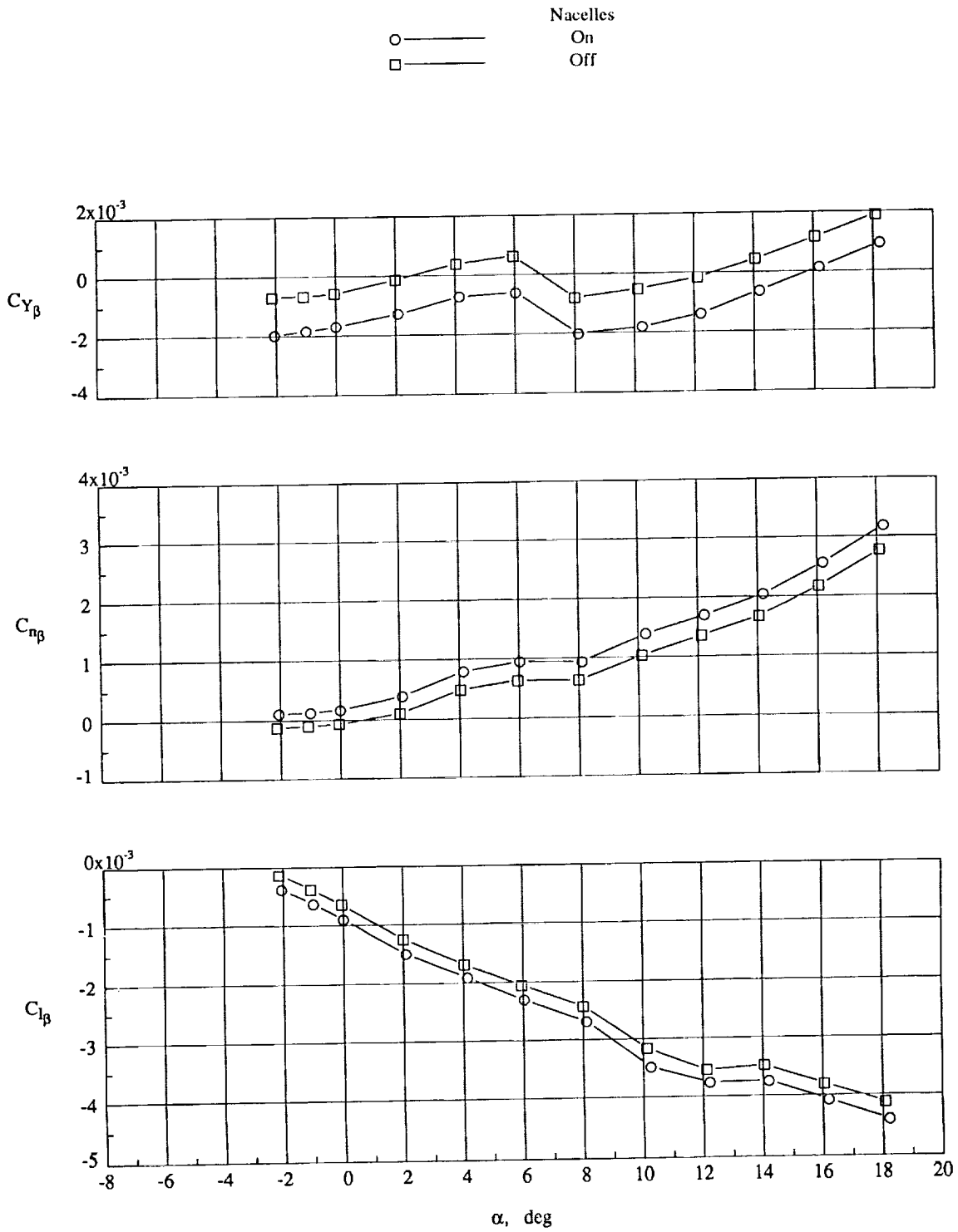
(c) $M_\infty = 0.80$.

Figure 15. Continued.



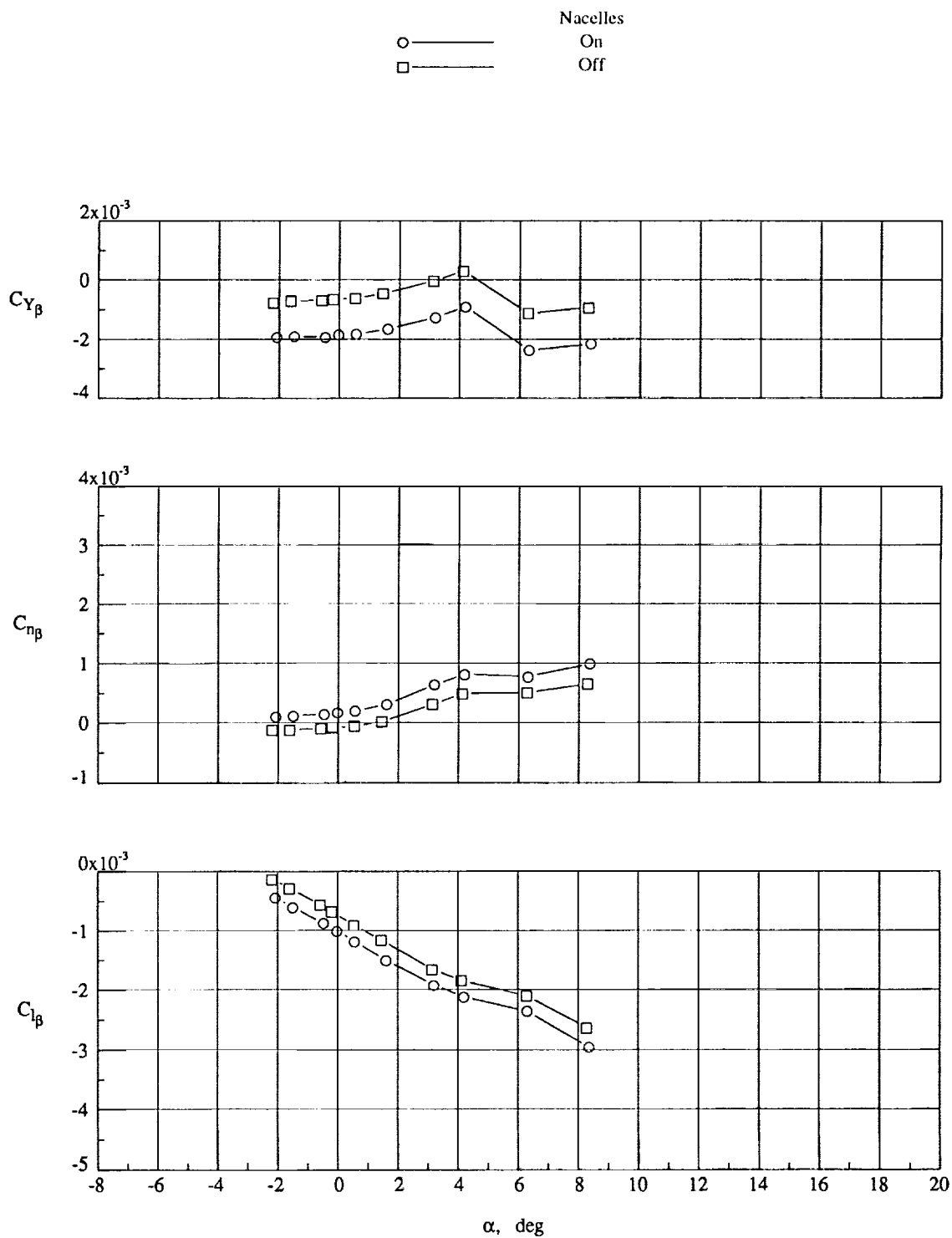
(d) $M_{\infty} = 0.90$.

Figure 15. Concluded.



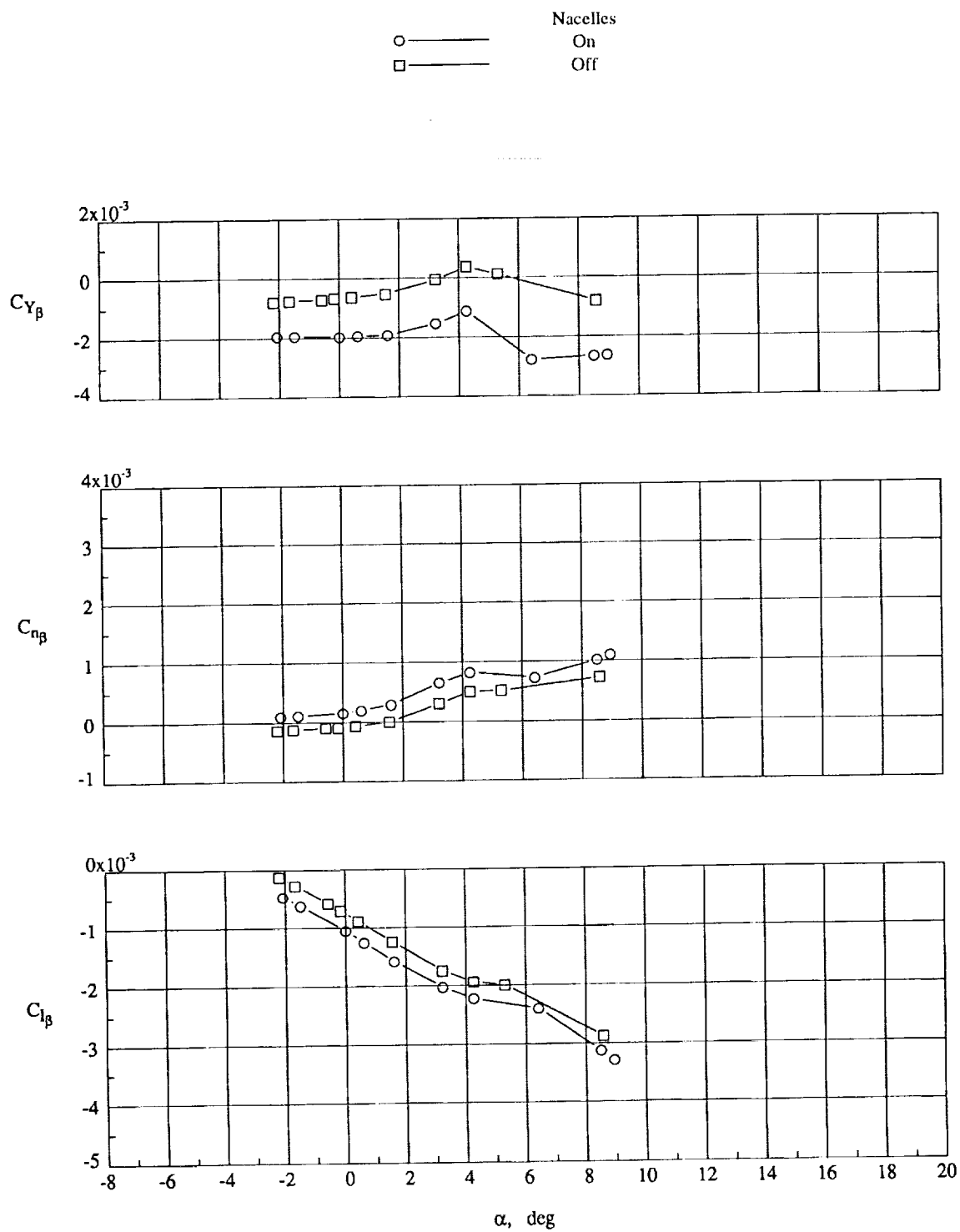
(a) $M_\infty = 0.30$.

Figure 16. Lateral-directional stability derivatives of the curved wingtip model.



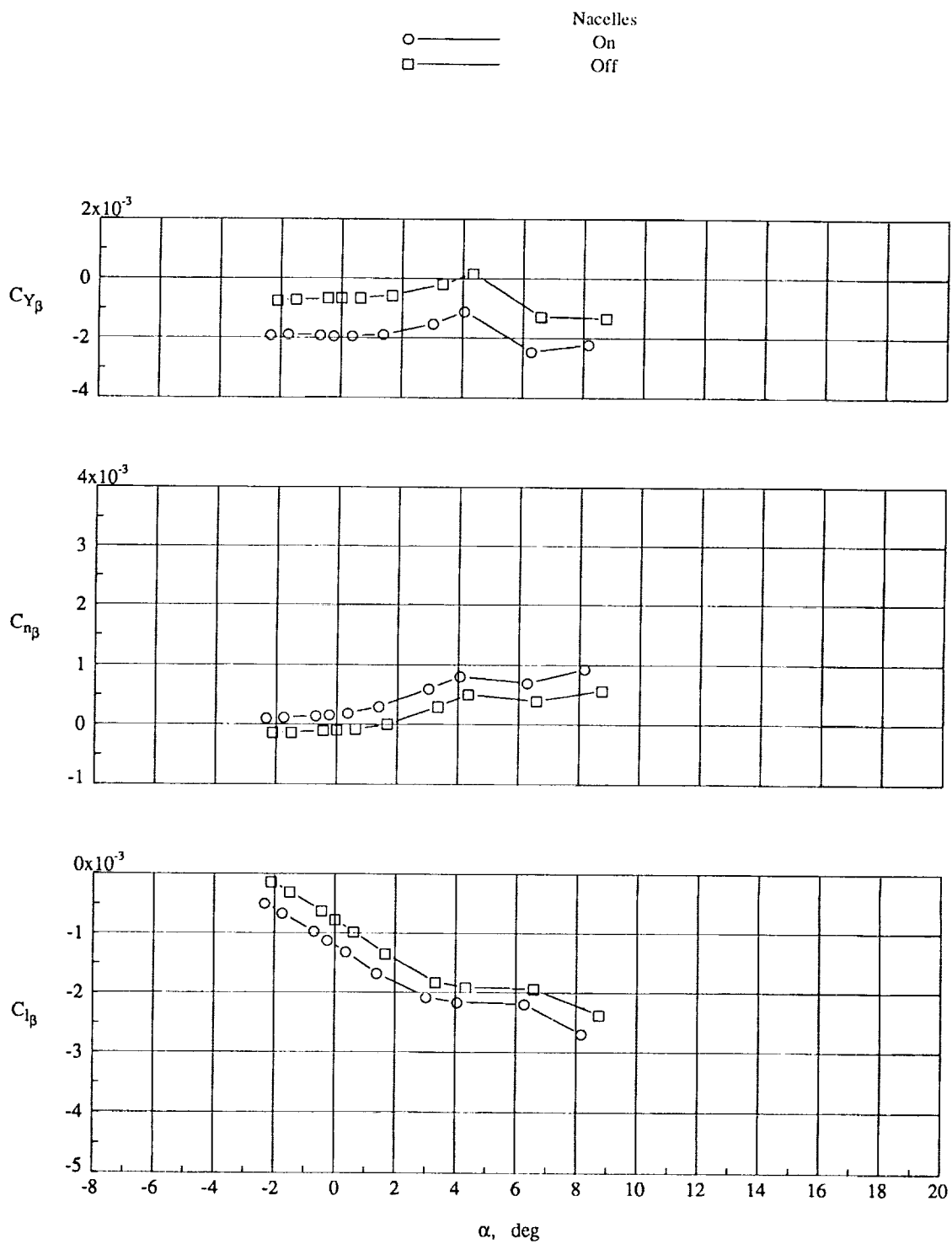
(b) $M_\infty = 0.70$.

Figure 16. Continued.



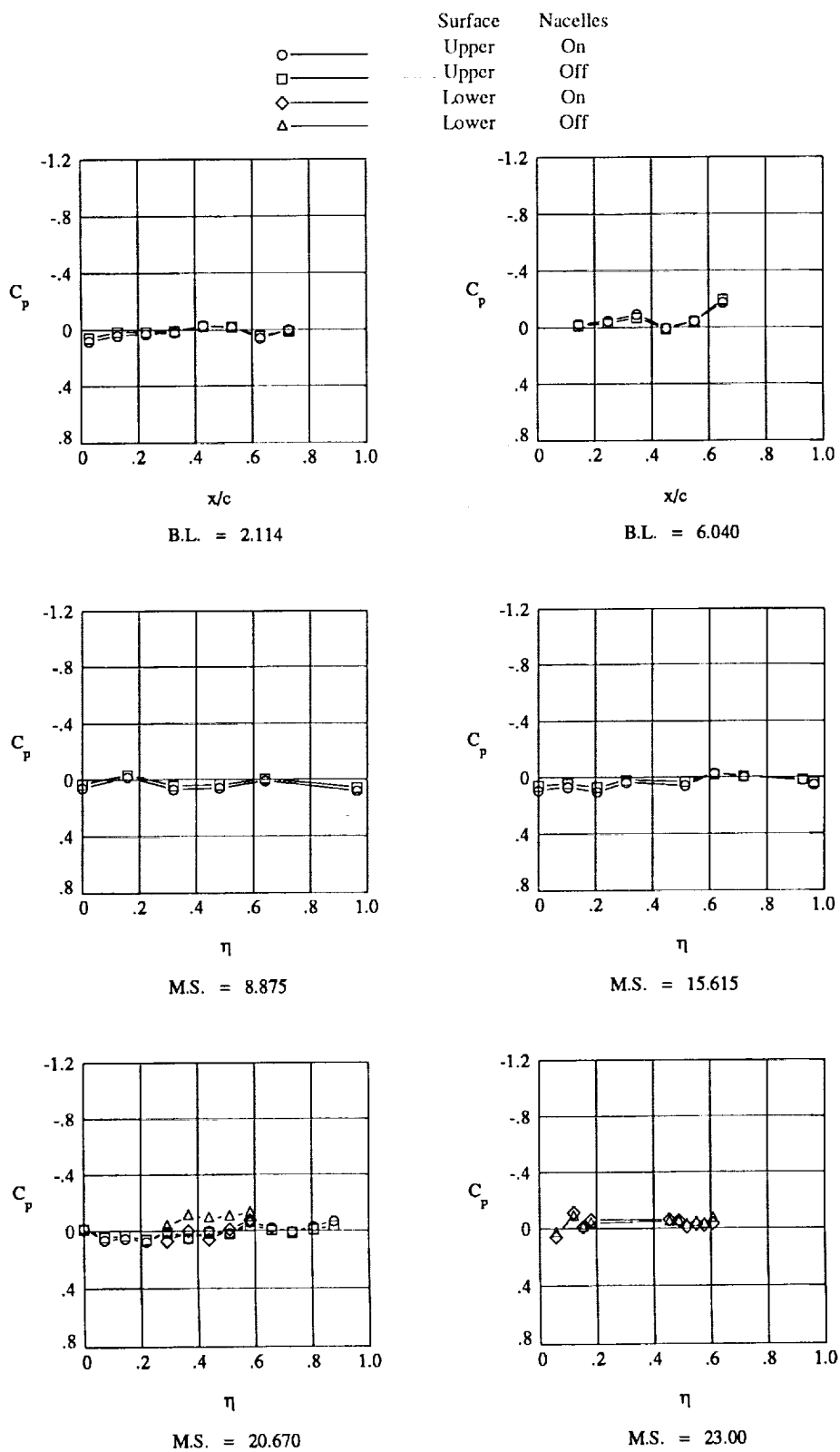
(c) $M_\infty = 0.80$.

Figure 16. Continued.



(d) $M_\infty = 0.90$.

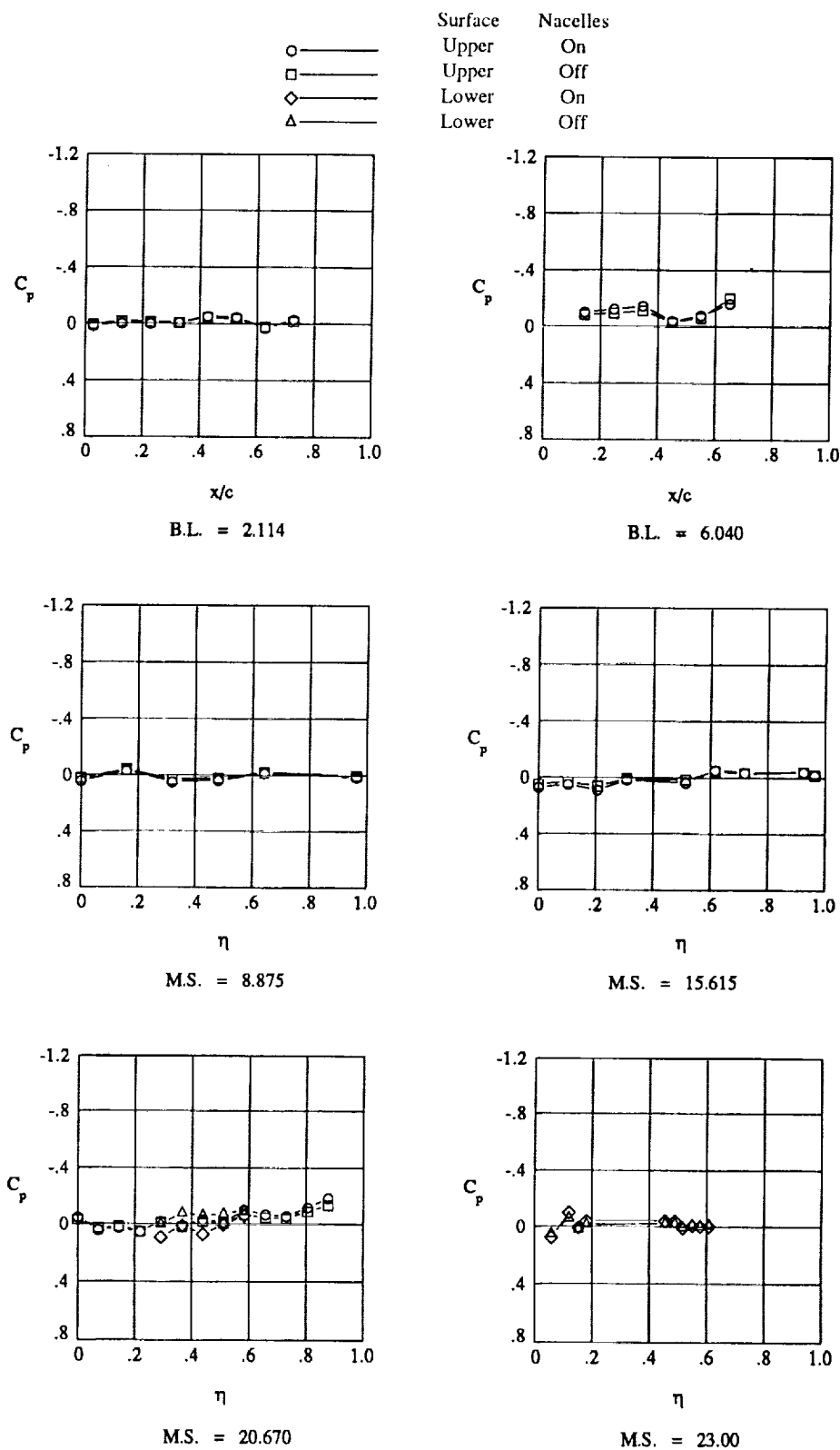
Figure 16. Concluded.



(a) $\alpha = -2.08^\circ$ (nacelles on); $\alpha = -2.41^\circ$ (nacelles off).

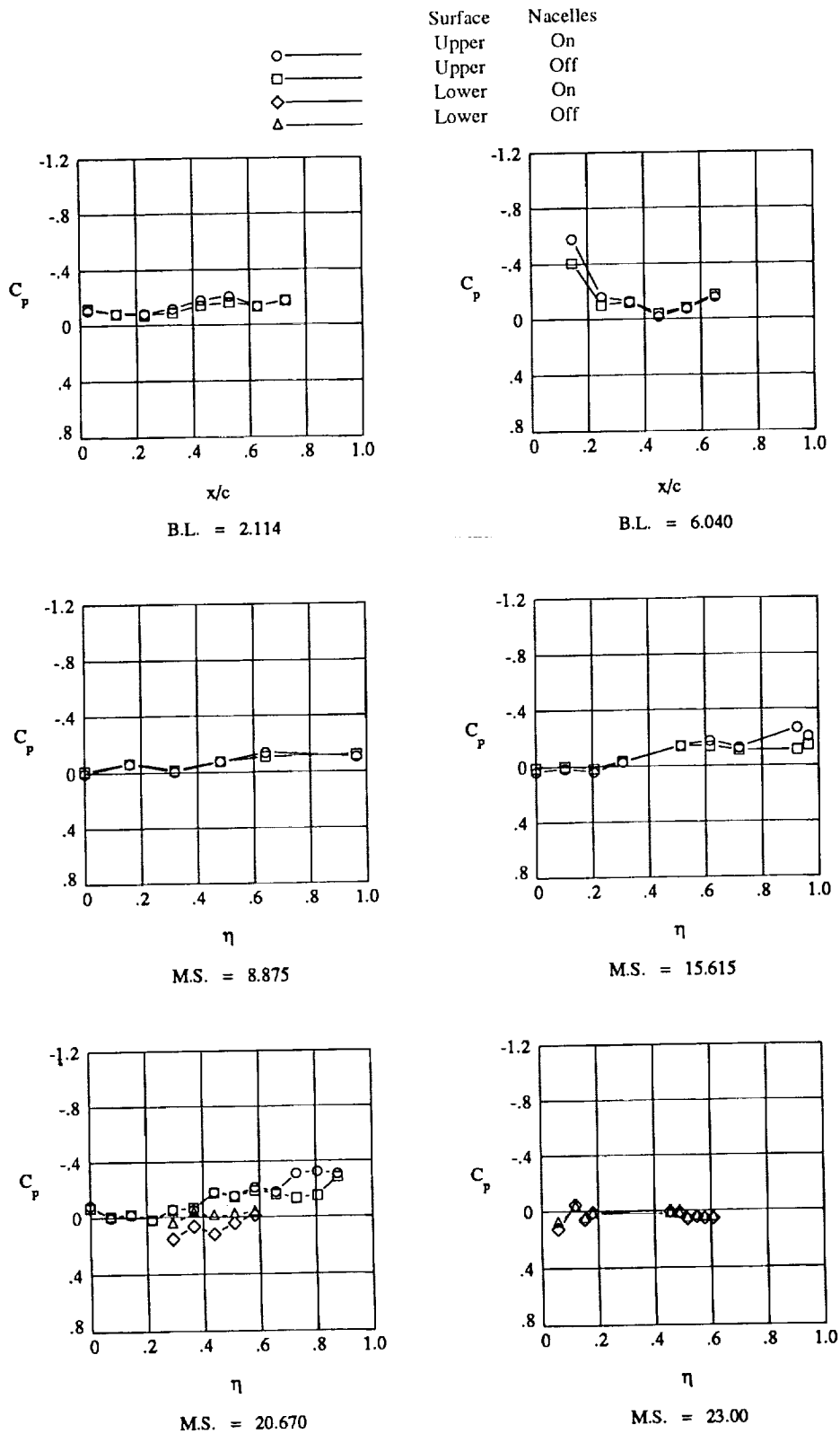
Figure 17. HSCT pressure distributions at $M_\infty = 0.30$. Curved wingtip.

C-2



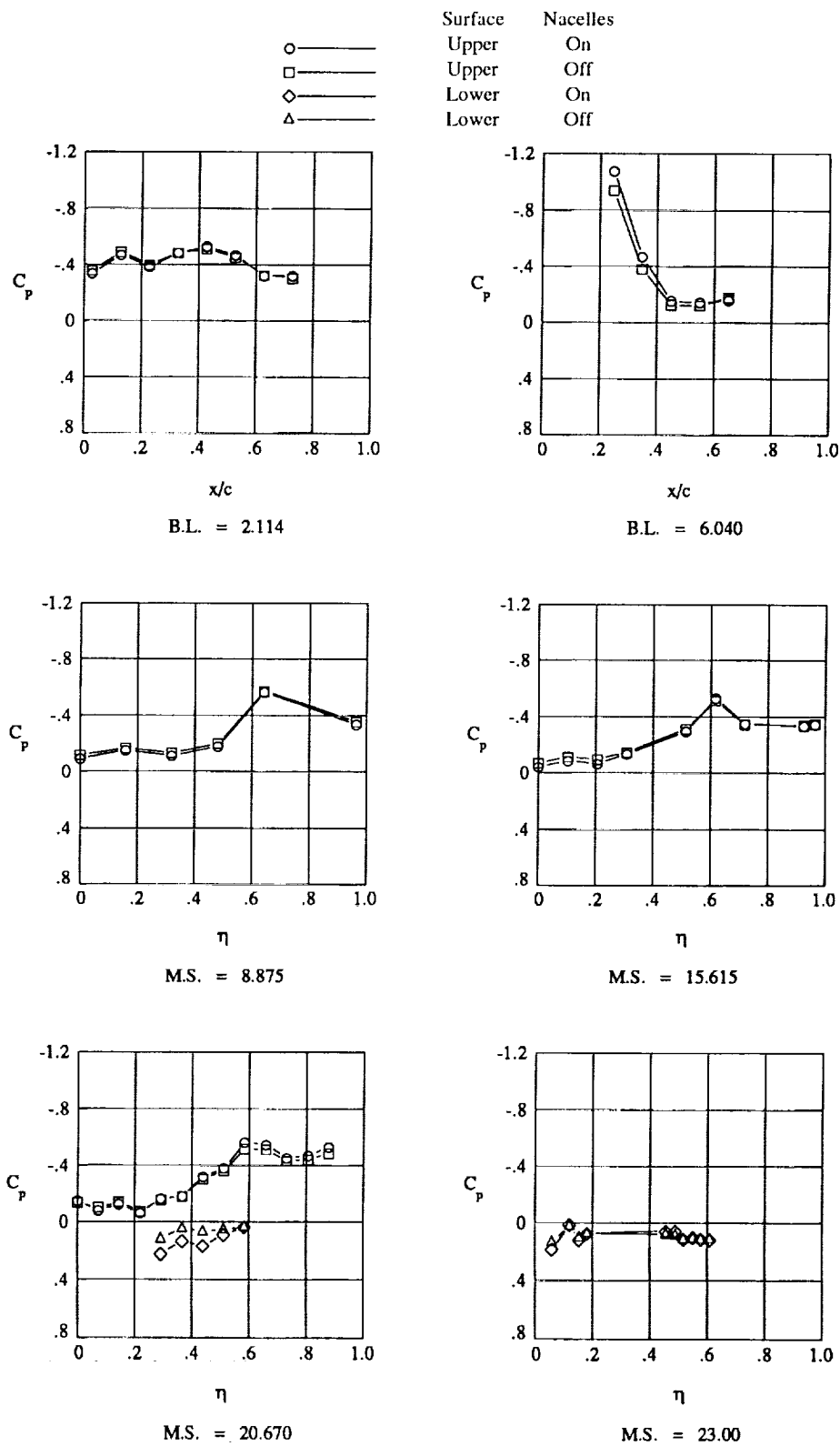
(b) $\alpha = 0.04^\circ$ (nacelles on); $\alpha = -0.23^\circ$ (nacelles off).

Figure 17. Continued.



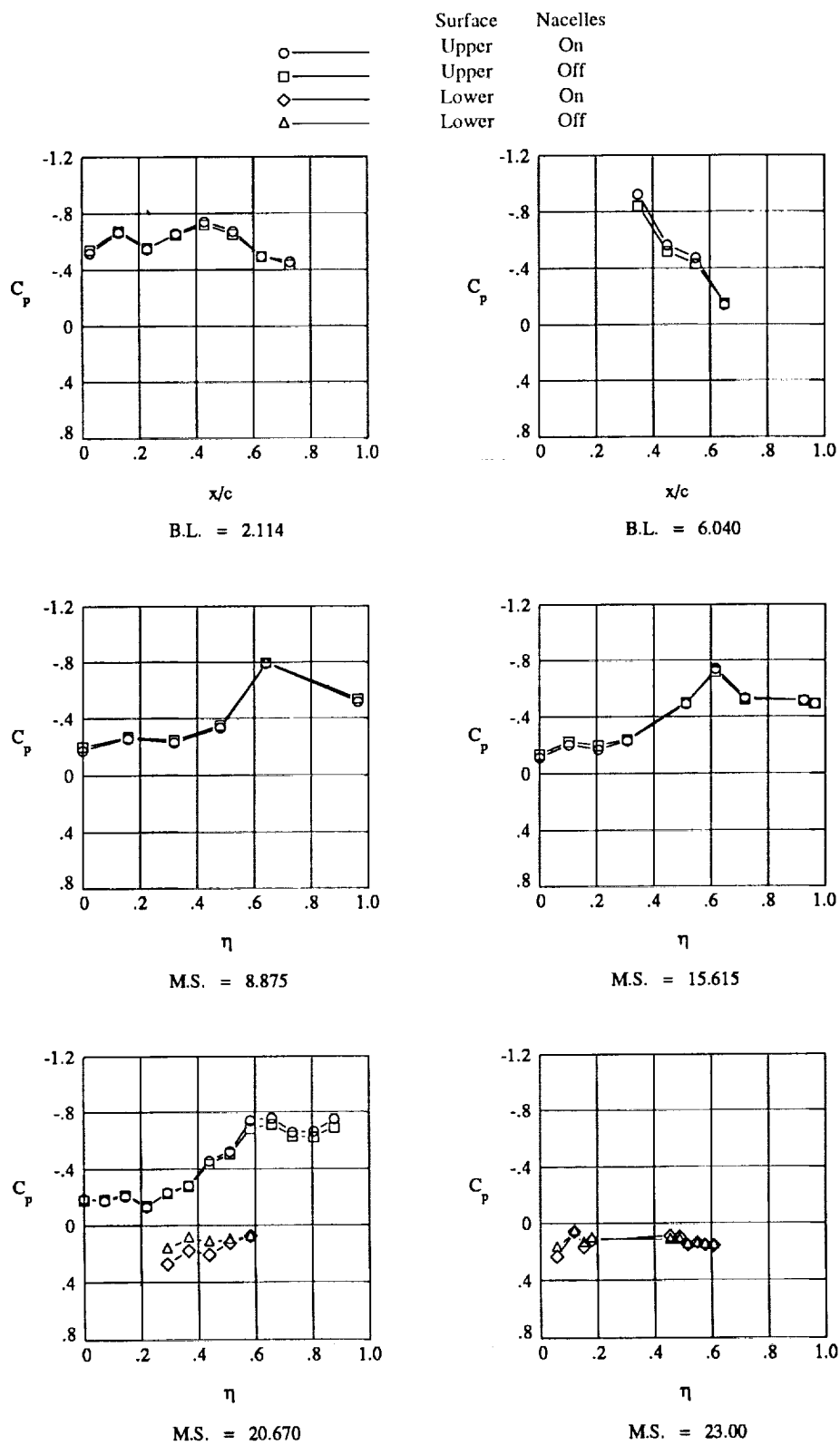
(c) $\alpha = 4.40^\circ$ (nacelles on); $\alpha = 3.92^\circ$ (nacelles off).

Figure 17. Continued.



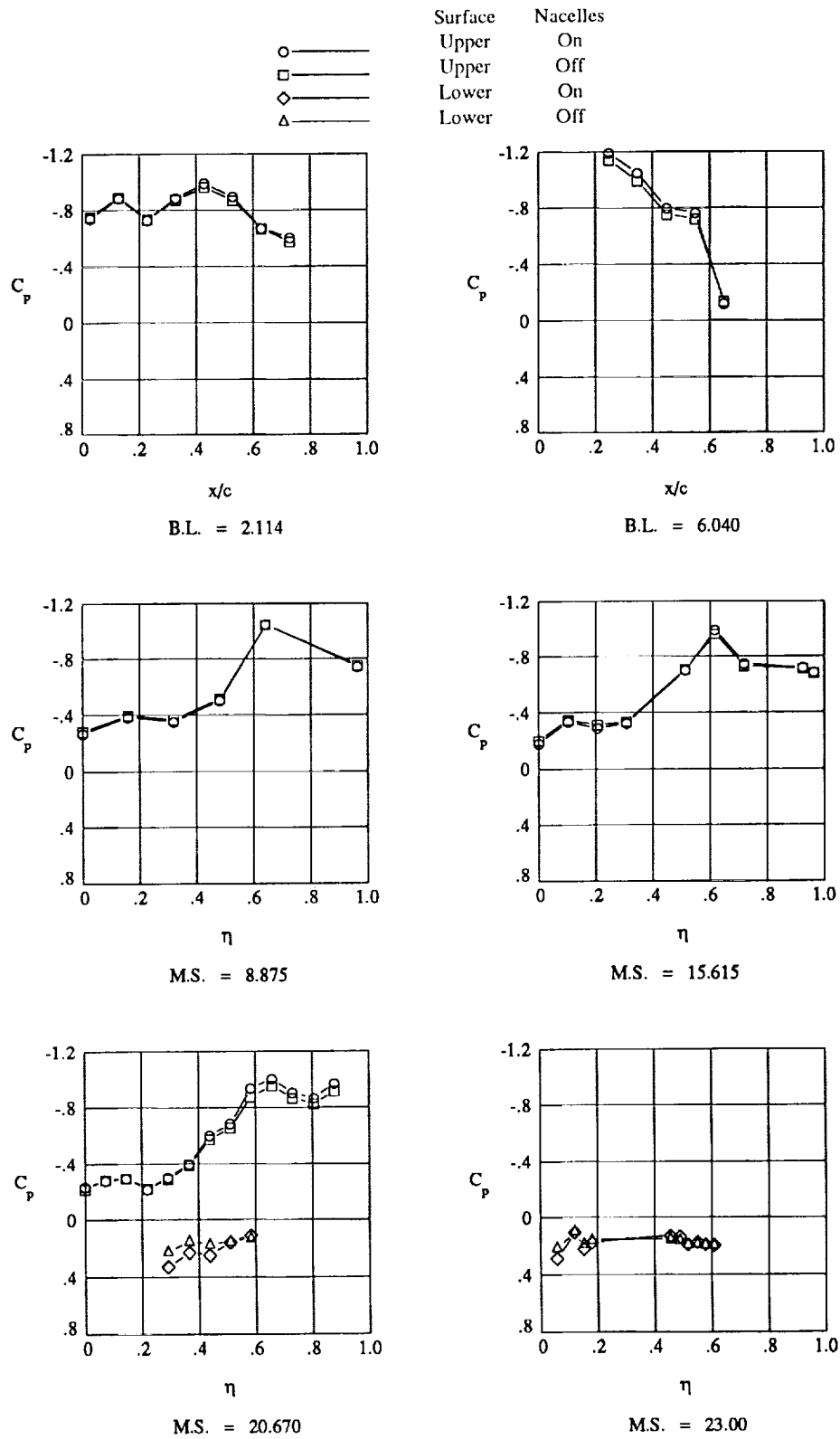
(d) $\alpha = 10.00^\circ$.

Figure 17. Continued.



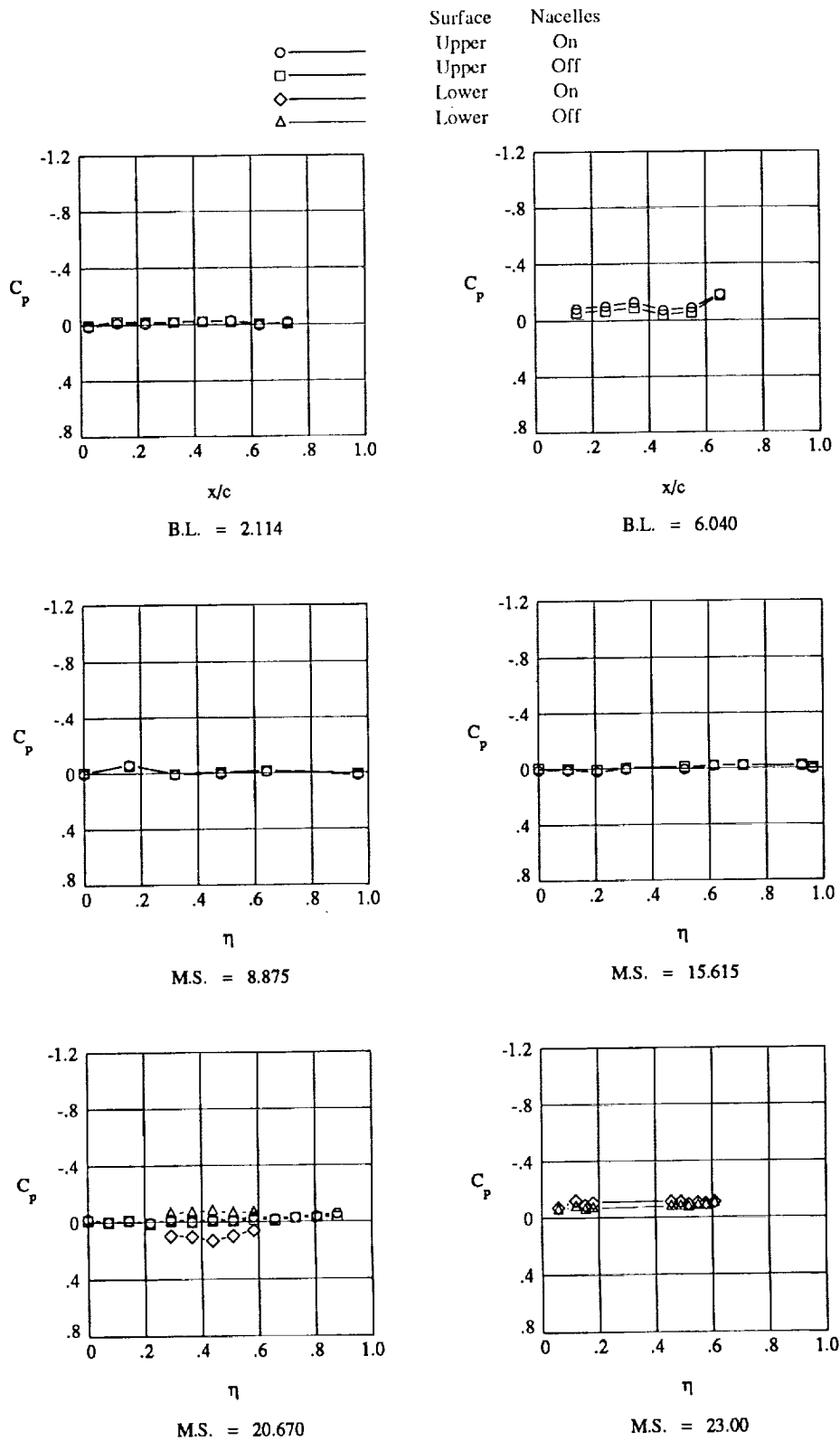
(e) $\alpha = 13.80^\circ$.

Figure 17. Continued.



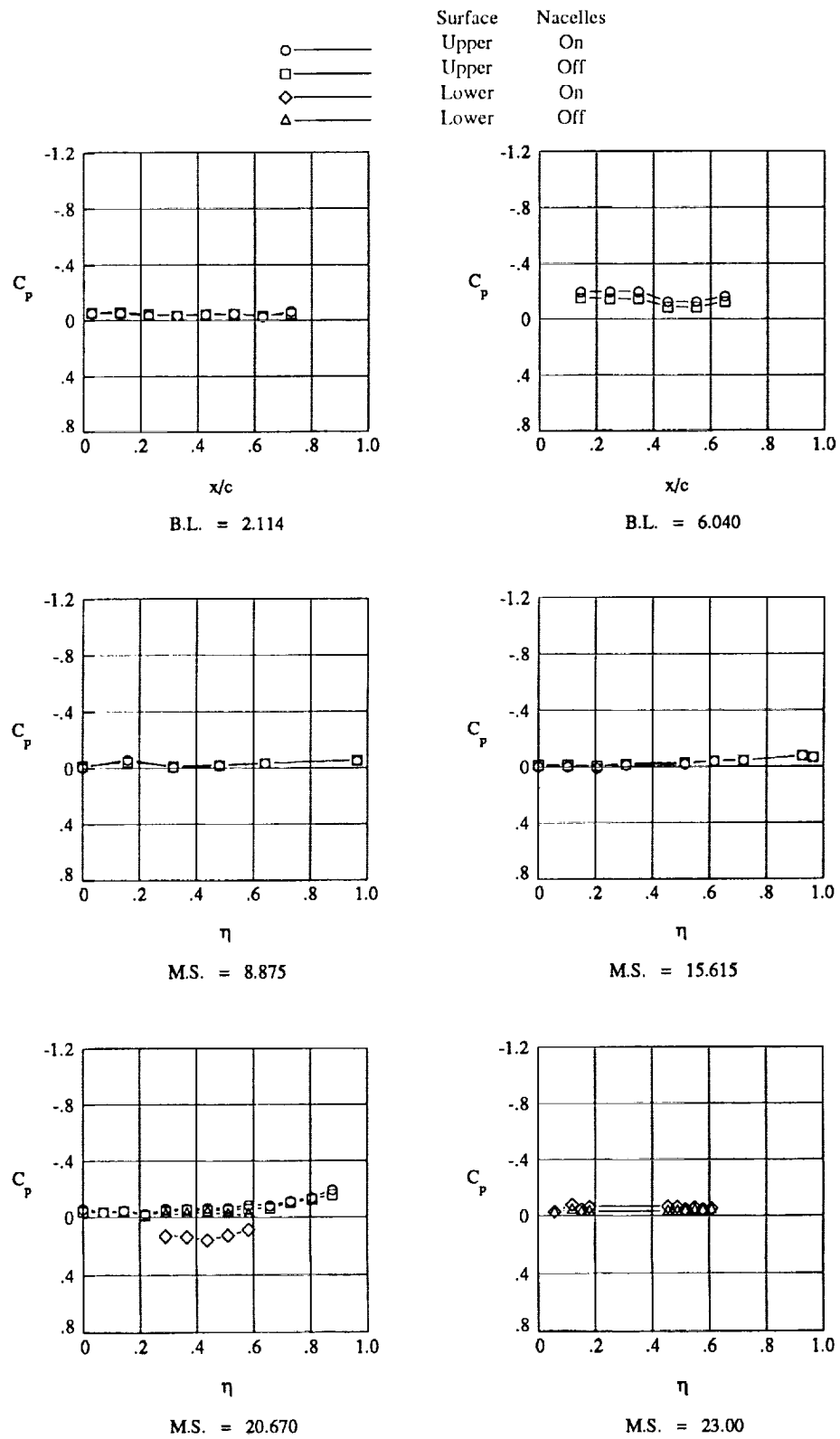
(f) $\alpha = 17.80^\circ$.

Figure 17. Concluded.



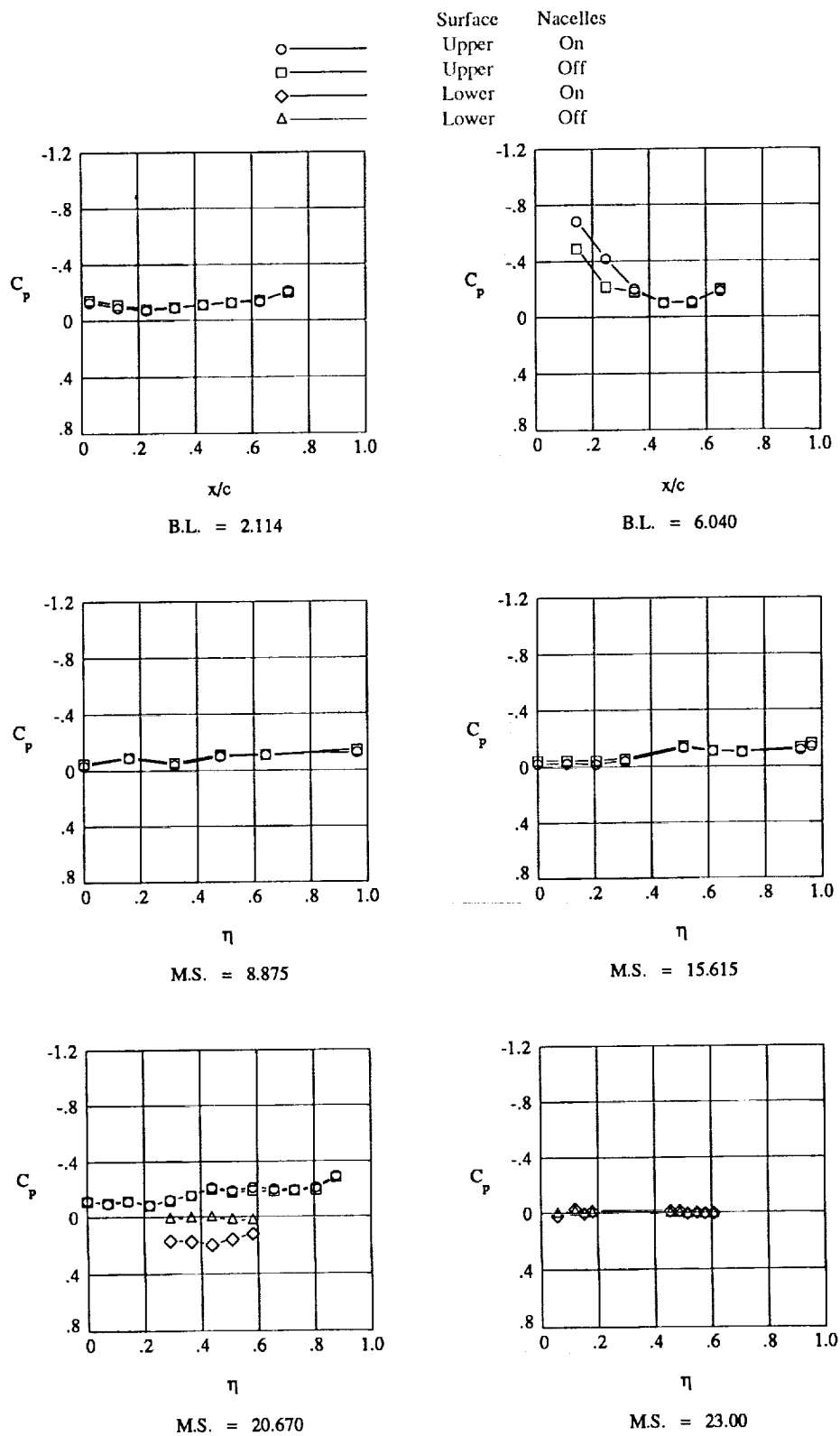
(a) $\alpha = -1.90^\circ$.

Figure 18. HSCT pressure distributions at $M_\infty = 0.90$. Curved wingtip.



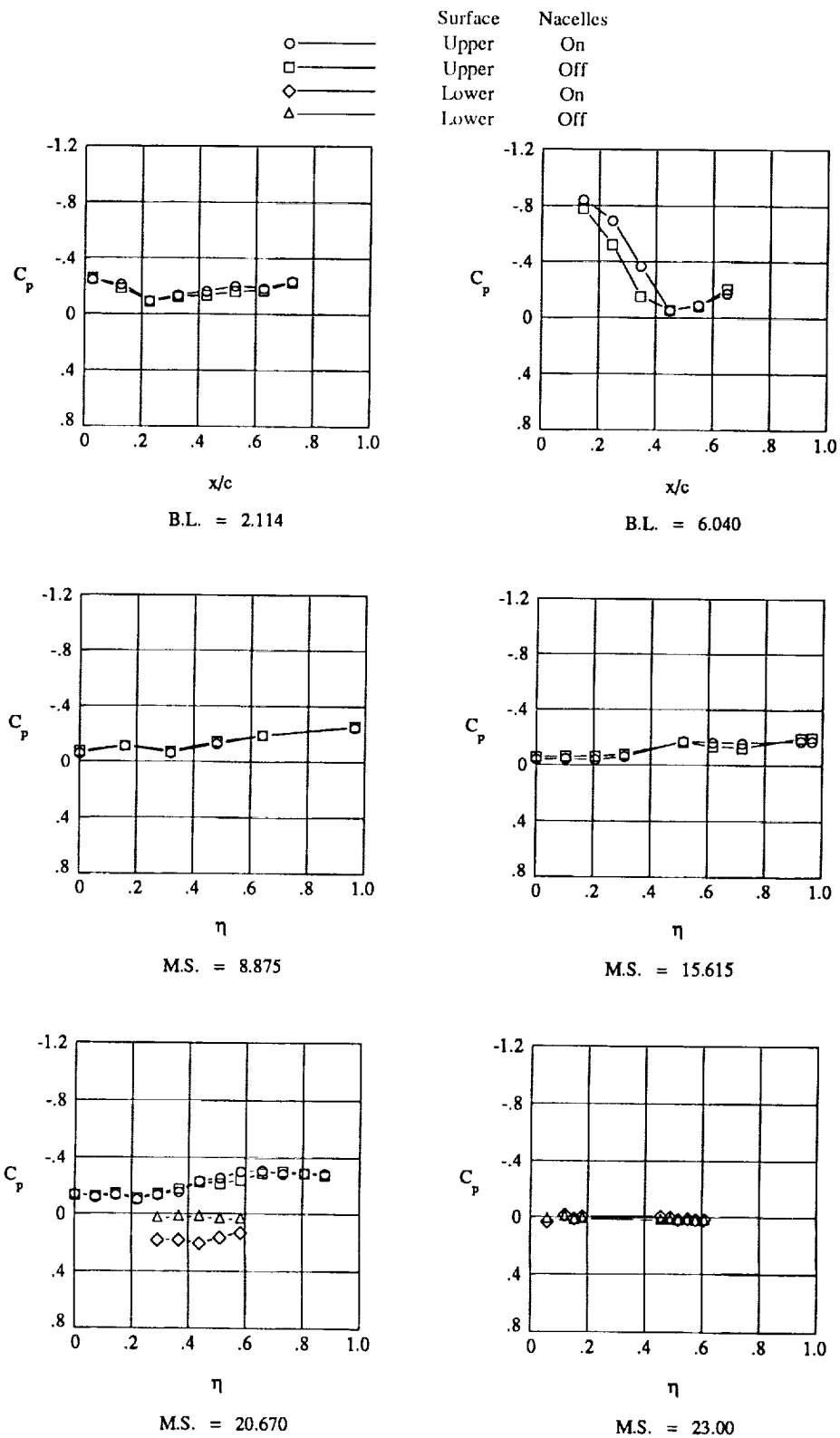
(b) $\alpha = 0.30^\circ$.

Figure 18. Continued.



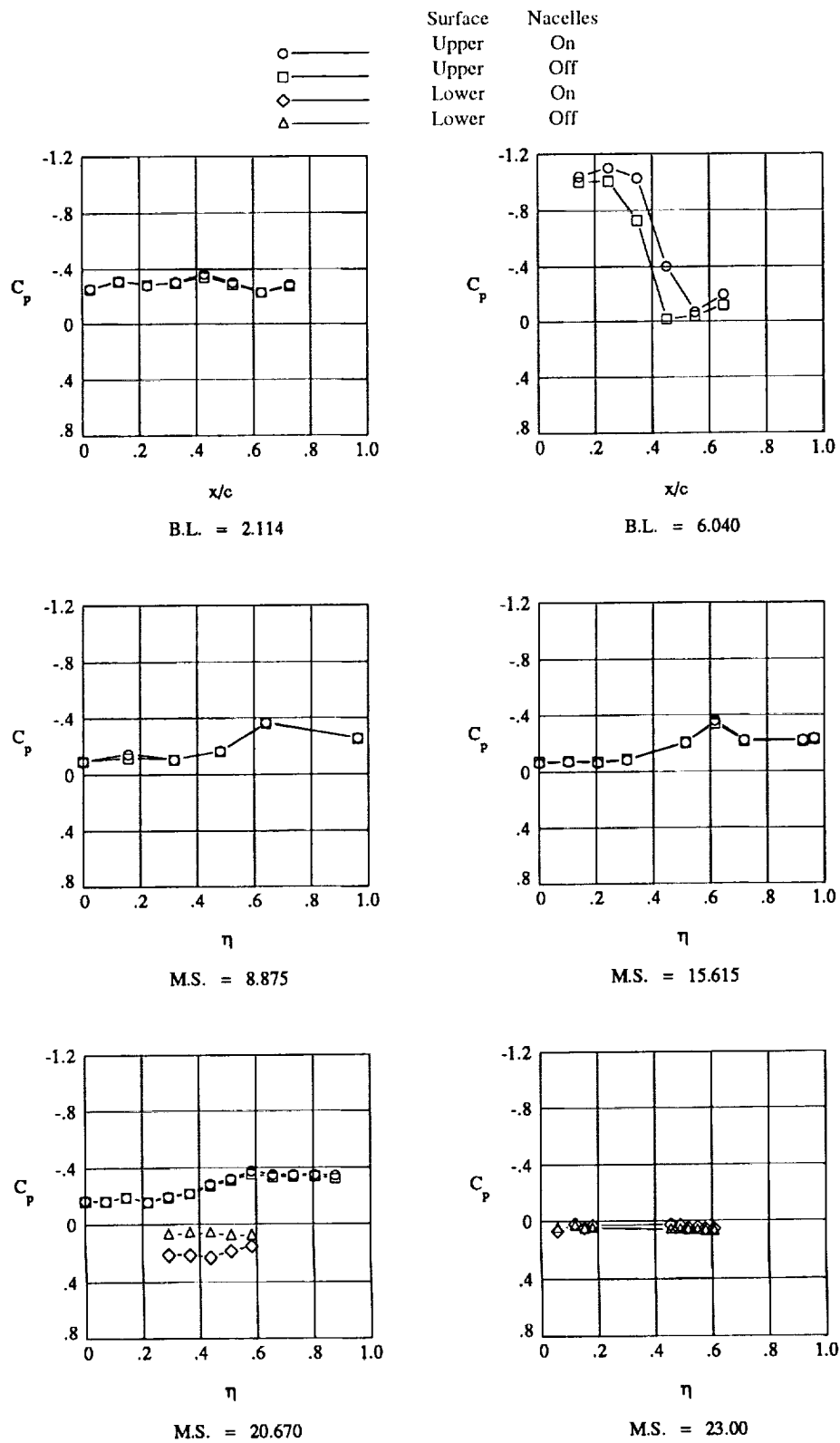
(c) $\alpha = 3.10^\circ$.

Figure 18. Continued.



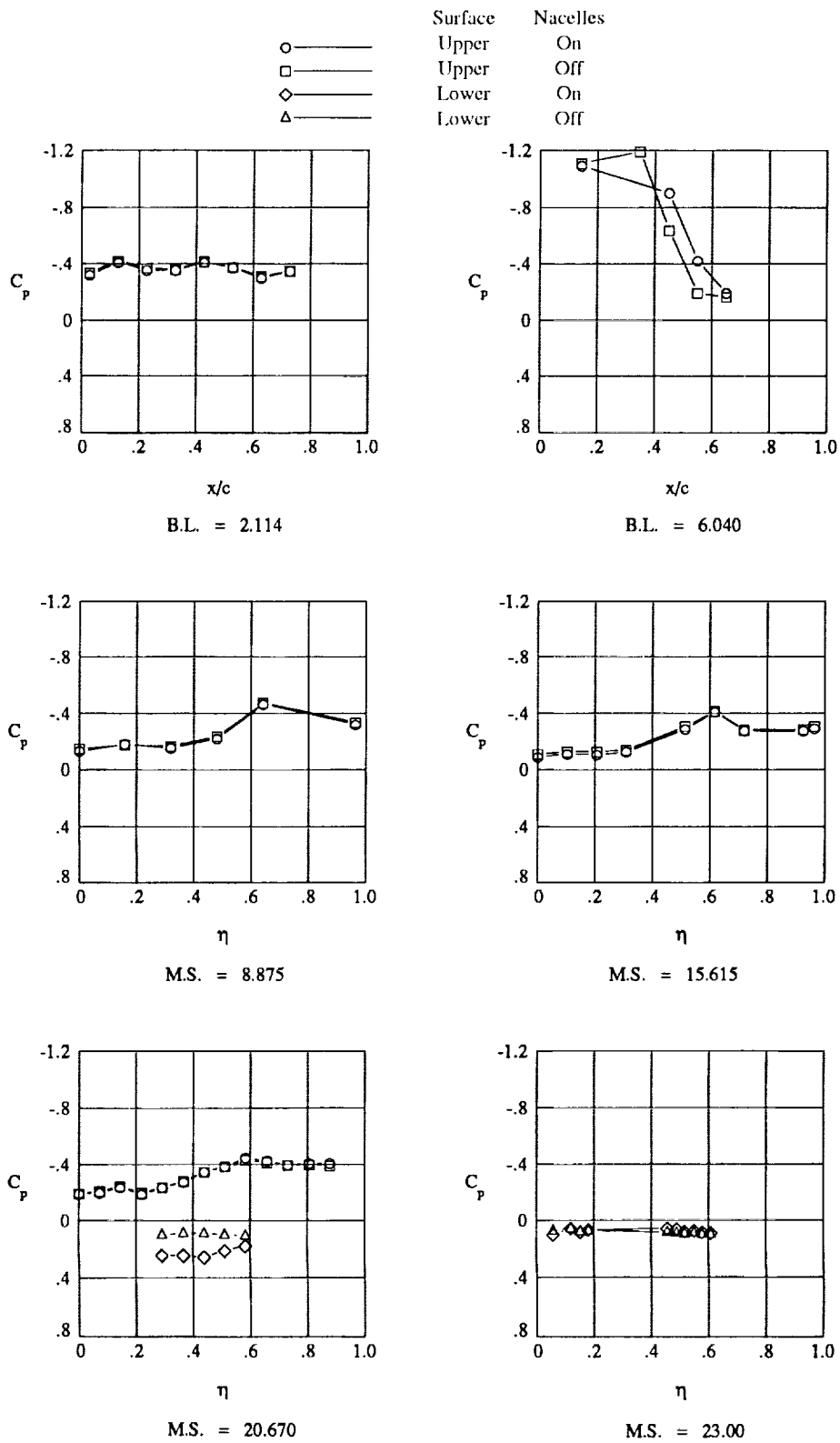
(d) $\alpha = 4.20^\circ$.

Figure 18. Continued.



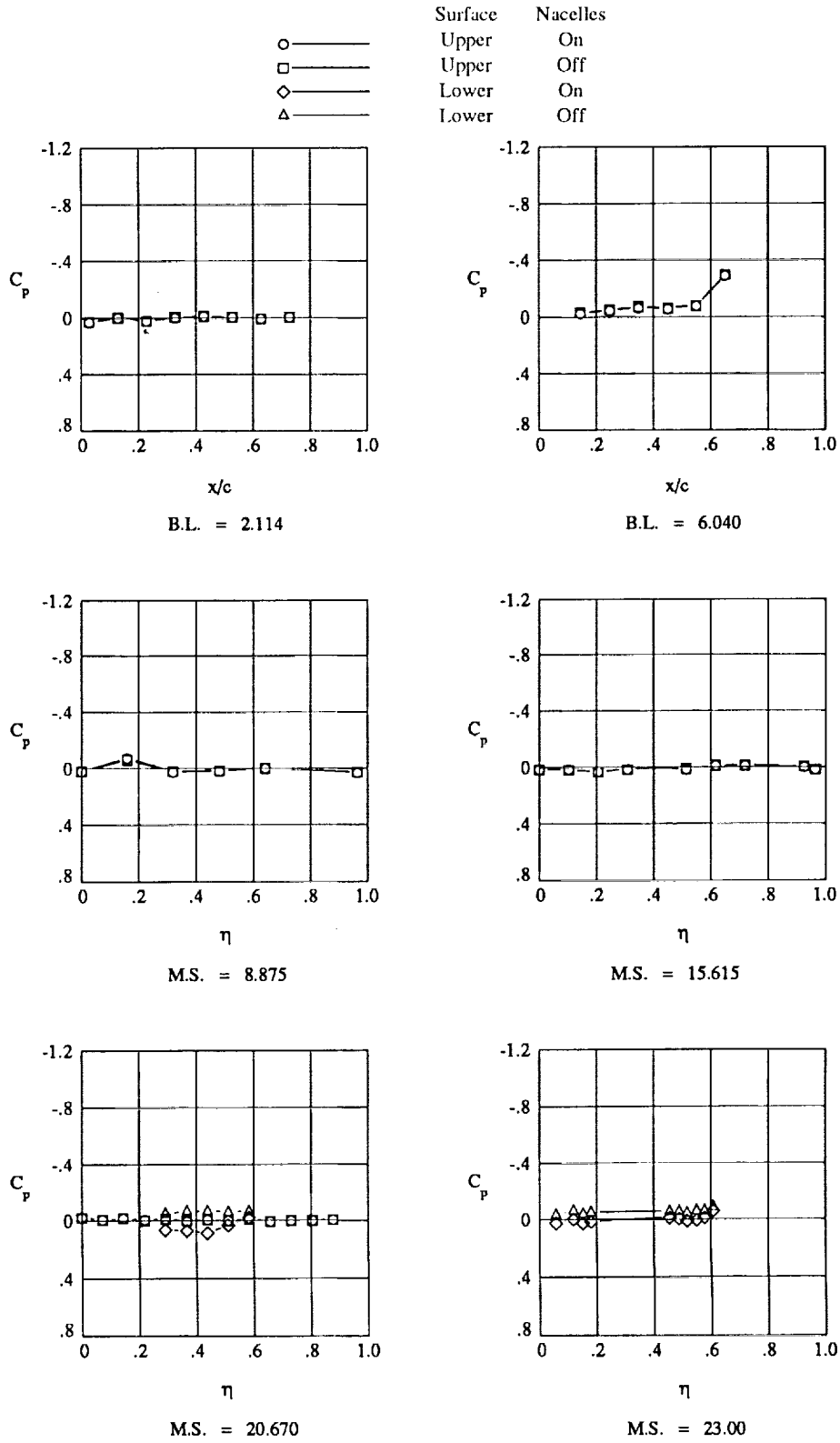
(e) $\alpha = 6.50^\circ$.

Figure 18. Continued.



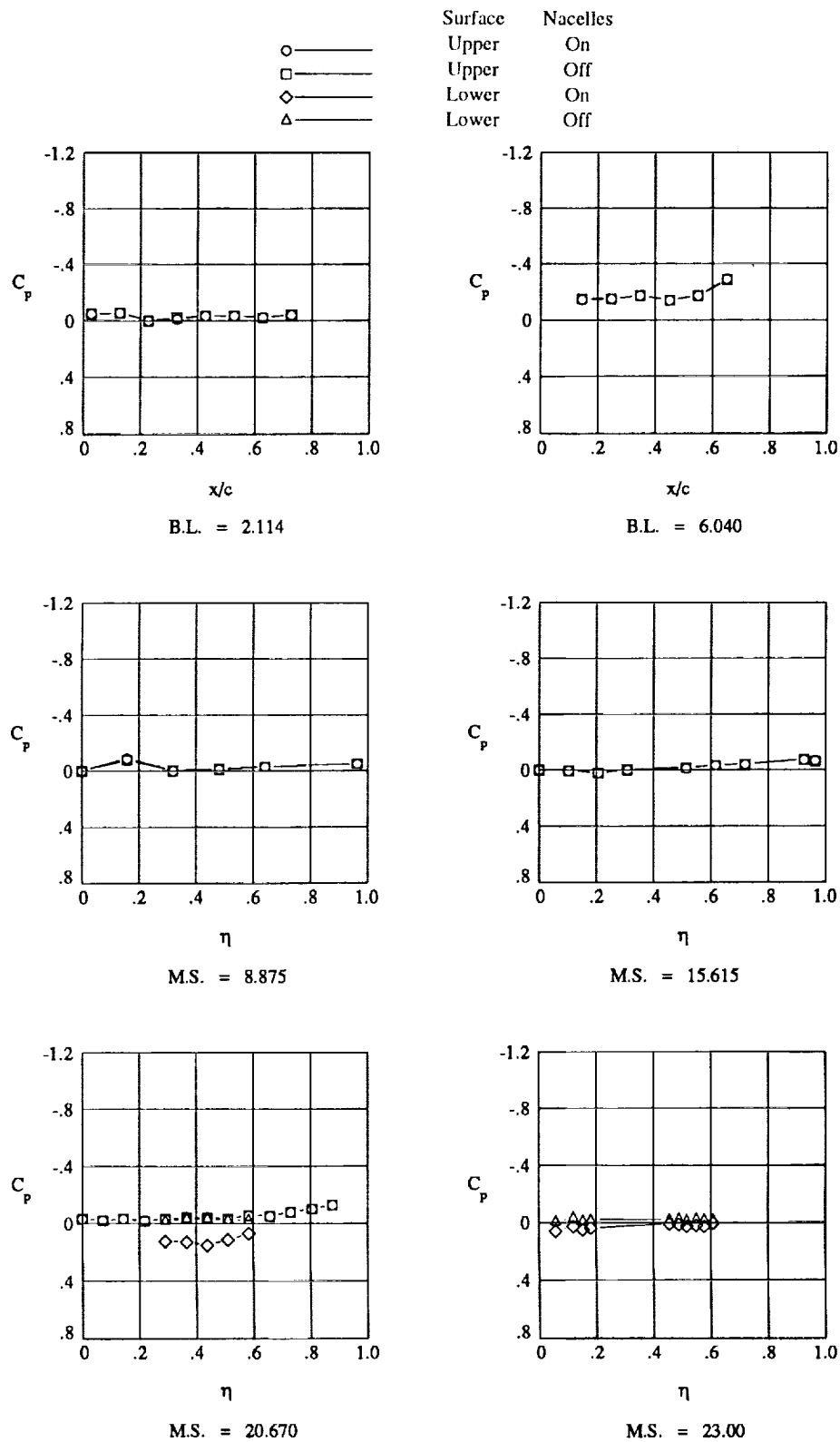
(f) $\alpha = 8.70^\circ$.

Figure 18. Concluded.



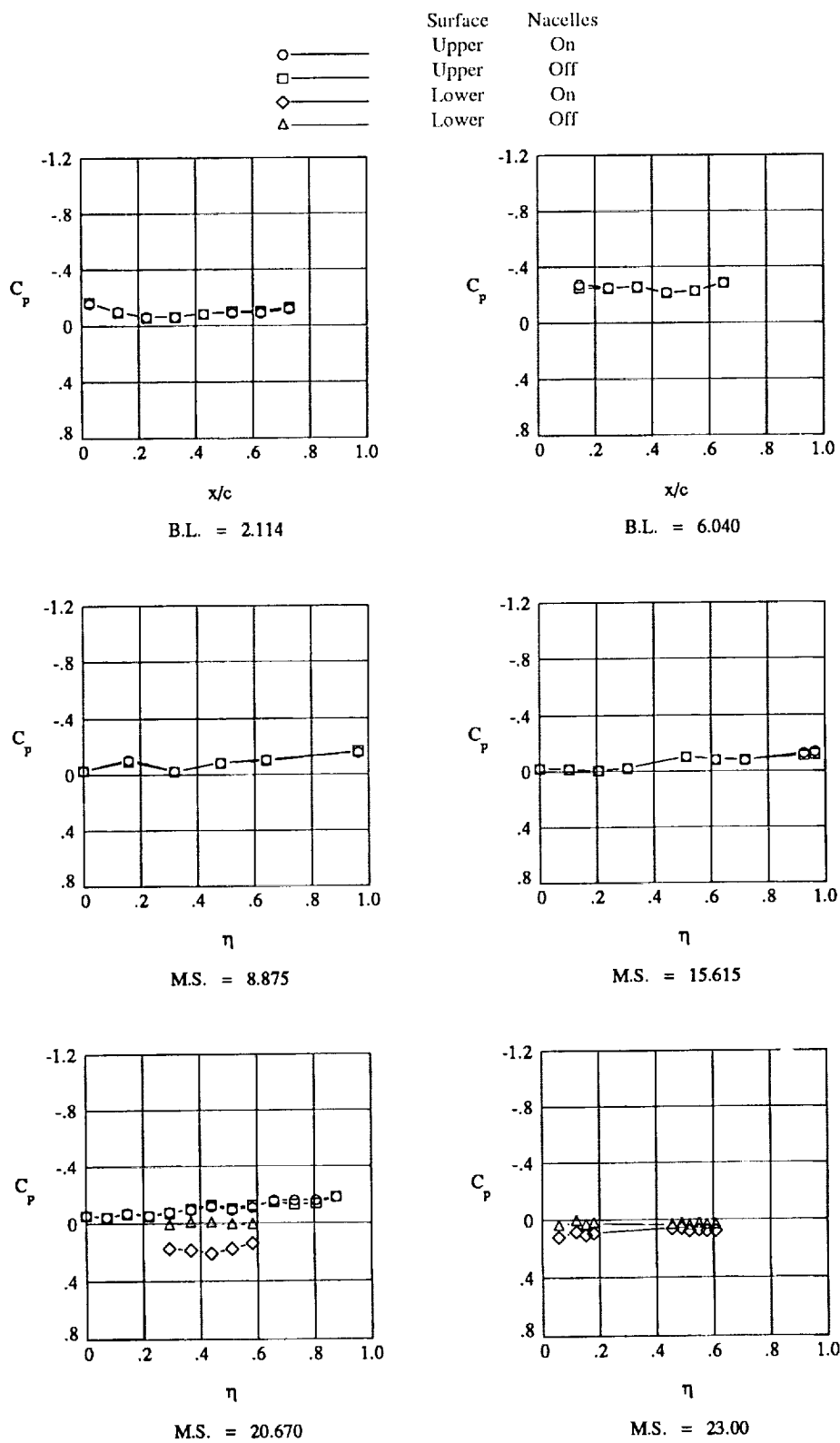
(a) $\alpha = -2.14^\circ$.

Figure 19. HSCT pressure distributions at $M_\infty = 1.19$. Curved wingtip.



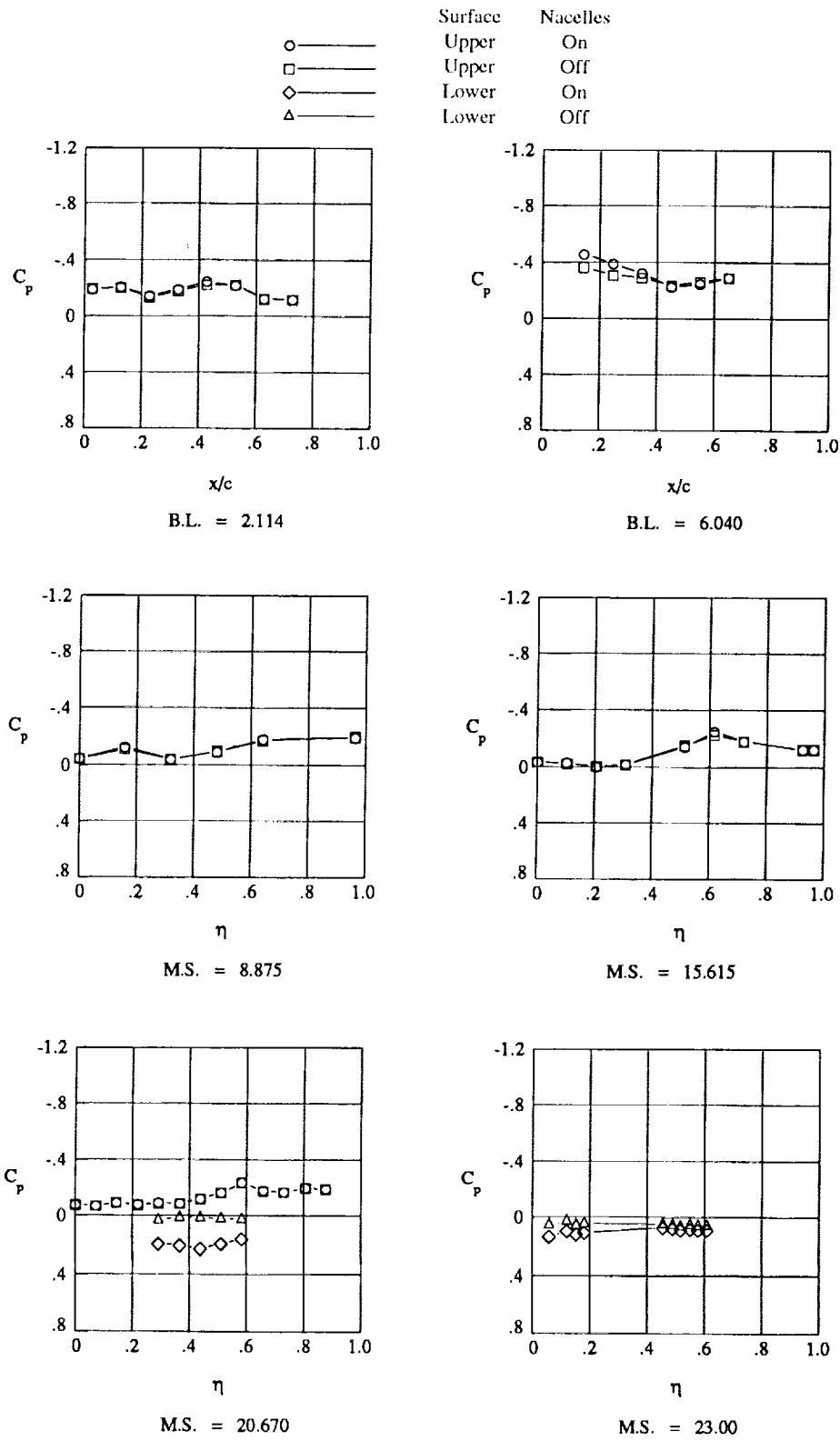
(b) $\alpha = 0.60^\circ$.

Figure 19. Continued.



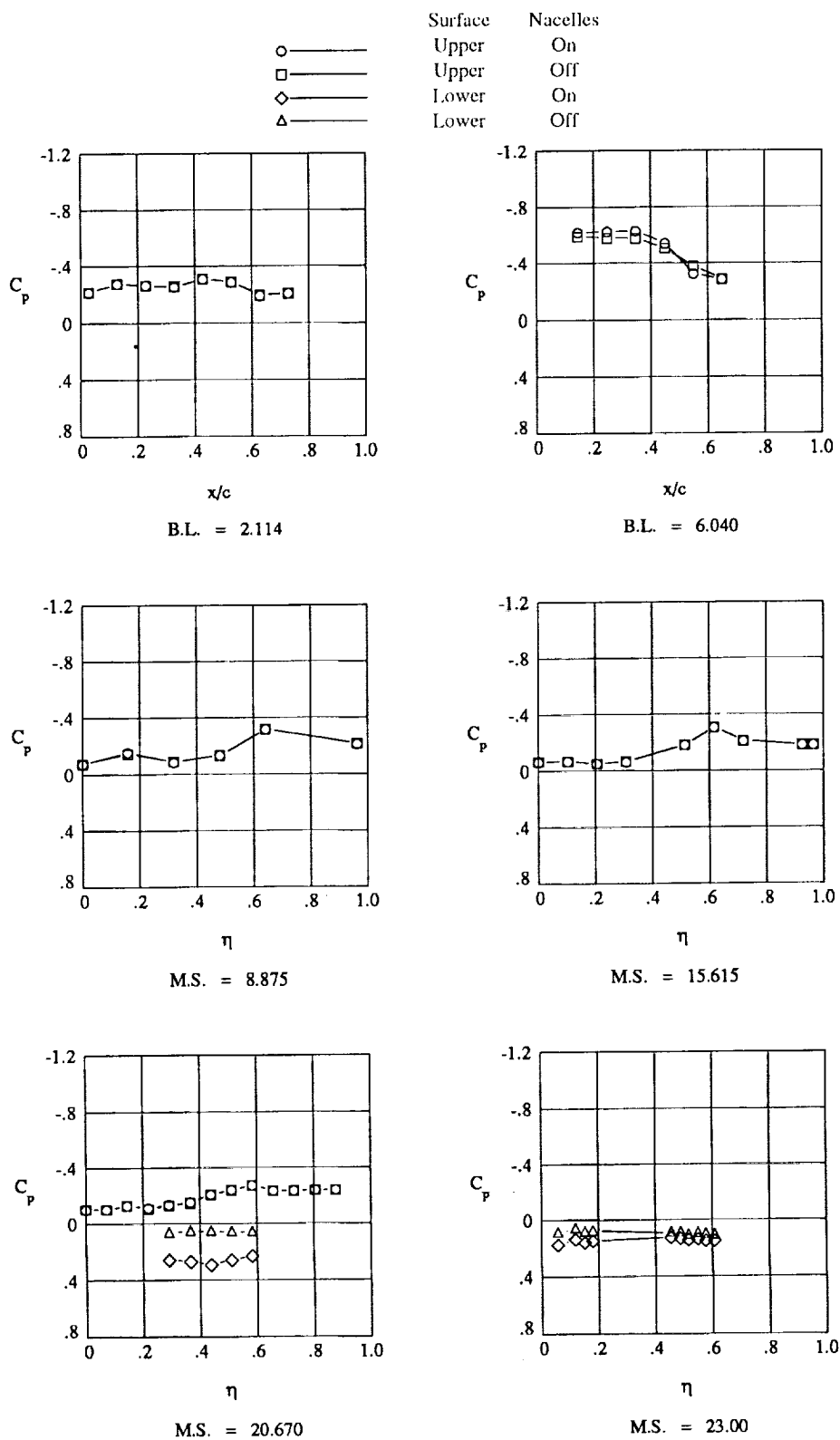
(c) $\alpha = 3.40^\circ$.

Figure 19. Continued.



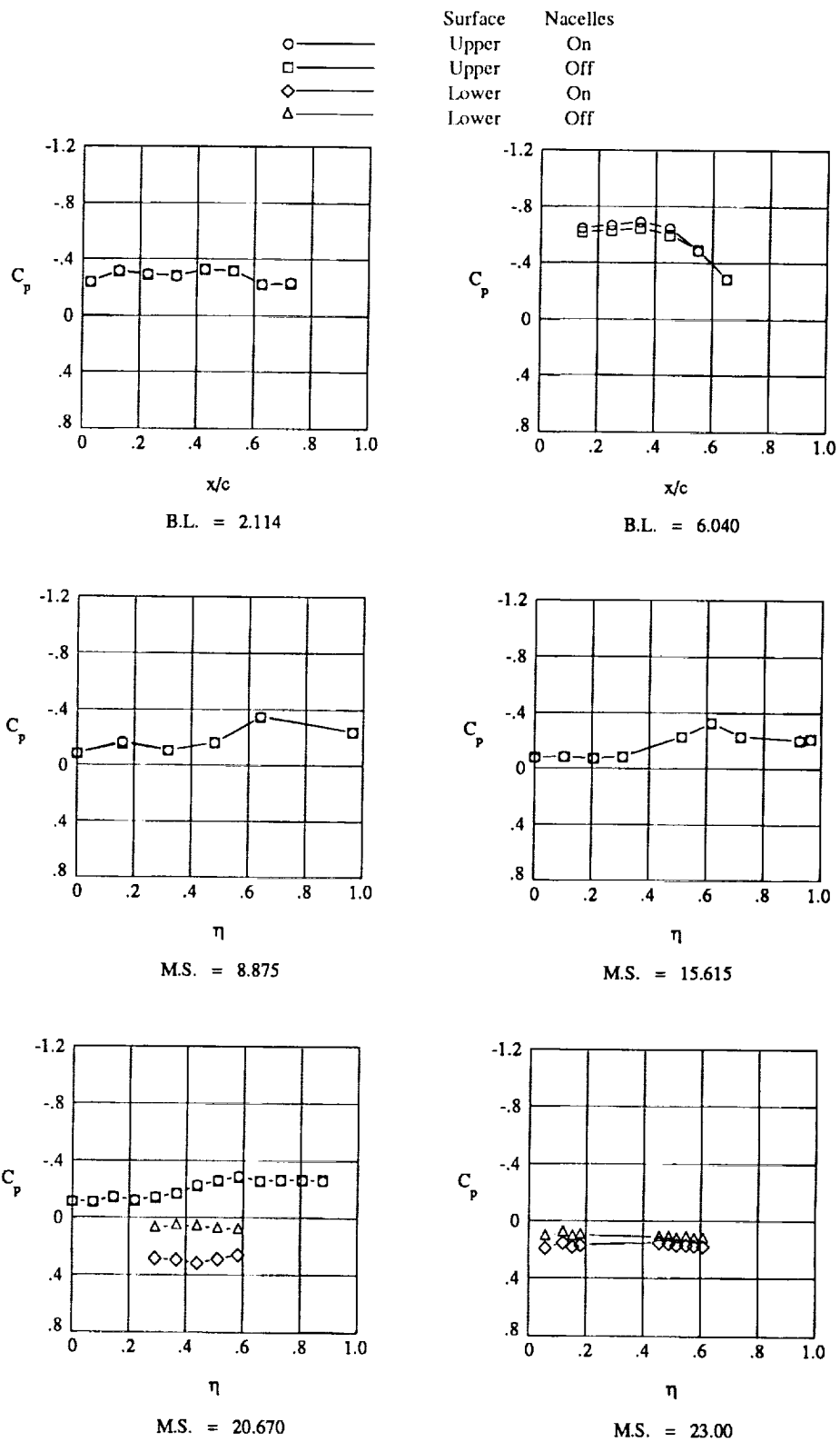
(d) $\alpha = 4.30^\circ$.

Figure 19. Continued.



(c) $\alpha = 6.90^\circ$.

Figure 19. Continued.



(f) $\alpha = 7.60^\circ$.

Figure 19. Concluded.

REPORT DOCUMENTATION PAGE			Form Approved OMB No. 0704-0188	
Public reporting burden for this collection of information is estimated to average 1 hour per response, including the time for reviewing instructions, searching existing data sources, gathering and maintaining the data needed, and completing and reviewing the collection of information. Send comments regarding this burden estimate or any other aspect of this collection of information, including suggestions for reducing this burden, to Washington Headquarters Services, Directorate for Information Operations and Reports, 1215 Jefferson Davis Highway, Suite 1204, Arlington, VA 22202-4302, and to the Office of Management and Budget, Paperwork Reduction Project (0704-0188), Washington, DC 20503.				
1. AGENCY USE ONLY(Leave blank)	2. REPORT DATE September 1992	3. REPORT TYPE AND DATES COVERED Technical Memorandum		
4. TITLE AND SUBTITLE Experimental Study of a Generic High-Speed Civil Transport		5. FUNDING NUMBERS WU 505-59-10-03		
6. AUTHOR(S) Pamela S. Belton and Richard L. Campbell				
7. PERFORMING ORGANIZATION NAME(S) AND ADDRESS(ES) NASA Langley Research Center Hampton, VA 23681-0001		8. PERFORMING ORGANIZATION REPORT NUMBER L-17046		
9. SPONSORING/MONITORING AGENCY NAME(S) AND ADDRESS(ES) National Aeronautics and Space Administration Washington, DC 20546-0001		10. SPONSORING/MONITORING AGENCY REPORT NUMBER NASA TM-4382		
11. SUPPLEMENTARY NOTES				
12a. DISTRIBUTION/AVAILABILITY STATEMENT Unclassified Unlimited Subject Category 02			12b. DISTRIBUTION CODE	
13. ABSTRACT (Maximum 200 words) An experimental study of a generic high-speed civil transport has been conducted in the NASA Langley 8-Foot Transonic Pressure Tunnel. The data base was obtained for the purpose of assessing the accuracy of various levels of computational analysis. Two models differing only in wingtip geometry were tested with and without flow-through nacelles. The baseline model has a curved or crescent wingtip shape, while the second model has a more conventional straight wingtip shape. The study was conducted at Mach numbers from 0.30 to 1.19. Force data were obtained on both the straight wingtip model and the curved wingtip model. Only the curved wingtip model was instrumented for measuring pressures. Selected longitudinal, lateral, and directional data are presented for both models. Selected pressure distributions for the curved wingtip model are also presented.				
14. SUBJECT TERMS High-speed civil transport; Transonic wind tunnel test			15. NUMBER OF PAGES 113	
			16. PRICE CODE A06	
17. SECURITY CLASSIFICATION OF REPORT Unclassified	18. SECURITY CLASSIFICATION OF THIS PAGE Unclassified	19. SECURITY CLASSIFICATION OF ABSTRACT	20. LIMITATION OF ABSTRACT	

NSN 7540-01-280-5500

Standard Form 298 (Rev. 2-89)
Prescribed by ANSI Std. Z39-18
298-102

NASA-Langley, 1992